Impairment Analysis and Mitigation for Cost-Effective OFDM-based Access Systems

vorgelegt von
M.Sc.
Nuno Miguel Duarte Sequeira André
ORCID: 0000-0003-2667-687X

von der Fakultät IV - Elektrotechnik und Informatik
der Technischen Universität Berlin
zur Erlangung des akademischen Grades

Dr. der Ingenieurwissenschaften
- Dr.-Ing. -

genehmigte Dissertation

Promotionsausschuss:
Vorsitzender: Prof. Dr.-Ing. Wolfgang Heinrich
Gutachter: Prof. Dr.-Ing. Klaus Petermann
Gutachter: Prof. Dr.-Ing. Norbert Hanik (TU München)
Gutachter: PD Dr. Volker Jungnickel (Fraunhofer HHI)

Tag der wissenschaftlichen Aussprache: 28/06/2019

Berlin 2020

Dedicated to my godmother, Albina
and my parents, Ana and Alcindo

Acknowledgements

First and foremost I would like to express my most sincere appreciation to Professor Klaus Petermann for all the support during the supervision of my thesis. His vast knowledge of all optical communication topics was a decisive factor in directing my research to loftier goals and thus improving the quality of my work.

This acknowledgement would not be complete without a mention of the deepest gratitude towards Hadrien Louchet for his *in loco* supervision at *VPIphotonics*. His continued support, encouragement, knowledge, attention to detail and friendship were the *condiciones sine quibus non* for the making of this dissertation.

I would also like to show my deep gratitude to André Richter for all the support and encouragement given during my stay at *VPIphotonics*. Sincere appreciation to Igor Koltchanov for our lengthy discussions on the realm of quantum mechanics that enabled me to gain a deeper understanding on this field and on how it influences our macro world. A special thank you also to Dimitar Kroushkov for his insightful remarks and unwavering encouragement, always pushing me forth to do more and better.

Deep gratitude goes to Kai Habel of the *Fraunhofer Heinrich-Hertz-Institut* for his untiring support in my experimental work. I would also like to thank the Laser Group of the *Fraunhofer Heinrich-Hertz-Institut* for providing their laser device to be used in my research enabling me to obtain important results.

To Volker Filsinger and Erik Hansen of *SHF Communication Technologies*, a big thank you for supporting my research at *SHF* where we explored the limits of OFDM transmission at low resolutions.

Big thank you to Amin Abbasi and Abdul Rahim of the *Photonics Research Group at Ghent University* for inviting me to participate in their ground breaking research in indium phosphide transmitters.

A word of appreciation to Professor António Teixeira of Aveiro University for his support and encouragement.

A special thanks to all my colleagues at *VPIphotonics* for the support and great work atmosphere.

To Carminda and Dinis Silva a sincere thank you for helping me with my first steps in Germany.

A big thanks to my friend Ricardo Gama for his insights and support.

Lastly, a big thank you to my long time friend Flavio Pohlmann for sharing with me the exciting world of ham radio, which was a deciding factor in the choice of telecommunications as the subject of my studies.

This work was supported by the *Bundesministerium für Bildung und Forschung* under Grant 16 BP 1136 through the framework of the *European Union's PIANO+* project *OCEAN*.

Abstract

The growth in broadband connection speed has been exponential, and this trend will continue in the foreseeable future [1]. An access network is a connection between users and service providers and therefore a key element in support of this growth. While expanding its broadband offer a service provider must ensure seamless migration through compatibility with legacy networks, and also create an offer that is attractive to customers. Access networks are designed to support numerous users at different distances from the service provider. Cost-efficiency is mandatory. It usually relies upon using **P**assive **O**ptical **N**etworks (PONs) and low complexity electro-optical devices (direct modulation/detection), whose performance can be unlocked by digital signal processing to mitigate components' limitations. Novel optical modulation formats help to achieve large spectral efficiencies and allow advanced signal distribution. One such modulation format is **O**rthogonal **F**requency **D**ivision **M**ultiplexing (OFDM), which offers a compact spectrum, resilience to chromatic dispersion and flexible subcarrier allocation [2].

Legacy PON systems use C-band (1500nm) downlinks and O-band (1330nm) uplinks [3]–[9]. The C-band has low attenuation at the cost of higher chromatic dispersion [10]. The O-band has practically no chromatic dispersion but higher attenuation [10] enabling the use of simpler transmitters, **D**irectly **M**odulated **L**asers (DMLs) for example. The latest PON systems must enable parallel operation with legacy systems. For this reason they operate both in the C-band down- and uplink [11]. A DML has chirp as a by-product of transmission [12], [13]. Chirp interacts with fibre chromatic dispersion (C-band) to create **S**ubcarrier-to-**S**ubcarrier **I**ntermixing **I**nterference (SSII) at the receiver after direct detection [14]. This occurs despite OFDM's resilience to chromatic dispersion and is one of the main impairments of cost-effective OFDM-based access systems. The main contribution of this work is to predict and analyse the impact of SSII as an impairment and to propose and experimentally verify mitigation techniques.

An analytical formulation capable of **S**ignal-to-**N**oise **R**atio (SNR) prediction for OFDM-based DML transmission is derived. This formulation is capable of determining the contribution of each subcarrier to SNR degradation. The DML intensity and frequency responses are included in the formulation by a, also presented, simplified laser model. The predictions of this formulation are experimentally validated under various conditions [15].

A bit-and-power loading algorithm is also proposed. It adapts the power and capacity of each subcarrier to the channel in order to maximize total transmission capacity [16].

Finally, an adaptive equalizer is presented. An optimization procedure is proposed to enable efficient mitigation of SSII [17]. Experimental results show a capacity increase of $\simeq$33% when using the proposed optimized equalizer [18].

Zusammenfassung

Der Bedarf an hochbitratigen Telekommunikationsverbindungen zeigt seit jeher ein exponentielles Wachstum, welches auch in näher Zukunft anhält [1]. Die Zugangsnetze bilden die Verbindungen zwischen Endnutzern und Telekommunikationsanbietern und leisten damit einen wesentlichen Beitrag zur Realisierung des Wachstums. Um das Breitbandangebot zu erweitern, müssen Telekommunikationsanbieter die rückwärtskompatible Aufrüstung existierender Netzwerke gewährleisten und dabei ebenso ein attraktives Kundenangebot schaffen. Zugangsnetze werden entworfen, um eine Vielzahl an Kunden in unterschiedlichen Entfernungen vom Telekommunikationsanbieter anzuschließen. Kosteneffizienz ist dabei zwingend nötig, weshalb häufig auf Passive Optische Netzwerke (PONs) und elektro-optische Komponenten (Detektoren, Modulatoren) von geringer Komplexität zurückgegriffen wird. Dessen Leistungsfähigkeit kann mit digitaler Signalverarbeitung verbessert werden. Neuartige optische Modulationsformate können ebenso eingesetzt werden, um eine gute spektrale Effizienz mit Hilfe komplexer Signalverteilung zu realisieren. Ein derartiges Modulationsformat ist Orthogonales Frequenzmultiplexverfahren (OFDM). Es bietet ein kompaktes Spektrum, Robustheit gegenüber chromatischer Dispersion und eine flexible Zuweisung der Signalträger im Spektrum [2].

Herkömmliche PONs nutzen das C-Band (1500nm) zum Downlink von Daten und das O-Band (1330nm) zum Uplink von Daten [3]–[9]. Das C-Band zeichnet sich durch eine geringe Dämpfung bei jedoch hoher chromatischer Dispersion aus [10]. Das O-Band hat fast keine chromatische Dispersion, jedoch eine höhere Dämpfung als das C-Band [10]. Dies ermöglicht den Einsatz einfacher Sender im O-Band wie zum Beispiel direkt-modulierte Laser (DML). Moderne PONs müssen einen parallelen Betrieb mit herkömmlichen Netzen erlauben. Aus diesem Grund werden im C-Band sowohl Uplink als auch Downlink vereint [11]. Ein DML verfügt als Nebeneffekt beim Senden über einen Chirp-Effekt [12], [13]. Dieser Chirp interagiert mit der chromatischen Dispersion (C-Band) der Glasfaser und erzeugt Träger-zu-Träger Mischung Übersprechen (SSII) nach einem direkt-detektierenden Empfänger [14]. Diese Störungen treten trotz der OFDM-typischen Robustheit gegenüber chromatischer Dispersion auf und erschweren den kosteneffizienten Einsatz OFDM-basierter Zugangsnetze. Der wesentliche Beitrag dieser Arbeit besteht in der Voraussage und Analyse der Auswirkungen von SSII auf Beeinträchtigungen der Signalqualität und dem Vorschlag und experimenteller Verifizierung von Kompensationstechniken.

Eine analytische Formulierung zur Voraussage des Signal-Rausch-Verhältnises (SNR), bei OFDM basierten DML Übertragungen wird angegeben. Die vorgeschlagene Methode ist in der Lage, den Einfluss einzelner Träger auf die Reduzierung des gesamten SNRs zu ermitteln. Die Intensitäts- und Frequenzantwort typischer DMLs sind ebenso in der Formulierung berücksichtigt. Sie werden in einem vereinfachten Lasermodell präsentiert. Die Voraussagen dieser Formulierung werden mithilfe von Experimenten unter verschiedenen Bedingungen validiert [15].

Des Weiteren wird ein Algorithmus zur Bit-und-Leistungsadaption präsentiert. Dieser kann die Leistung und Übertragunskapazität für jeden Träger auf dem Kanal anpassen, so dass ein maximaler Durchsatz erzielt wird [16].

Abschließend wird ein adaptiver Equalizer präsentiert. Das gezeigte Optimierungsverfahren erlaubt eine effiziente Kompensation von SSII [17]. Durch den Einsatz dieses optimierten Equalizers konnte in Experimenten eine Kapazitätssteigerung von $\simeq$33% erreicht werden [18].

Resumo

O crescimento das ligações de banda larga tem sido exponencial, e esta tendência manter-se-á no futuro previsível [1]. Uma rede de acesso é a ligação entre utilizadores e fornecedores de serviço, sendo um elemento chave no suporte do referido crescimento. Ao expandir a sua oferta de banda larga, um fornecedor de serviço tem, por um lado, de assegurar a sua migração através da compatibilidade com redes já existentes, e por outro lado, criar uma oferta atractiva para os consumidores. As redes de acesso são projectadas para suportar um grande número de utilizadores a diferentes distâncias do fornecedor de serviço, a viabilidade económica é obrigatória e é geralmente baseada no uso de Redes Ópticas Passivas (PONs) e componentes electro-ópticos de baixa complexidade (modulação/detecção directa), cujo desempenho pode ser melhorado através do uso de processamento digital de sinal com o intuito de mitigar limitações dos mesmos. Os mais recentes formatos de modulação também ajudam na obtenção de grande eficiência espectral assim como na distribuição avançada de sinal. Um destes formatos de modulação é Multiplexação por Divisão de Frequências Ortogonais (OFDM), que oferece um espectro compacto, é resiliente à dispersão cromática e possibilita a alocação flexível de subportadoras [2].

As redes já existentes usam a banda-C (1500nm) na ligação descendente e a banda-O (1330nm) na ligação ascendente [3]–[9]. A banda-C tem baixa atenuação apesar de ter elevada dispersão cromática [10]. A banda-O não tem practicamente dispersão cromática apesar da sua elevada atenuação [10], o que permite o uso de transmissores mais simples, tal como o Laser Directamente Modulado (DML). Os mais recentes sistemas PON devem permitir operação conjunta com redes já existentes. Por esta razão podem operar na banda-C tanto na ligação descendente como na ascendente [11]. Um DML tem *chirp* (variação da frequência de transmissão dependente da intensidade de emissão) como sub-producto da transmissão [12], [13]. O *chirp* interage com a dispersão cromática da fibra óptica (banda-C) criando Interferências de Mistura entre Subportadoras (SSII) num receptor de detecção directa [14]. Estas interferências podem ocorrer apesar da resiliência do OFDM à dispersão cromática e são uma das mais importantes limitações em sistemas de acesso economicamente viáveis baseados em OFDM. A principal contribuição deste trabalho é prever e analisar o impacto de SSII como limitação, propondo e verificando experimentalmente técnicas de mitigação.

Um modelo analítico capaz de prever a Relação Sinal-Ruído (SNR) para transmissão com DML baseada em OFDM é derivada. Este modelo tem a capacidade de determinar a contribuição de cada subportadora para a degradação da SNR. As respostas em intensidade e frequência do DML são incluídas na formulação através de um modelo simplificado de laser. As previsões desta formulação são validadas experimentalmente sob várias condições [15].

Um algoritmo de adaptação de bit-e-potência também é proposto, este algoritmo adapta a potência e capacidade de cada subportadora ao canal, maximizando assim a capacidade total de transmissão [16].

Finalmente um equalizador adaptativo é apresentado. Um processo de optimização capaz de conseguir mitigação eficiente de SSII é proposto [17]. Resultados experimentais demonstram um aumento de capacidade de $\simeq$33% ao usar o equalizador optimizado proposto [18].

Contents

Chapter 1

Introduction

In 2017, global average connection speed lied just over 7Mb/s [19] and has ever since been increasing. This value is still below 15.3Mb/s, which was deemed sufficient in 2013 [20]. By 2020, the minimum sufficient subscription speed is expected to rise exponentially to 165Mb/s [20]. Allied to this substantial growth in demand, the ubiquity of broadband access makes it even more pressing for telecommunication system providers to offer cost-effective access solutions to network operators.

1.1 Access Systems Concepts

An access network is the final transmission path between provider and subscriber. Optical access networks represent the current state of the art, enabling unprecedented data rates. These are also known as **F**ibre **t**o **t**he **X** (FTTX), a generic term defining how much of the network is composed of optical fibre. In fact, the replacement of copper with fibre commenced in the vicinity of the provider premises. It has been expanding throughout the network, reaching ever closer to the user.

Types of FTTX follow a nomenclature that indicates the point where fibre is terminated. These can be:

- FTTC - curb (kerb) - a street cabinet close to the user
- FTTB - building - brings fibre into the building, where the signal then relies on Ethernet to connect all the dwellings
- FTTH - home - fibre is connected directly to the home

Of these definitions only FTTH and FTTB have been standardized by the FTTH Council Global Alliance [21]. The shift from the cabinet type equipment (FTTC) to the home user one (FTTH) requires a new type of device known as **O**ptical **N**etwork **T**erminal (ONT) or **O**ptical **N**etwork **U**nit (ONU). The added optical capability increases the cost of devices even if signal processing requirements are similar to a legacy **D**igital **S**ubscriber **L**ine (DSL) router.

1.2 State of the Art in Optical Access Systems

Current optical access can be realized using two distinct network architectures. One uses a single fibre to connect the service provider's central office to each user, while the other sees the fibre split to interconnect several users. In the first architecture, named **A**ctive **O**ptical **N**etwork (AON), connections are possible only between active nodes. The second architecture uses a passive splitter to distribute signals sent from the central office to different users. Because of the presence of one, or more, passive devices (splitters) in the signal path, a network of this type is named **P**assive **O**ptical **N**etwork (PON). The biggest advantage of a PON is the lack of active components, i.e. reduced cost and footprint. The placement of passive devices is independent of the availability of electric power or space. This is allied to maintenance free operation, making PON an attractive alternative to a full active network. Interest in PON has led to an initial standardization and a quick evolution of standards defined by the **I**nternational **T**elecommunication **U**nion (ITU) and the **I**nstitute of **E**lectrical and **E**lectronics **E**ngineers (IEEE). The most recent PON standards can be seen in Table 1.1 ordered by year of first ratification. Here, the maximum downlink and

Definition	Year	Standard	Downlink/Uplink		Distance	Split
			Rate[Gb/s]	(λ)[nm]	[km]	Ratio
BPON	1998	G.983.1	1.24/0.62	1490/1300	20	1:32
GPON	2003	G.984.1	2.4/1.2	1490/1300	20	1:64
EPON	2004	IEEE 802.3ah	1/1	1490/1300	20	1:16
10G-EPON	2009	IEEE 802.3av	10/1	1577/1270	20	1:32
XG-PON	2010	G.987	10/2.5	1577/1270	20	1:64
NG-PON2	2013	G.989	40/10	1600/1530	20	1:64

Table 1.1: PON standards [3]–[9], [11].

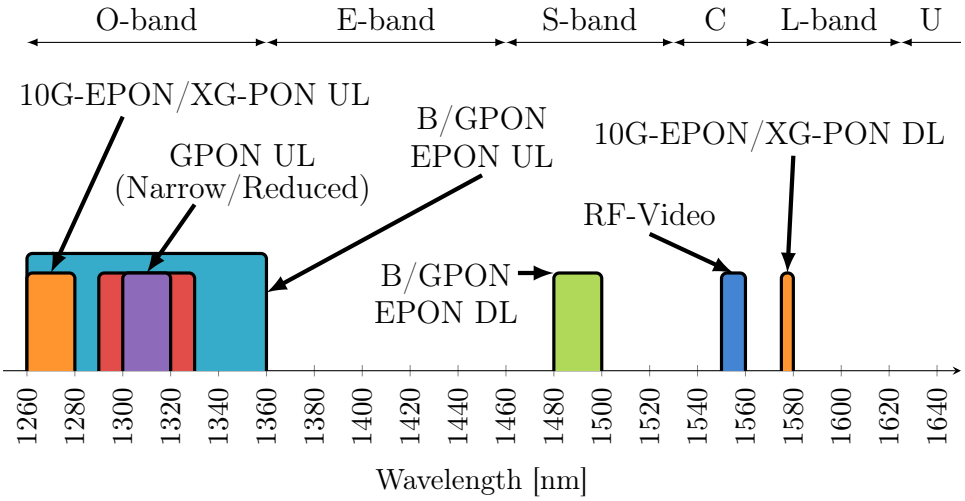

Figure 1.1: Wavelength plans of legacy PON systems [9].

uplink rates in the asymmetrical option of the standard are shown. Standards can support lower data rates and/or symmetrical operation. The minimum distance and minimum supported splitting ratio can also be seen. Splitting ratio is limited by the optical power budget, limiting the number of users.

A graphical representation of wavelength distribution among different standards is shown in Figure 1.1. The nomenclature used for each transmission band is also depicted. Of note is that the E-band is completely unused. The cause is apparent in Figure 1.2: legacy fibres exhibit high attenuation due to the presence of water vapour [10]. More recent fibres have low attenuation resulting from improvements in the manufacturing process.

1.3 PON Elements and Data Multiplexing

In the **C**entral **O**ffice (CO), fibre connection starts at the **O**ptical **L**ine **T**erminal (OLT) which manages the connection to multiple subscribers. The fibre terminates at the ONU/ONT, on the subscriber side, where conversion from the optical domain to the electrical domain and vice versa is performed.

Downlink and uplink transmissions support multiplexing. This can be performed either electrically or optically. Electrical multiplexing is the simplest variant, in which the ONU is responsible for selecting the correct signal [22]. In optical multiplexing each ONU is assigned a specific wavelength (**W**avelength **D**ivision **M**ultiple **A**ccess (WDMA) [23]). This can either be filtered at the ONU or at the passive

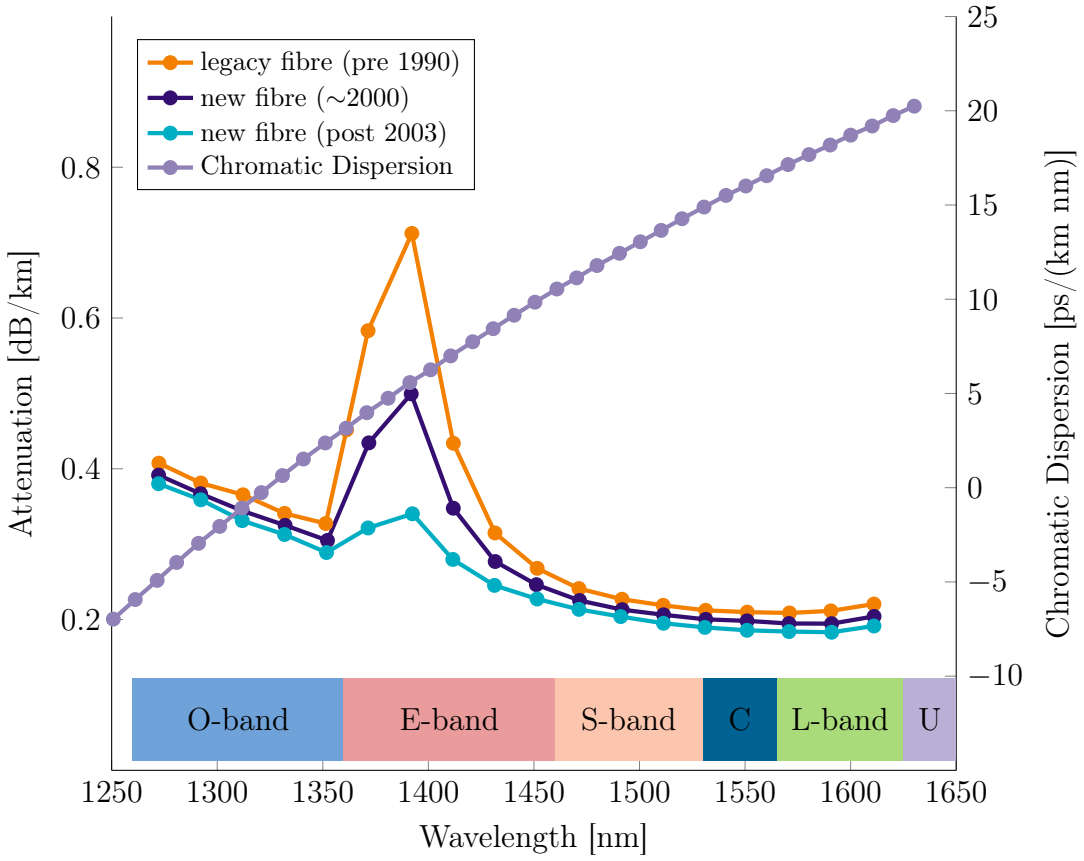

Figure 1.2: Standard single mode fibre attenuation and chromatic dispersion with transmission bands indication [9].

splitter (wavelength routing). Multiplexing in the optical domain has the added advantage of splitting ratio reduction for each wavelength, thus lowering insertion loss [22]. Not covered in this work is **S**pace **D**ivision **M**ultiple **A**ccess (SDMA) using multiple fibres, modes or cores. Mode and core-based SDMA systems are still in initial phases of development.

Electrical multiplexing can be performed either in the time or frequency domain. These can be defined by their generic terms: **T**ime **D**ivision **M**ultiplexing (TDM) and **F**requency **D**ivision **M**ultiplexing (FDM). Alternatively, terms more specific to access are used: **T**ime **D**ivision **M**ultiple **A**ccess (TDMA) and **F**requency **D**ivision **M**ultiple **A**ccess (FDMA). TDMA works by creating time slots that can be used for transmission. In the downlink direction, specific time intervals are assigned to specific ONUs. In the uplink direction each ONU transmits in its assigned time slot, requiring centralized control of all ONUs to achieve synchronization. **S**ub**c**arrier **M**ultiple **A**ccess (SCMA) (interchangeable with FDMA) works in the frequency domain by

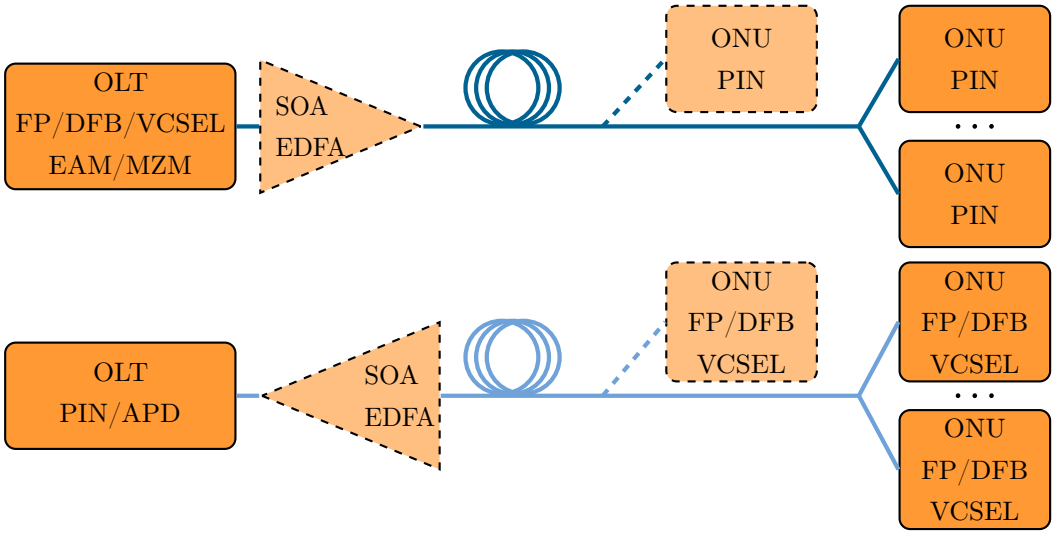

Figure 1.3: Typical PON downlink (top) and uplink (bottom) architectures showing possible ONU connection to a secondary remote node. Optional post/pre-amplification at the OLT is also shown.

assigning a specific **R**adio **F**requency (RF) carrier to a specific transmission.

The appearance of new services leads the uplink traffic to have a larger predicted growth than the downlink one [20]. For this reason there are provisions to offer symmetrical transmissions. Nevertheless, the current and future provisioned connection speeds are asymmetrical [20].

The main difference between uplink and downlink occurs for asymmetrical PONs as capacity requirements are different depending on the direction of transmission. These create a difference in equipment requirements. The OLT must transmit many high-bandwidth signals, whereas the ONU only transmits one low-bandwidth signal. As the OLT is shared by all ONU, its cost is diluted allowing for more expensive optical components and more complex signal processing. The ONU is cost-sensitive due to a large number of units employed in a PON.

As seen in Table 1.1 and Figure 1.1, uplink and downlink use separate bands (except for NG-PON2) allowing great tolerance in optical filters and laser frequency stability. The downlink is invariably chosen to be around 1550nm (Table 1.1), having the advantage of lower attenuation at the cost of higher **C**hromatic **D**ispersion (CD) (Figure 1.2). In terms of the receiver configuration, **D**irect **D**etection (DD) is the cost-effective choice, with the PIN photodiode in common use. In terms of the transmitter, a **D**irectly **M**odulated **L**aser (DML) is the most cost-effective

solution, more specifically a **F**abry-**P**erot (FP) laser. Systems making use of **D**irect **M**odulation (DM) and DD are referred to as **D**irect **M**odulation **D**irect **D**etection (DMDD). The FP laser has the disadvantage of having multiple longitudinal modes, thus suffering a higher transmission penalty in the presence of CD. Alternatively, a narrow spectrum, single longitudinal mode, DML can be used. Two examples are: the **D**istributed **F**eed**b**ack (DFB) laser and the lower powered, but more cost-effective, **V**ertical **C**avity **S**urface **E**mitting **L**aser (VCSEL). The low power of the VCSEL limits its usage in current PON networks.

At the OLT, more costly optical modulators can also be used: **E**lectro-**A**bsorption **M**odulator (EAM) or **M**ach–**Z**ehnder **M**odulator (MZM). Post-amplification can be performed either by a **S**emiconductor **O**ptical **A**mplifier (SOA) or by an **E**rbium-**d**oped **F**ibre **A**mplifier (EDFA) [24] as seen in Figure 1.3(top).

The uplink is commonly located around 1300nm (Table 1.1) in a band free from chromatic dispersion (Figure 1.2), allowing directly modulated FP lasers to be used. If the uplink band has enough bandwidth, as in the case of the 100nm available for legacy PON (B/G/EPON), **W**avelength **D**ivision **M**ultiplexing (WDM) can be used with FP lasers. Other cost-effective alternatives are to use a directly modulated DFB or VCSEL. The disadvantage of using this band is the higher attenuation, which increases the optical power demands of the transmitter. This can be overcome by using post-amplification at the OLT with an SOA or an EDFA. The latter is only possible for 1500nm uplink. Sensitivity can also be improved by using the more costly **A**valanche **P**hoto**d**iode (APD) [25], as seen in Figure 1.3(bottom).

A narrow emission spectrum is not the only transmitter characteristic imposed by dispersion in the downlink band, low chirp is also desirable [14], [26]. Cost-effective modulators commonly exhibit higher chirp: EAM to some extent and DML to a greater extent (depending on the design). This is not the case of an MZM, where the optical signal can be controlled in terms of its power and phase.

Future PONs will see coherent optical transmission [27] being used either due to bandwidth demands or due to reduced cost of components.

1.4 Modulation Formats for Optical Access

The initial modulation format used in PON was **O**n-**O**ff **K**eying (OOK) **N**on-**R**eturn-to-**Z**ero (NRZ). OOK is especially suited for use with a DML because the binary

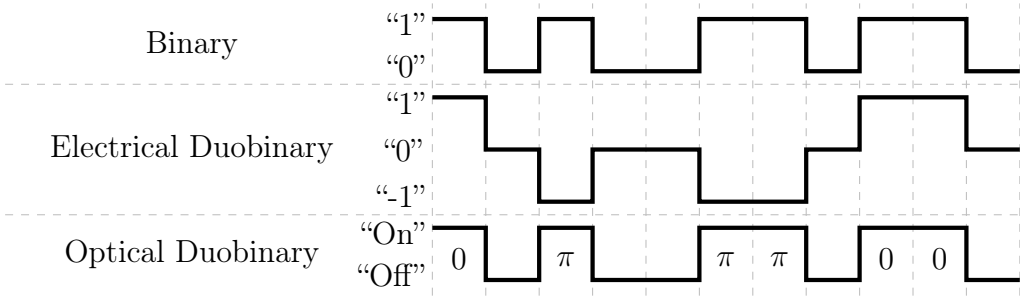

Figure 1.4: Binary signal (top), its corresponding electrical duobinary [29] (centre) and optical duobinary [30] (bottom) signals.

stream can simply be biased and fed to the laser. As the data-rate-per-wavelength requirements grow, two problems arise. The first is related to fibre dispersion [28] and the second to the cost increase in larger bandwidth optical transmitters. The effects of fibre dispersion can be alleviated by reducing signal bandwidth or by using a modulation format that is resilient to dispersion. The former can be accomplished with electrical duobinary, the latter with optical duobinary.

Electrical duobinary [29], [31] uses controlled **I**nter**s**ymbol **I**nterference (ISI) to produce a three level signal. By having half of the bandwidth, this signal is more resilient to dispersion for the same data rate. In this modulation format, the central level represents "zeros", the outer levels represent "ones" having alternate polarity when separated by an odd number of "zeros", as seen in Figure 1.4.

Optical duobinary [30] is an OOK signal in terms of intensity. Unlike an OOK signal, the optical phase of the "ones" is inverted when these are separated by an odd number of "zeros". Dispersion causes signal broadening of the "ones" pulses. When two "ones" pulses overlap, destructive interference cancels the signal. This modulation format requires phase control of the optical signal, thus requiring an MZM to be used.

Spectral efficiency can be further improved by using a multilevel modulation format such as **P**ulse **A**mplitude **M**odulation (PAM). Departing from baseband modulation formats, an electrical carrier can be modulated in: amplitude to produce **A**mplitude-**s**hift **K**eying (ASK), phase to produce **P**hase-**s**hift **K**eying (PSK) or both producing **Q**uadrature **A**mplitude **M**odulation (QAM). **C**arrierless **A**mplitude **P**hase Modulation (CAP) is similar to QAM but uses pulse shaping filters that can be implemented electrically [32].

FDM is achieved by combining several electrical modulated carriers. When several

CAP carriers are combined, the denomination changes to MultiCAP. One limitation of FDM is the necessity of guard bands to separate signals thus preventing interference between bands [33].

Two modulation formats dispense guard bands. **O**rthogonal **F**requency **D**ivision **M**ultiplexing (OFDM) ensures their orthogonality. **F**ilter **B**ank **M**ulti**c**arrier (FBMC) allows carriers to overlap in the frequency domain. By alternating I and Q transmission in adjacent carriers, interference is avoided [34].

1.5 Orthogonal Frequency Division Multiplexing

OFDM [35] has a long history outside the realm of optical communications [36]. In wireless communications, it has found a successful use in Wi-Fi networks [37], Wimax [38] and LTE [39]. It has also been implemented in digital audio broadcasting [40] and video content: terrestrial [41] and satellite for hand-held devices [42]. In the case of wired communications, it can be found in **A**symmetric **D**igital **S**ubscriber **L**ine (ADSL) [43], cable television [44], broadband power line communications [45], as well as in narrowband for smart grids [46].

1.5.1 OFDM for Optical Communications

Even though the first paper [47] on OFDM for optical communications dates back to 1996, only in 2001 would its robustness against chromatic dispersion be recognized [48], [49]. In 2006, three seminal papers established OFDM as a contender for use in long haul systems, two of them using DD [48], [49] and one using coherent detection [50]. Papers showing **I**ntensity **M**odulation **D**irect **D**etection (IMDD) transmission for PONs appeared not far after [51].

1.5.2 Motivation for OFDM

OFDM, due to its multicarrier architecture, is especially suited for implementation in access systems. This is because of the logical (bandwidth assignment) as well as physical (mitigation of impairments) advantages.

Having multiple subcarriers allied with TDM means that a finer granularity can be achieved in bandwidth sharing among users, where a user can have one or several subcarriers assigned, or several users share a single subcarrier. These are desired

characteristics of networks that adapt *on the fly*, ensuring that bandwidth is allocated to users when required.

OFDM also excels in channel adaptation due to its multicarrier nature. Transmission can be tailored to channel characteristics, maximizing data rates at frequencies that can support it while backing off at frequencies experiencing low **S**ignal-to-**N**oise **R**atio (SNR).

A physical advantage of OFDM, when compared to NRZ or PAM-based baseband modulations, is especially noted in C-band transmission. OFDM is less affected by CD, partially due to having many low speed subcarriers. Moreover, addition of a **C**yclic **P**refix (CP) contributes to higher resilience, however, at a capacity cost. Despite these advantages, an OFDM signal can still be affected by power fading, which manifests itself through signal cancellation at the receiver. This occurs as a result of CD-induced π radians phase shift between upper and lower optical side-bands after direct detection [52]. Subscribers located at different distances from the OLT will experience signal cancellation at different frequencies due to different accumulated CD. By taking power fading into consideration, subcarrier assignment can avoid this impairment altogether. When this is not possible, subcarriers can be disabled and their power can be transferred to other, less affected subcarriers.

Subcarriers can also be controlled independently, in terms of amplitude and number of bits-per-symbol, in what is known as bit-and-power loading. This form of pre-distortion is performed at the transmitter and allows signal adaptation to the channel.

Selected subcarriers can transmit a known sequence (pilot tones) aiding equalization at the receiver.

OFDM is spectrally efficient due to the possibility of using dense constellations. Due to low speed subcarriers, tight Nyquist filtering can be performed, further compacting the spectrum and enabling OFDM to work well in bandwidth-limited systems.

1.5.3 OFDM types for Optical Communications

The best performing but also most complex scheme is **C**oherent **O**ptical **OFDM** (CO-OFDM) [2]. Early experiments achieved 8Gb/s after 1000km [53] and 20Gb/s after 4160km [54]; far in excess of what is required for access systems. CO-OFDM can be implemented by using an IQ modulator to modulate the optical carrier performing

direct conversion. Alternatively an RF carrier used as **I**ntermediate **F**requency (IF) can be IQ modulated and then used to modulate the optical carrier. In both cases one, or more, MZM are used to control both the intensity and phase of the optical carrier. In order to also detect the phase of the optical carrier, a coherent receiver is required, that, in addition to the MZM increases system complexity, as well as cost. For this reason CO-OFDM is not considered in this work.

The alternative to CO-OFDM is **D**irect **D**etection **O**ptical **OFDM** (DDO-OFDM) providing gains in terms of cost-effectiveness but lacking the ability to discern the phase of the optical carrier. This type of OFDM is further divided into two classes: Linearly Mapped DDO-OFDM and Nonlinearly Mapped DDO-OFDM.

Linearly Mapped DDO-OFDM, as the name indicates, performs a linear mapping between the electrical and optical fields, where the RF spectrum is up-shifted to an optical frequency. **S**ingle **S**ide-**B**and OFDM (SSB-OFDM) is a form of linear mapping, where the RF or baseband signal modulates the **L**ower **S**ide-**B**and (LSB) or the **U**pper **S**ide-**B**and (USB) of the optical carrier. Since a photodiode is a square law detector, second order intermodulation terms will appear at the baseband after detection. These can be avoided by ensuring enough offset (akin to a guard band) is given to the OFDM signal relative to the optical carrier, so that after detection the nonlinear terms can be filtered out, in what is known as Offset SSB-OFDM [48]. The drawback of this approach is that no signal is transmitted in the guard band. By minimizing the guard band and accepting a penalty in terms of receiver sensitivity, the otherwise wasted bandwidth is reclaimed in what is known as baseband optical SSB-OFDM [55]. RF Tone-Assisted OFDM transmits signal in odd subcarriers alone, second order intermodulation terms land on frequencies of the, now suppressed, even subcarriers; this technique is known as subcarrier interleaving [56]. Finally, the iterative approach of Virtual SSB-OFDM [57] takes the received signal and processes it to reconstruct the second order intermodulation, this is then subtracted from the subsequent received signal which is processed again. Iterations succeed in order to mitigate second order intermodulation.

Nonlinearly Mapped DDO-OFDM aims to obtain linear mapping between the OFDM signal and optical intensity, instead of the field. As only optical intensity needs to be controlled, an EAM or even the more cost-effective DML can be used. As the photodiode detects the intensity of the optical signal, the linear mapping of the electrical field to the optical intensity will not cause second order intermodulation

after detection for an ideal optical transmission channel. Modulating the optical intensity has the consequence of creating two sidebands. In the presence of dispersion, frequency components of each sideband are delayed by different amounts causing destructive interference after detection [52]. This effect is the previously mentioned power fading. By transmitting in **S**ingle **S**ide-**B**and (SSB), the influence of dispersion on transmission can be overcome, this is known as compatible OFDM [58]. Due to the lack of second order intermodulation, there is no guard band required, making it spectrally efficient despite the added complexity of transmitting in SSB.

For short reach applications, such as access systems, dispersion is much smaller than for long haul systems. The focus can then be shifted to cost-effectiveness. To avoid using an RF carrier, a DFB laser is directly modulated with a real-valued OFDM signal, also known as **D**iscrete **M**ulti**T**one (DMT). This type of OFDM is known as adaptively modulated optical OFDM [59].

One limitation of using adaptively modulated optical OFDM in DMDD systems arises from the introduction of chirp in a transmission system with CD. Both interact, causing **F**requency **M**odulation (FM)-**A**mplitude **M**odulation (AM) conversion of the transmitted signal after detection [60], causing a reduction in the SNR of the system. This interference is referred to as **S**ubcarrier-to-**S**ubcarrier **I**ntermixing **I**nterference (SSII).

The systems analysed in this work use adaptively modulated optical OFDM, which for simplicity will be referred to as OFDM systems.

1.6 Outline

This work considers OFDM-based DMDD access systems operating in the C-band without amplification. Optical/electrical conversion is performed by DFB lasers and PIN photodiodes. For the considered systems two important impairments were identified: power fading and SSII. The former arising from CD and the latter from CD-induced FM-AM conversion of laser chirp.

The focus of this work is to provide a comprehensive understanding of the impairments in the considered systems. The goal is to develop impairment prediction and mitigation techniques. Validation of developed techniques is performed experimentally.

This work is outlined as follows: **Chapter 2** focuses in the presentation of key

technologies used in cost effective access systems, with special attention being devoted to OFDM.

In **Chapter 3**, transmission impairments are characterized. Initially, fibre related causes of such impairments are explored. Separate sections are devoted to power fading and SSII. Finally, an analytical formulation capable of predicting SSII-induced SNR degradation is derived and experimentally verified.

Chapter 4 presents equalization techniques for signal adaptation to the channel and SSII mitigation. The validity of the presented techniques is experimentally verified in terms of capacity increase arising from impairment mitigation.

Chapter 5 draws conclusions on the efficacy of proposed techniques for identification and mitigation of impairments in cost-effective OFDM-based access systems.

Chapter 2

Key Technologies

In this Chapter, key technologies and components for cost-effective OFDM-based access systems are presented. Initially, the focus is on modulation format concepts. This is followed by digital to electrical conversion. Finally, attention is devoted to electro/optical conversion components.

2.1 OFDM concepts

OFDM is a type of FDM with orthogonal carriers [33]. An OFDM signal is seen as a single carrier, its carriers are referred to as subcarriers. In FDM, overlapping carriers lead to interference and, as a consequence, degraded SNR. For this reason, FDM uses guard bands, empty frequency bands between carriers, decreasing spectral efficiency. OFDM subcarriers overlap but do not interfere as they are orthogonal, thus higher spectral efficiency is achieved.

2.1.1 Orthogonality

The orthogonality of OFDM subcarriers is achieved by making all subcarriers harmonic of the lowest frequency subcarrier. A multi-carrier signal $s(t)$ composed of N subcarriers ($s_k(t)$) can be described as:

$$s(t) = \sum_{k=1}^{N} s_k(t). \tag{2.1}$$

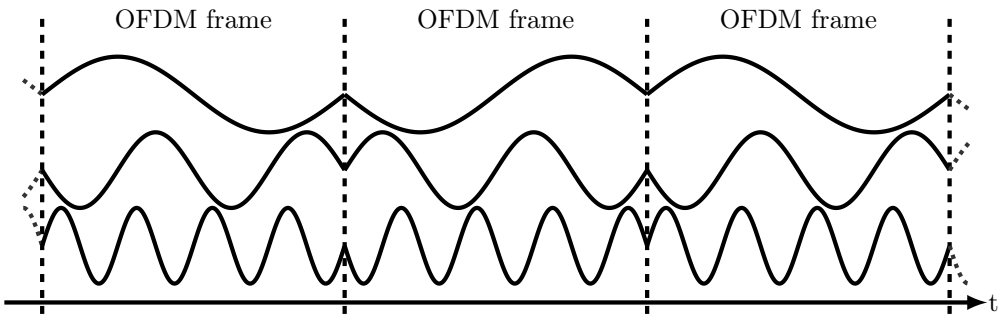

Figure 2.1: Exemplary OFDM frames showing three subcarriers with alternating phase modulation for different frames.

A subcarrier can be represented by either a sine or a cosine with unitary amplitude. Since both are orthogonal, they can be used simultaneously:

$$s_k(t) = \cos(\omega_k t) - \sin(\omega_k t). \tag{2.2}$$

To define orthogonality it is sufficient to take one quadrature component, in this case a cosine:

$$s_k(t) = \cos(\omega_k t). \tag{2.3}$$

In order to ensure that any two subcarriers (for example s_2 and $s_k\ \forall k > 2$) at angular frequencies ω_2 and ω_k are orthogonal, their inner, or scalar, product (integral of the product) over one cycle of the lowest frequency subcarrier above 0Hz (**D**irect **C**urrent (DC)) must be zero:

$$\int s_2(t) s_k(t)\,\mathrm{d}t = 0 \quad \forall k > 2, \tag{2.4}$$

which can be rewritten as:

$$\int_0^{\frac{2\pi}{\omega_2}} \cos(\omega_2 t)\cos(\omega_k t)\,\mathrm{d}t = 0 \quad \forall k > 2. \tag{2.5}$$

The orthogonality condition holds for integer multiples of the lowest frequency subcarrier: ω_k/ω_2 must be an integer.

The integration interval introduces the notion of an OFDM frame. It contains one cycle of the lowest frequency subcarrier above DC and an integer number of cycles of all other higher frequency subcarriers. To guarantee the orthogonality of the entire OFDM signal, the orthogonality condition must hold for each OFDM frame.

ω_k – k subcarrier angular frequency

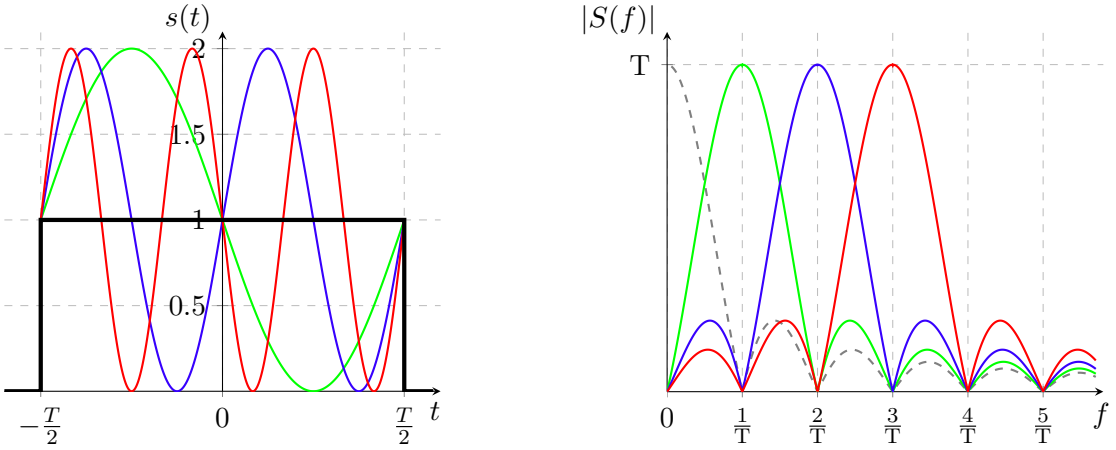

Figure 2.2: Time (left) and frequency (right) domain representations of an OFDM frame limited by a rectangular function (left black) leading to a sinc frequency response for each subcarrier. Also included is a DC (0Hz) subcarrier.

2.1.2 OFDM Frame

The OFDM frame period (T) defines the OFDM symbol length. This interval is the same as the period of the lowest frequency subcarrier, as seen in Figure 2.1. The relation between the frame period (T) and subcarrier frequencies (ω_k) is given by [33]:

$$\omega_k = \frac{2\pi(k-1)}{T}, \ k = 1, 2, \cdots, N, \tag{2.6}$$

with the first subcarrier being the DC subcarrier (ω_1=0).

We can now define a general orthogonality condition between any two subcarriers based on the frame period. The index p denoting a second subcarrier ($\omega_k \neq \omega_p$) is introduced:

$$\int_0^T s_k(t)s_p(t)\,\mathrm{d}t = 0 \quad \forall k, p = 1, 2, \cdots, N, \ k \neq p. \tag{2.7}$$

The amplitude and phase of each subcarrier can be changed for the subsequent frame. Amplitude and phase combinations are dictated by the modulation format which defines the encoding of bits to be transmitted. Each amplitude and phase combination can represent one or more bits and is known as a symbol. Subcarrier amplitude and phase are constant inside each OFDM frame. The number of transmitted symbols per OFDM frame is equal, or smaller, than the number of subcarriers. Consequently, the symbol rate is:

$$R_s = \frac{N}{T}. \tag{2.8}$$

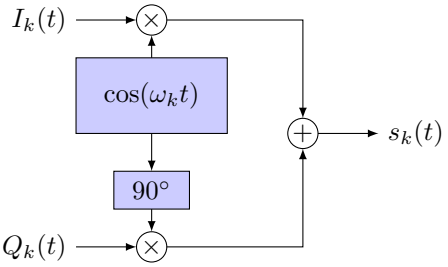

Figure 2.3: Single subcarrier, IQ modulator based, QAM transmitter.

Symbol changes between frames lead each frame of the OFDM signal to behave as a rectangular pulse in the time domain. In the frequency domain each subcarrier is represented by a sinc function:

$$\sum_{k=1}^{N} \cos\left(\frac{2\pi(k-1)t}{T}\right) \operatorname{rect}\left(\frac{t}{T}\right) \xrightarrow{\mathcal{F}} \sum_{k=1}^{N} \delta\left(f - \frac{k-1}{T}\right) * T \operatorname{sinc}(fT). \tag{2.9}$$

Figure 2.2 shows an OFDM frame containing four subcarriers (including DC) both in time and frequency domains. Even though each subcarrier has a large frequency spread, nulls at other subcarrier frequencies ensure that there is no interference between subcarriers, a by-product of orthogonality.

2.1.3 Quadrature

A subcarrier controllable in both amplitude (A) and phase (ϕ) can be defined as:

$$s_k(t) = A\cos(\omega_k t + \phi). \tag{2.10}$$

This is equivalent to having two waves in quadrature as in Eq. (2.2) [33]. The amplitude of these waves can be controlled to represent coordinates of points on a plane: one axis is given by the in-phase (I) component, whereas the other is given by the quadrature (Q) component. Using this notation, possible symbols can be defined as a grid in the complex plane, in what is known as a constellation. Due to the fact that cosine and sine are in quadrature, this modulation type is known as QAM. Using the notion of I and Q symbols controlling the modulation (IQ modulation) of

rect – rectangular function
$\xrightarrow{\mathcal{F}}$ – Fourier transform
$*$ – convolution
δ – Dirac delta function
sinc – normalized sinc function: $\operatorname{sinc}(x) = \sin(\pi x)/(\pi x)$ where $\operatorname{sinc}(0)=1$

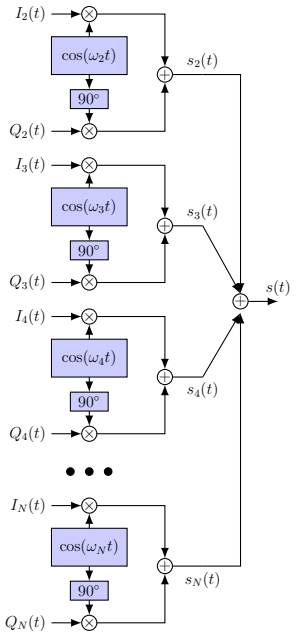

Figure 2.4: OFDM transmitter based on separate IQ modulators for each subcarrier.

each k-th orthogonal subcarrier, a QAM modulated signal can be represented as:

$$s_k(t) = I_k(t)\cos(\omega_k t) - Q_k(t)\sin(\omega_k t). \tag{2.11}$$

A schematic of a QAM modulated subcarrier can be seen in Figure 2.3. By combining several subcarriers, a full OFDM signal can be created:

$$s(t) = \sum_{k=1}^{N} I_k(t)\cos(\omega_k t) - Q_k(t)\sin(\omega_k t). \tag{2.12}$$

An OFDM transmitter can be seen in Figure 2.4. This realization requires a separate oscillator and modulator arrangement for each subcarrier, an impractical and costly manner to generate OFDM signals.

2.1.4 DFT Implementation

OFDM resilience to channel dispersion increases for large numbers of subcarriers [2]. Achieving a large subcarrier count presents a complexity challenge if separate transmitters are used for each subcarrier (Figure 2.4). **F**ast **F**ourier **T**ransform (FFT) algorithms allow OFDM to be efficiently generated by means of a **D**iscrete **F**ourier **T**ransform (DFT) [61]. Using Eq. (2.12) a real-valued signal is produced and can be directly transmitted, due to $I_k(t)$ and $Q_k(t)$ being real. Noting that:

$$e^{j\omega t} = \cos(\omega t) + j\sin(\omega t), \tag{2.13}$$

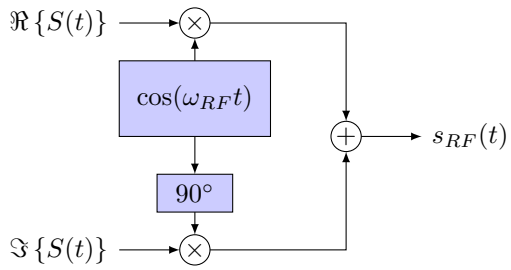

Figure 2.5: Quadrature modulation of a complex baseband signal.

the notation of Eq. (2.12) can be changed to the equivalent phasor representation:

$$s(t) = \Re\left\{\sum_{k=1}^{N}(I_k(t) + jQ_k(t))e^{j\omega_k t}\right\}. \tag{2.14}$$

Subcarriers are generated directly at the desired RF frequency. This is not always possible due to hardware limitations. The alternative is to generate subcarriers at baseband frequencies which will then be up-converted to an RF frequency (ω_{RF}). There are two options for up-conversion: multiplication with an RF carrier or IQ modulation. The latter uses less bandwidth than the former but requires the generation of both the I and Q baseband signals. Appendix C describes both types of up-conversion as well as where different baseband subcarriers land when up-converted.

The complex baseband signal is represented by:

$$S(t) = \sum_{k=1}^{N}(I_k(t) + jQ_k(t))e^{j\omega_k t}, \tag{2.15}$$

to perform up-conversion, an IQ modulator similar to the QAM transmitter of Figure 2.3 can be used. Instead of symbols, the real and imaginary parts of $S(t)$ in Eq. (2.15) are fed to the in-phase and quadrature arms respectively. This can be written as [2]:

$$s_{RF}(t) = \cos(\omega_{RF}t)\Re\{S(t)\} - \sin(\omega_{RF}t)\Im\{S(t)\}, \tag{2.16}$$

or simply as:

$$s_{RF}(t) = \Re\left\{S(t)e^{j\omega_{RF}t}\right\}. \tag{2.17}$$

The schematic of this type of modulator can be seen in Figure 2.5. The expression of Eq. (2.15) can also be written in terms of frequency (f_k) instead of angular frequency (ω_k):

$$S(t) = \sum_{k=1}^{N}(I_k(t) + jQ_k(t))e^{j2\pi f_k t}. \tag{2.18}$$

The relation between baseband subcarrier frequencies and frame period is defined similarly to Eq. (2.6):

$$f_k = \frac{k-1}{T},\ k = 1, 2, \cdots, N. \tag{2.19}$$

As the first subcarrier (k=1) is at DC, the second baseband subcarrier (k=2) defines the frame period. The continuous signal of Eq. (2.18) can be sampled at instants t=t' T/N, where t' is a discrete time index [33]. The digitized signal of Eq. (2.18) is:

$$S[t'] = \sum_{k=1}^{N} (I_k[t'] + jQ_k[t'])e^{j2\pi f_k t' T/N},\ t' = 0, 1, 2, 3, \cdots, \tag{2.20}$$

it is possible to replace the subcarrier frequency using Eq. (2.19):

$$S[t'] = \sum_{k=1}^{N} (I_k[t'] + jQ_k[t'])e^{j2\pi (k-1) t'/N},\ t' = 0, 1, 2, 3, \cdots, \tag{2.21}$$

where $S[t']$ is the **i**nverse **D**iscrete **F**ourier **T**ransform (iDFT), at each discrete time t', of the symbols of all subcarriers [33]:

$$S[t'] = \sum_{k=1}^{N} (I_k[t'] + jQ_k[t'])e^{j2\pi (k-1) t'/N} = \mathcal{F}^{-1}[t'] \left\{ \sum_{k=1}^{N} (I_k[t'] + jQ_k[t']) \right\}. \tag{2.22}$$

The iDFT converts the symbols of each subcarrier at its input into a time domain complex OFDM signal. The output of the iDFT has the same amount of samples (time domain) as the number of subcarriers. For this reason the maximum representable frequency (Nyquist frequency) is the subcarrier of index k=1+$N/2$ (assuming an even number of subcarriers). Subcarriers with indexes k>1+$N/2$ represent negative frequencies after up-conversion, causing them to have a frequency lower than ω_{RF}. The real and imaginary outputs of the iDFT can be fed to an IQ modulator as the one in Figure 2.5. The details on where a subcarrier, of a given index k, lands after up-conversion are provided in Appendix C.

2.1.5 Discrete Multitone

Using special subcarrier encoding it is possible to cause the output of the iDFT ($S[t']$) to have no imaginary component, being therefore real-valued. Such a signal has all its baseband subcarriers modulated both in amplitude and phase.

$\mathcal{F}^{-1}[t']$ – inverse discrete Fourier transform

$1+\cos(\omega_2 t') + \cos(\omega_3 t') + \cos(\omega_4 t') \overset{(i)DFT}{\Leftrightarrow}$

DC	ω_2	ω_3	ω_4	$\omega_{Nyq.}$	$-\omega_4$	$-\omega_3$	$-\omega_2$

Figure 2.6: Fourier transform representation in terms of angular frequencies of a real-valued signal using (i)DFT.

A real-valued signal can be generated using an iDFT if it has Hermitian symmetry in the frequency domain. To achieve this, only subcarriers up to the index $k = N/2$ (assuming an even number of subcarriers) are considered. The remaining indexes are populated by the same symbols, but complex conjugated and in the inverse order, as seen in Figure 2.6. For this reason, the size of the DFT/iDFT is the double of the number of subcarriers (assuming an even number of subcarriers).

A signal of this type is denominated **D**iscrete **M**ulti**T**one (DMT), a real-valued baseband version of OFDM. The generated baseband signal can be used in optical **I**ntensity **M**odulation (IM) systems without requiring up-conversion. The subcarrier at DC is usually discarded in optical IM systems as it would affect the transmitter biasing.

2.1.6 PAPR and Clipping

The OFDM signal is composed of many tones. Their amplitudes can add to create signal peaks that are significantly higher in amplitude than the signal average. This is denominated as **P**eak-to-**A**verage **P**ower **R**atio (PAPR) which is defined as being the ratio of the maximum signal peak power to the average signal power [2]:

$$PAPR = \frac{max\{|s(t)|^2\}}{E\{|s(t)|^2\}}. \tag{2.23}$$

The size and occurrence of these peaks depend on several factors: bit sequence, modulation format and number of subcarriers.

OFDM has typically high PAPR [2]. Therefore the driving electrical signal must be adjusted carefully to take peaks into account instead of the signal average, thus worsening SNR. In addition, very large peaks can cause distortions as the signal is outside electrical/optical components' linear behaviour. The severity of these effects depends on how high the probability of the occurrence of the high peaks is. Using the complementary cumulative distribution function, the probability ($PAPR_P$) of PAPR exceeding a given value (ζ) is given by [2]:

$$PAPR_P = P(PAPR > \zeta). \tag{2.24}$$

PAPR can be reduced through signal distortion at the cost of SNR [2]. The PAPR peaks are eliminated by clipping. More specifically an amplitude threshold, above which the signal is discarded, can be defined. Setting a threshold can be a complex design task due to the aforementioned random nature of the signal. Therefore, it is desirable that the signal is normalized before applying clipping. Normalization can be performed relatively to the clipping threshold, where the probability of threshold crossing is defined as clipping probability ($clip_P$):

$$clip_P = P(|s(t)| > clip_{th}). \tag{2.25}$$

The input signal is $s(t)$ and $clip_{th}$ is the clipping threshold. By using this measure, clipping is directly related to the actual signal and therefore it does not depend on the bit sequence or modulation. The optimum value of $clip_P$ can be analytically derived [26], [62] or experimentally inferred.

Distortion free PAPR reduction can also be achieved through special coding at the cost of capacity [2].

2.1.7 Cyclic Prefix

At the receiver, a DFT is used to convert OFDM frames from time domain to symbol representation. This requires two types of alignment: frame alignment with the DFT as well as alignment between subcarriers. Frame alignment guarantees that a single frame is processed by the DFT in its entirety. Methods to achieve this type of alignment are available for single [2] and multiple transmitters sharing a frame (uplink) [63]; both are out of the scope of this work. Subcarrier alignment guarantees that all subcarriers change their modulation (amplitude/phase) to the next symbol in unison at the frame boundaries, preserving orthogonality. Alignment is lost when subcarrier frequencies have different propagation speeds, as experienced in a dispersive channel. This leads to increased noise, as part of another frame, and consequentially another symbol will overlap with the current frame causing **I**nter**s**ymbol **I**nterference (ISI) due to **I**nter**c**arrier **I**nterference (ICI).

A case where orthogonality would not be lost in a dispersive channel occurs if each subcarrier consecutively transmitted the same symbol. For this specific case, a delay in one of the subcarriers relative to others would have no impact as the orthogonality condition is not lost. This strategy is used to counteract the effects of a dispersive channel in OFDM. Each symbol is extended in time, the added symbol length is

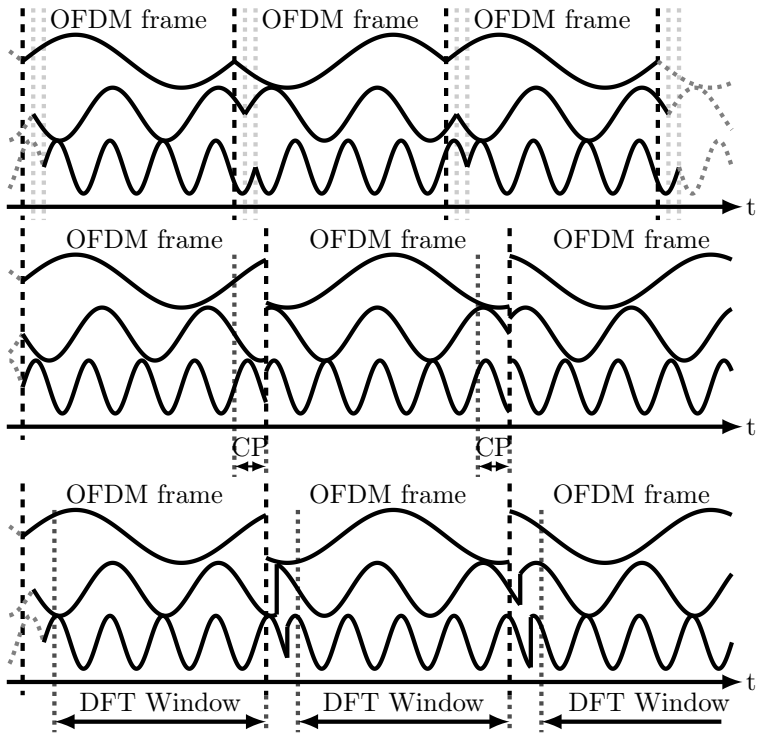

Figure 2.7: Top: OFDM signal without Cyclic Prefix (CP) at the receiver showing the impact of different propagation speeds for different subcarriers, for example due to CD. Middle: The OFDM signal with added CP at the transmitter. Bottom: OFDM signal with CP at the receiver showing that the DFT observation window contains no symbol transitions. The DFT observation window is the same size as the frame without CP. The phase difference between consecutive symbols is π radians.

known as **C**yclic **P**refix (CP). When a subcarrier is delayed, the signal inside the DFT observation window is the extension of the current symbol and one of the next or previous frame symbols. The CP adds redundancy to the signal, and consequently lowers total capacity. The effect of adding CP can be seen in Figure 2.7.

The amount of CP needed depends on the CD-induced delay relative to the frame size. Long frames require a smaller CP (percentage-wise) reducing capacity loss. Long frames, also seen as slower subcarriers, are more resilient to CD. This advantage is achieved at the cost of complexity, as frame enlargement is achieved by increasing the number of subcarriers.

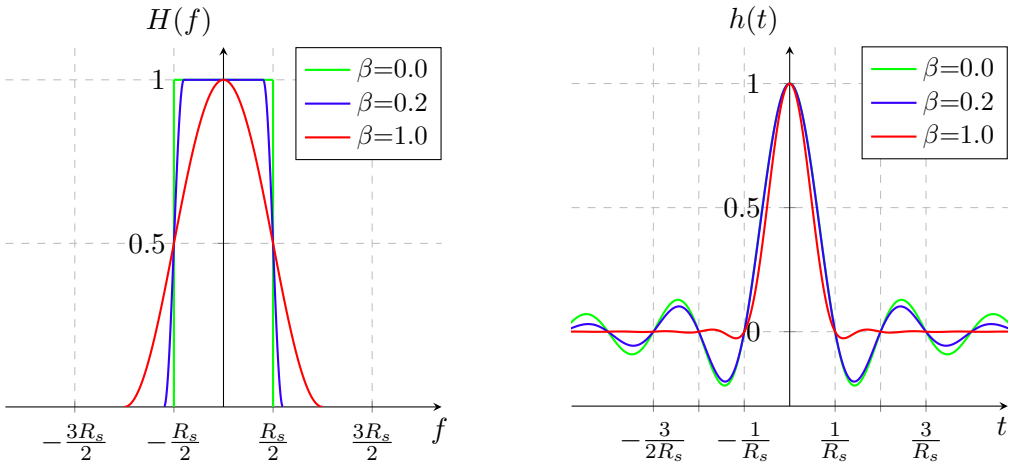

Figure 2.8: Frequency (left) and time domain (right) transfer functions of a raised cosine filter for several roll-off (β) values.

2.1.8 OFDM Windowing

As stated in Section 2.1.2, the rectangular function nature of OFDM frames leads to a sinc function in the frequency domain. As shown in Figure 2.2, subcarrier side-lobes extend beyond the frequency interval defined by the subcarrier frequencies. The total bandwidth can be confined through the use of windowing. This technique smooths frame transitions in the time domain to reduce the side-lobes of the OFDM signal in the frequency domain. Several windowing functions can be used [2], to give a few examples: Kaiser, Blackman–Harris and raised cosine. The raised cosine function has frequency and time domain transfer functions [64]:

$$H(f) = \begin{cases} 1, & 0 \leq |f| \leq (1-\beta)\frac{R_s}{2} \\ 0.5\left(1-\sin\left(\frac{\pi}{\beta R_s}\left(|f|-\frac{R_s}{2}\right)\right)\right), & (1-\beta)\frac{R_s}{2} \leq |f| \leq (1+\beta)\frac{R_s}{2} \\ 0, & (1+\beta)\frac{R_s}{2} \leq |f| \end{cases}, \tag{2.26}$$

$$h(t) = \begin{cases} 1, & |t| = 0 \\ \frac{\pi R_s}{4}\operatorname{sinc}\left(\frac{\pi}{2\beta}\right), & |t| = \frac{1}{2\beta R_s} \\ R_s \operatorname{sinc}\left(R_s t\right)\frac{\cos(\pi\beta R_s t)}{1-(2\beta R_s t)^2}, & |t| \neq \frac{1}{2\beta R_s} \wedge |t| \neq 0 \end{cases}. \tag{2.27}$$

R_s – symbol rate (N/T)
β – roll-off factor
T – OFDM frame period
sinc – normalized sinc function: $\operatorname{sinc}(x) = \sin(\pi x)/(\pi x)$ where $\operatorname{sinc}(0)=1$

This function has the advantage of not affecting subcarrier orthogonality [65]. Spectrum compactness can be controlled by the roll-off factor (β) [64], as seen in Figure 2.8. A very compact spectrum can be achieved by setting β=1, which also leads to a filter that is complex to implement. Raised cosine windowing can be applied by distributing the filter between the transmitter and receiver to create a matched filter. OFDM transmissions in this work use matched filtering (raised cosine) with β=0.2, unless noted otherwise.

2.2 AD/DA Conversion

The usage of DFT provides convenient means of generating OFDM signals. Being performed in the digital domain, it can be combined with advanced signal processing. A necessary component to bridge the gap between digital and analogue domain are the converters: **A**nalogue to **D**igital **C**onverter (ADC) and **D**igital to **A**nalogue **C**onverter (DAC).

The effect that converters have on system performance depends on their limitations in terms of the following parameters: bandwidth, linearity and resolution. Resolution is expressed in n number of bits, allowing 2^n levels to be represented. Parameters dictate how cost-effective a given converter is. The trade-off between sampling rate and resolution [62] has also to be considered. Low sampling rate limits OFDM symbol rate, whereas limited resolution imposes an error floor due to quantization noise. This noise is minimized whenever the **F**ull **S**cale **R**ange (FSR) of the converter is used. For the DAC case, this is achieved by normalizing the signal, thus ensuring that all levels (FSR) are used. The ADC case requires setting the appropriate electrical pre-amplifier gain. High PAPR causes the largest peak to occupy most of the FSR, reducing the resolution available for most of the signal samples. As shown in Section 2.1.6, clipping can be used to remove large peaks and allow the signal to use the entirety of the DAC levels (FSR). Optimal clipping represents a trade-off between clipping noise and quantization noise [26].

Low amplitude subcarriers are more affected by quantization noise as these use less than the FSR. At the transmitter (DAC) equalization can be performed to ensure that quantization noise is equalized for all subcarriers. The power distribution of subcarriers at the receiver (ADC) is dependent on the channel characteristics. It is desirable to have all carriers with the same amplitude at the transmitter and

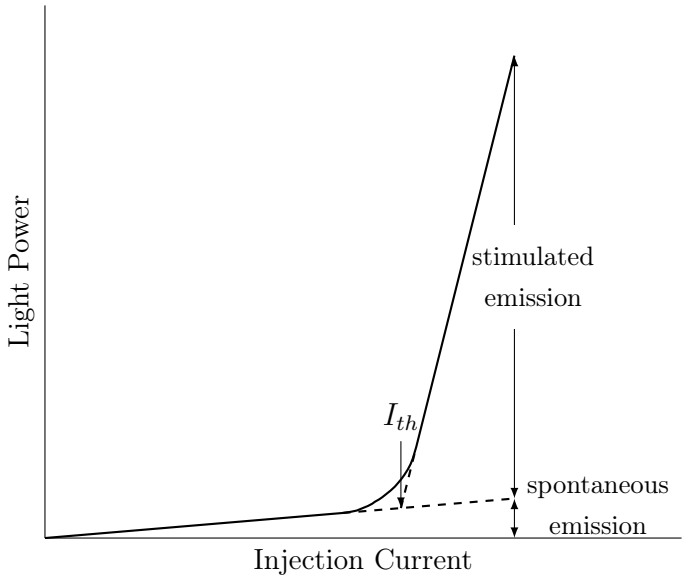

Figure 2.9: Output power vs. current characteristics of a laser diode [12].

receiver (assuming no bit loading) but this is not always possible. For instance, a low-pass channel attenuates high frequency subcarriers, these will suffer an SNR penalty due to limited resolution. By pre-emphasising the high frequency subcarrier at the transmitter, the effects of the low-pass channel can be mitigated. This is done at the cost of low frequency subcarriers, which will now have an SNR penalty at the transmitter. The SNR penalty can be equally distributed among all subcarriers by the use of power loading, i.e. independent control of subcarrier powers that enables high SNR subcarriers to provide power to low SNR ones.

2.3 Directly Modulated Lasers

The term laser originates from an acronym for **L**ight **A**mplification by **S**timulated **E**mission of **R**adiation. As the name indicates, stimulated emission is used to perform optical amplification and emit (ideally) monochromatic light.

A laser is composed of an optical cavity containing a gain medium. The optical cavity provides feedback by confining most of the photons to the cavity where they are multiplied by the gain medium.

Energy is provided to the gain medium through pumping, which is commonly performed by a light source or by an injection current (in semiconductor lasers). Pumping causes excitation of atoms of the gain medium in the case of gas lasers.

For semiconductor lasers, electrical bias causes the injection of electrons and holes in the active layer. These form electron-hole pairs, known as carriers. Carriers can recombine without external influence (spontaneously) or due to the influence of photons. Spontaneous recombination occurs at the carrier recombination rate (γ_e). The number of carriers inside the cavity (carrier population) is governed by the rate equation [13]:

$$\dot{N} = \frac{I}{q} - \gamma_e N - GP, \tag{2.28}$$

the first term represents carrier injection, the second term spontaneous carrier recombination and the final term carrier depletion due to stimulated emission.

Photon-induced recombination creates a new photon (copy of the influencer) in a process known as stimulated emission. Spontaneous radiative recombination also generates a photon in a process known as spontaneous emission. A photon is lost when it is absorbed by material imperfections inside the gain medium or when it leaves the cavity (generating laser output). This occurs at the photon decay rate (γ_p). A photon can also be absorbed by the gain medium and generate a carrier, in this scenario even though a photon is lost, its energy is stored. This energy can be used to generate a similar photon, a lower energy one or be completely lost. The number of photons inside the cavity (photon population) is governed by the rate equation [13]:

$$\dot{P} = (G - \gamma_p)P + R_{sp}. \tag{2.29}$$

For small injection currents, the number of carriers are small and spontaneous emission (R_{sp}) dominates. Increases in injection current lead to modest increases in the output of the laser. Still in this regime, when enough carriers are available (due to increased current), enough photons are generated to compensate loss in the gain medium. At this point the gain medium is said to be optically transparent (G=0) [13]. Due to scattering losses and photons escaping the cavity, loss still dominates; further increases in the carrier population lead to increases in gain up to the point where stimulated emission can be sustained. At this point generated photons match the

---

I – injection current
q – magnitude of the electron charge
γ_e – carrier recombination rate
N – carrier population
G – nonlinear gain
P – photon population
γ_p – photon decay rate
R_{sp} – spontaneous emission rate

losses, it is known as the laser threshold and the necessary injection current is the threshold current (I_{th}). From this point on, further increases in current do not lead to carrier population increases as these are quickly consumed by the large photon population inside the cavity. Similarly, the gain is constant matching the losses. Carrier population and gain are said to be clamped causing laser power to increase almost linearly with current, as seen in Figure 2.9.

Changes in the carrier population, and to a lower extent the photon population, lead to variations of the refractive index of the gain medium, causing phase changes in the laser output. These phase changes can be related to the carrier density and consequently to the gain by the linewidth enhancement factor α_c, also known as α-factor. The name of the parameter arises from the fact that laser linewidth is increased due to coupling between intensity and phase. Laser emission frequency (ω_0) is altered by gain medium refractive index changes. Phase is governed by the rate equation [13]:

$$\dot{\phi} = -(\omega_0 - \omega_{th}) + \frac{1}{2}\alpha_c(G - \gamma_p). \tag{2.30}$$

2.3.1 Modulation

As seen before, changes in laser injection current lead to changes in the laser output. These changes are linear above threshold. They can be used to encode information, being the laser referred to as a DML. This modulation process controls light intensity, making it a type of IM.

Usually a biasing current (DC) is initially defined (I_{bias}). It sets the power of the laser carrier to be modulated. Current changes (**A**lternating **C**urrent (AC)) will be directly translated into changes in the optical power. The ratio of the AC current change to the DC bias change is the modulation index (m), more specifically defined as [66]:

$$m = \frac{\Delta I_{mod}}{I_{bias} - I_{th}}. \tag{2.31}$$

ω_0 – lasing mode frequency
ω_{th} – lasing mode frequency at threshold
α_c – linewidth enhancement factor, or α-factor
G – nonlinear gain
γ_p – photon decay rate
m – modulation index
ΔI_{mod} – variation of the modulation current
I_{bias} – bias current
I_{th} – threshold current

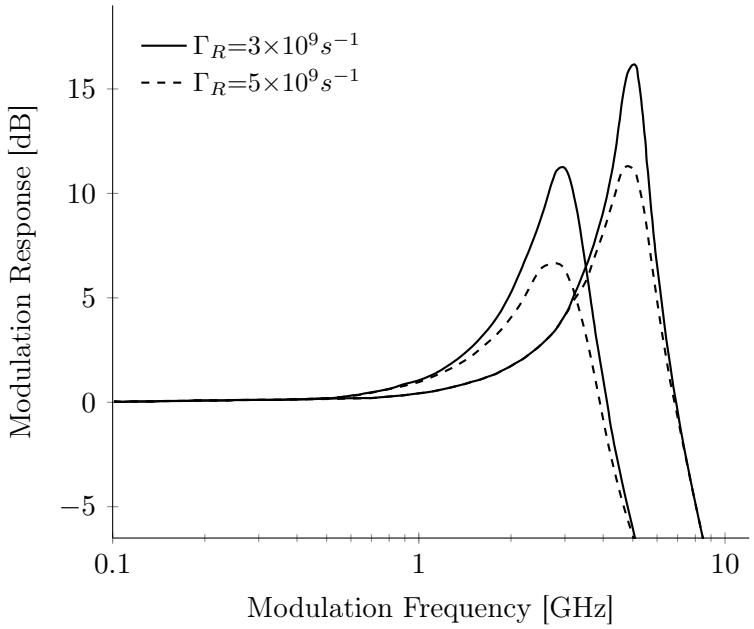

Figure 2.10: Calculated small-signal modulation response showing the relaxation oscillation peak at Ω_R and the dependence of the peak height on the relaxation oscillation decay rate Γ_R [13].

2.3.2 Small Signal Modulation

One method to characterize the laser modulation response is to use small signal analysis. This method is based on using low modulation index ($m \ll 1$) sinusoids with a wide frequency range at several biasing points. The resulting laser response is then analysed in order to infer its characteristics. The obtained response can be compared to the one obtained from analytical equations.

Intensity Modulation

The intensity response can be analytically derived by linearising laser rate equations. This derivation is performed in Appendix D. The intensity modulation equation

defines the frequency-dependent modulation response of the laser [13]:

$$\Delta_p(\omega) = \frac{\frac{\partial G}{\partial N} P I_p/q}{\left(\left(\omega^2 - \Omega_R^2 - \Gamma_R^2\right)^2 + 4\omega^2\Gamma_R^2\right)^{1/2}}. \tag{2.32}$$

The response is flat for low frequencies, $\omega \ll \Omega_R$ and shows a peak (ω_{pk}) at the resonance frequency close to Ω_R. Γ_R controls the ratio between the peak power and the flat portion of the low frequency response, $\Delta_p(\omega_{pk})/\Delta_p(0)$. This dependence can be seen in Figure 2.10. An approximate value for this ratio can be calculated using Eq. (2.32) by assuming that $\Gamma_R \ll \Omega_R$ [13] and $\omega_{pk} = \Omega_R$:

$$\frac{\Delta_p(\omega_{pk})}{\Delta_p(0)} \cong \frac{\Omega_R}{2\Gamma_R}. \tag{2.33}$$

Laser bandwidth is defined as the frequency where the modulation response is 3dB below the modulation response at DC. Frequencies beyond the laser bandwidth can still be used for transmission, albeit at a power penalty.

With intensity modulation there is also an associated frequency-dependent phase shift defined by [13]:

$$\theta_p(\omega) = \arctan\left(\frac{2\omega\Gamma_R}{\omega^2 - \Omega_R^2 - \Gamma_R^2}\right). \tag{2.34}$$

Frequency Modulation

Direct laser modulation has frequency modulation as a side effect. This is known as laser chirp.

Laser modulation is performed through changes in injection current, which in the dynamic regime cause variations in carrier density. As seen before, these lead to a phase change of the transmitted light.

Laser chirp is not only modulation amplitude-dependent but also frequency-

---

$\frac{\partial G}{\partial N}$ – gain derivative relative to the carrier population
P – photon population
I_p – peak value of the modulation current
q – magnitude of the electron charge
Ω_R – angular frequency of the relaxation oscillation peak
Γ_R – relaxation oscillation decay rate

dependent, and is defined by [13]:

$$\Delta_f(\omega) = \frac{\alpha_c I_p \frac{\partial G}{\partial N}}{4\pi q} \left(\frac{\Gamma_P^2 + \omega^2}{\left(\omega^2 - \Omega_R^2 - \Gamma_R^2\right)^2 + 4\omega^2\Gamma_R^2} \right)^{1/2}. \tag{2.35}$$

The derivation for this equation can be found in Appendix D. Similarly to the intensity response, there is a phase shift of the chirp. This causes a delay between the intensity modulation and the frequency modulation. This delay is also frequency-dependent [13]:

$$\theta_f(\omega) = \arctan\left(\frac{\omega}{\Gamma_P}\right) + \arctan\left(\frac{2\omega\Gamma_R}{\omega^2 - \Omega_R^2 - \Gamma_R^2}\right). \tag{2.36}$$

2.4 Photodiode

At the end of the optical link, the photodiode converts the optical signal into electrical current. This Section contains a brief overview of photodiode operation.

2.4.1 Photodiode Concepts

Similarly to a semiconductor laser, a photodiode uses a PN junction. Unlike a laser, the photodiode is set up to absorb photons. When a photodiode is reverse biased, a large depletion region is created. This prevents current from passing through the device. When a photon is absorbed in this region, a carrier (electron hole pair) is created. The action of the applied voltage will cause the electron and hole to move to the N and P sections respectively, thus completing the circuit and creating a current. Below saturation the generated current is directly proportional to the incident light power; the ratio is denominated responsivity [10].

The bandwidth of a photodiode is governed by the carrier travel time. If a carrier is generated in the depletion region, its movement is governed by the drift speed, as opposed to the undepleted region, where current carrier movement is governed by the much slower diffusion speed. This implies that a large depleted region will

---

α_c – linewidth enhancement factor, or α-factor
I_p – peak value of the modulation current
$\frac{\partial G}{\partial N}$ – gain derivative relative to the carrier population
q – magnitude of the electron charge
Γ_P – small signal decay rate of the fluctuations in the photon population
Ω_R – angular frequency of the relaxation oscillation peak
Γ_R – relaxation oscillation decay rate

increase bandwidth as the probability of a photon being absorbed in this region is higher. This is achieved by large reverse voltages and/or by having an intrinsic (undoped or lightly doped) region between the P and N regions, thus creating a PIN photodiode. In this type of diodes drift speed dominates and the contribution of diffusion is minimized. One added advantage of a large depleted region is the large separation of the conductive P and N regions. As these act as a capacitor, larger separation leads to increased bandwidth due to a reduction in capacitance. The upper limit of the depletion region size is dictated by carrier transit times.

2.4.2 Thermal and Shot Noise

The two main types of noise in a photodiode are thermal and shot noise [10].

Thermal noise is caused by the motion of charge carriers in a conductor. This motion causes current fluctuations. Thermal noise dominates (compared to shot noise) in typical operating conditions, becoming more noticeable for lower **R**eceived **O**ptical **P**ower (ROP). Its magnitude depends mostly on the temperature and resistance in the circuit. This implies that the main contributor for thermal noise in a receiver is not the photodiode but the amplification sections after it.

Shot noise occurs due to the discrete nature of electrons (for electrical circuits). In optical circuits it arises from the similarly discrete nature of photons. This noise is most noticeable for high ROP and conversely high photodiode current where thermal noise is not dominant. In this situation, all the photon/electron contributions to the total power/current add up becoming noticeable. Increases in ROP do not lead to a decrease in shot noise due to the added contribution of more photons/electrons.

Chapter 3

Transmission Impairments Characterization

In this Chapter, transmission impairments of access systems are characterized.

Initially, an overview of fibre impairments is presented. Special attention is given to the impact of CD in IMDD systems where power fading can be a limiting factor for large bandwidth signals.

Later, results of the interaction between CD and laser chirp are analysed. These cause FM-AM signal conversion [60] which, after detection, can lead to SSII. This analysis is performed analytically by deriving a formulation capable of predicting SSII-induced SNR degradation. For this purpose, a simplified laser model is also developed.

3.1 Fibre Transmission

The dominant fibre type in current access networks is the **S**ingle-**M**ode **F**ibre (SMF). Alternatives to this fibre are **M**ulti-**M**ode **F**ibres (MMFs) or **M**ulti-**C**ore **F**ibres (MCFs). One limiting factor of MMF is modal dispersion which is caused by different modes propagating at different speeds resulting in pulse spreading [67]. This effect imposes a length-dependent bandwidth penalty; the bandwidth-times length product, known as modal bandwidth [67], is used as a figure of merit for MMFs [68]. 40Gbit/s transmission over 550m using MMF has been shown [69].

While an SMF can transmit parallel channels in its two polarizations, MMFs and MCFs can use spatial modes to transmit parallel channels in a process known as **S**pace

Division **M**ultiple **A**ccess (SDMA) [70]. Due to bending and fibre imperfections, modes couple during propagation leading to crosstalk [67], [70]. This crosstalk can be eliminated using **M**ultiple-**I**nput **M**ultiple-**O**utput (MIMO) signal processing. This, however, increases system cost [71]. Complexity, and consequently cost, of signal processing is dictated by the number of modes. It is common to use fibres that support a limited number of modes, known as **F**ew **M**ode **F**ibres (FMFs) [70].

Due to this work's focus on cost-effective access systems that require longer spans than what MMFs can provide, only SMF-based transmission is explored, more specifically **S**tandard **S**ingle-**M**ode **F**ibre (SSMF).

3.1.1 Fibre Loss

PON systems are constrained by high splitting ratios, which reduce optical power at the receiver, therefore making thermal noise a significant impairment. This is further compounded by fibre attenuation, usually represented by the fibre loss parameter in units of dB/km [10]:

$$\alpha(\text{dB/km}) = -\frac{10}{L}\log_{10}\left(\frac{P_{out}}{P_{in}}\right) \tag{3.1}$$

Fibre losses are wavelength-dependent, as seen in Figure 1.2. For bands used in PON typical losses are: 0.2 dB/km in the C-band and 0.35 dB/km in the O-band.

3.1.2 Chromatic Dispersion in Single-Mode Fibres

Chromatic **D**ispersion (CD), also known as intramodal dispersion, causes different wavelengths (colours) to propagate at different velocities. It arises from a combination of material (D_M) and waveguide (D_W) dispersion [10]. The former is caused by the frequency dependence of the refractive index (n). The latter is due to waveguide characteristics such as core radius and index difference between core and cladding [10].

Ignoring loss, the field of a travelling monochromatic wave of frequency ω_c with unitary amplitude, propagating along a fibre, at a given position (z) and time

$\alpha(dB/km)$ – fibre loss parameter
L – fibre length in km
P_{out} – output power at the fibre end
P_{in} – input power coupled at the fibre input

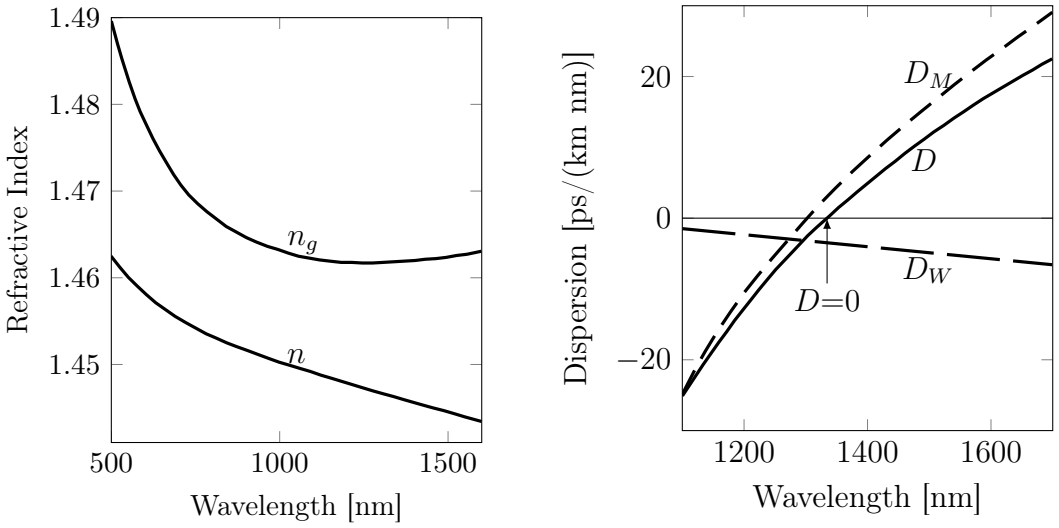

Figure 3.1: Left: variation of refractive index (n) and group index (n_g) with wavelength for fused silica [10]. Right: total dispersion (D) with material (D_M) and waveguide (D_W) contributions for an SSMF. Waveguide contribution shifts zero dispersion to a longer wavelength [10].

instant (t) is given by:

$$E(z,t) = \Re\left\{e^{j(\omega_c t - \beta z)}\right\}. \tag{3.2}$$

The phase of the wave at any given instant and position is given by $\varphi{=}\omega_c t{-}\beta z$. The frequency-dependent propagation constant$\left(\beta{=}\frac{\omega_c}{c}\bar{n}\right)$ depends on the, also frequency-dependent, refractive index $\bar{n}$ (including waveguide contribution). An observer travelling with the wave and experiencing a constant phase will have a velocity equal to the phase velocity of the wave:

$$v_\varphi = \frac{\partial z}{\partial t} = \frac{\omega_c}{\beta} = \frac{\omega_c}{\frac{\omega_c}{c}\bar{n}} = \frac{c}{\bar{n}}. \tag{3.3}$$

For a modulated wave, the envelope propagates at a different speed. An observer travelling with the envelope and experiencing a constant phase will have a velocity equal to the group velocity (v_g), which is given by the angular frequency derivative

ω_c – optical carrier angular frequency
β – propagation constant
v_φ – phase velocity
$\bar{n}$ – fibre effective refractive index
c – speed of light in vacuum

with respect to β:

$$v_g = \frac{\partial \omega_c}{\partial \beta} = \frac{\partial \omega_c}{\frac{\partial(\omega_c \bar{n})}{c}} = \frac{c}{\frac{\partial(\omega_c \bar{n})}{\partial \omega_c}} = \frac{c}{\bar{n}_g}. \tag{3.4}$$

The inverse of the group velocity is the group delay per unit length, given by:

$$\tau_g = \frac{1}{v_g} = \frac{\bar{n}_g}{c} = \frac{\partial \beta}{\partial \omega_c}. \tag{3.5}$$

The difference in propagation time per unit length and angular frequency is known as **G**roup-**V**elocity **D**ispersion (GVD). It is given by the derivative of the group delay (the inverse group velocity) relative to frequency:

$$GVD = \frac{\partial \left(\frac{1}{v_g}\right)}{\partial \omega_c} = \frac{\partial \tau_g}{\partial \omega_c} = \frac{\partial \left(\frac{\partial \beta}{\partial \omega_c}\right)}{\partial \omega_c} = \frac{\partial^2 \beta}{\partial \omega_c^2}. \tag{3.6}$$

GVD can also be seen as $\partial(\bar{n}_g/c)/\partial\omega_c$, where the zero slope of $\bar{n}_g$ represents zero dispersion. Dispersion in pure silica is known as material dispersion (D_M) which is zero at λ=1276nm, as seen in Figure 3.1(left). As previously stated, D_W contributes along with D_M to total dispersion (D). This causes a shift in zero dispersion for SSMFs to λ=1310nm, as seen in Figure 3.1(right).

It is also common to define dispersion (GVD coefficient) in terms of wavelength. Noting that ω_c=$2\pi c/\lambda$ and $d\omega_c/d\lambda$=$-2\pi c/\lambda^2$:

$$D_\lambda = \frac{d\left(\frac{d\beta}{d\omega_c}\right)}{d\lambda} = \frac{d\omega_c}{d\lambda}\frac{d\left(\frac{d\beta}{d\omega_c}\right)}{d\omega_c} = -\frac{2\pi c}{\lambda^2}\frac{\partial^2 \beta}{\partial \omega_c^2}. \tag{3.7}$$

Finally, the variation of GVD with frequency is known as the dispersion slope and is given by:

$$\frac{\partial \left(\frac{\partial \tau_g}{\partial \omega_c}\right)}{\partial \omega_c} = \frac{\partial \left(\frac{\partial^2 \beta}{\partial \omega_c^2}\right)}{\partial \omega_c} = \frac{\partial^3 \beta}{\partial \omega_c^3}. \tag{3.8}$$

Due to the relatively small bandwidth of signals used in access systems, dispersion slope and higher order dispersion will not be considered.

ω_c – optical carrier angular frequency
β – propagation constant
v_g – group velocity
c – speed of light in vacuum
$\bar{n}$ – fibre effective refractive index
$\bar{n}_g$ – fibre group index
ω_g – group angular frequency
β_g – group propagation constant
λ – wavelength

A modulated signal is composed of several frequency components and is therefore not monochromatic. Assuming the difference between a given frequency component (ω_s) and the optical carrier (ω_c) to be $|\omega_s - \omega_c| \ll \omega_c$, the signal can be considered quasi-monochromatic and the propagation constant (β) can be expanded in a Taylor series around the carrier frequency:

$$\beta = \beta_0 + \frac{\partial\beta}{\partial\omega_s}(\omega_s - \omega_c) + \frac{1}{2}\frac{\partial^2\beta}{\partial\omega_s^2}(\omega_s - \omega_c)^2 + \frac{1}{6}\frac{\partial^3\beta}{\partial\omega_s^3}(\omega_s - \omega_c)^3 + \cdots . \tag{3.9}$$

Using a simplified notation, the expansion of Eq. (3.9) can be rewritten as:

$$\beta = \beta_0 + \beta_1(\omega_s - \omega_c) + \frac{\beta_2}{2}(\omega_s - \omega_c)^2 + \frac{\beta_3}{6}(\omega_s - \omega_c)^3 + \cdots , \tag{3.10}$$

were β_0 represents a common phase shift and β_1 is the inverse of the group velocity representing a time delay.

We can now introduce the dispersion operator representing the accumulated GVD after fibre length L, assuming that $\omega = \omega_s - \omega_c$ [72], [73]:

$$d(\omega) = \frac{\beta_2}{2}\omega^2 L. \tag{3.11}$$

The dispersion operator affects the phase of each spectral component of the optical field with CD:

$$E_{out}(t) = E_{in}(t)e^{-jd(\omega)}. \tag{3.12}$$

3.1.3 Other Fibre Transmission Effects

Brillouin and Raman scattering cause incident photons to be converted into lower energy photons and phonons, respectively. The associated loss is negligible at low power levels [10]. Both nonlinear scattering phenomena become stimulated for powers above a given threshold which is modulation format-dependent. The threshold for **S**timulated **B**rillouin **S**cattering (SBS) is larger than 10mW for optical carrier bandwidths exceeding 200MHz [10]. **S**timulated **R**aman **S**cattering (SRS) has a threshold of 570mW near 1550nm [10]. Due to access systems' low power none of these effects is considered.

The refractive index of silica behaves nonlinearly at high optical powers in what is known as the Kerr effect. The nonlinear component of the refractive index has a small numerical value but its effects are cumulative with fibre length [10]. One of the effects resulting from the modulation-dependent change in refractive index is

Self-**P**hase **M**odulation (SPM) which, as the name indicates, alters the phase of the optical signal. The maximum SPM-induced phase shift is given by [74]:

$$\phi_{max} = \gamma P_0 L_{eff}. \tag{3.13}$$

The effects of SPM are negligible whenever ϕ_{max}<1 [74]. For typical values of $\alpha(dB/km)$=0.2 and 1<γ<5W^{-1}/km [10], SPM is only relevant at peak power levels above 25 mW [74]. Due to low power levels used in access systems SPM is not considered in this work.

An effect similar to SPM but occurring between co-propagating optical channels (in different wavelengths) is Cross-**P**hase **M**odulation (XPM). As the name indicates, each channel is affected by phase modulation arising from power variations of other optical channels. In a WDM system with M channels each with P_{ch} power, the maximum XPM-induced phase shift is given by [74]:

$$\phi_{max} = \gamma L_{eff}(2M-1)P_{ch}. \tag{3.14}$$

Again, assuming that XPM effects are negligible for ϕ_{max}<1 [74] and for typical values of $\alpha(dB/km)$ and γ, P_{ch} should be below 10 mW for a five channel WDM system. Due to low power levels used in access systems and the fact that the XPM-induced penalty is reduced for large optical channel spacing [74], XPM is not considered in this work.

The remaining Kerr effect, **F**our-**W**ave **M**ixing (FWM), causes an optical field to be generated whenever three fields co-propagate in the fibre. The frequency of the resulting field is related to other fields by the expression [10]:

$$\omega_{ijk} = \omega_i \pm \omega_j \pm \omega_k, i \neq k, j \neq k. \tag{3.15}$$

Most combinations do not form due to a phase matching requirement [75]. Near phase matching occurs where two photons from ω_i and ω_j are lost to generate two photons at ω_{ijk} and ω_k leading to the expression [75]:

$$\omega_{ijk} + \omega_k = \omega_i + \omega_j, i \neq k, j \neq k, \tag{3.16}$$

which can be rewritten as [10]:

$$\omega_{ijk} = \omega_i + \omega_j - \omega_k, i \neq k, j \neq k. \tag{3.17}$$

γ – fibre nonlinear coefficient

L_{eff} – effective interaction length $L_{eff} \approx \left[1 - \exp\left(-\left(\frac{\alpha(dB/km)}{4343}\right)L\right)\right] / \left(\frac{\alpha(dB/km)}{4343}\right)$

This combination is especially important for WDM systems operating close to the zero dispersion wavelength. The phase matching condition arises from the requirement of momentum conservation and is of the form [10]:

$$\Delta = \beta(\omega_k) + \beta(\omega_{ijk}) - \beta(\omega_i) - \beta(\omega_j), i \neq k, j \neq k, \tag{3.18}$$

with maximum phase matching at Δ=0. The conditions $i \neq k$ and $j \neq k$ do not prevent $\omega_i = \omega_j$ from occurring, which is the degenerate case. In this case, assuming two consecutive channels (1 and 2) they can be assigned as: $i=j=1$ and $k=2$ leading to:

$$\omega_{112} = \omega_1 + \omega_1 - \omega_2 = \omega_1 - (\omega_2 - \omega_1) = \omega_1 - \Omega. \tag{3.19}$$

where Ω is the channel spacing, implying that:

$$\omega_2 = \omega_1 + \Omega. \tag{3.20}$$

Replacing Eqs. (3.19) and (3.20) into Eq. (3.18) leads to:

$$\Delta = \beta(\omega_1 + \Omega) + \beta(\omega_1 - \Omega) - 2\beta(\omega_1). \tag{3.21}$$

Expanding Eq. (3.21) using Eq. (3.10) will lead the components β_0 and β_1 to be cancelled and the phase mismatch to be [10]:

$$\Delta = \beta_2 \Omega^2. \tag{3.22}$$

For $|\beta_2| > 5ps^2/km$ and $\Omega > 50Ghz$ the power transferred to the generated wave is close to zero [74]. FWM is not considered in this work.

Polarization **M**ode **D**ispersion (PMD) causes different delays between the two polarization components of an SMF. The **R**oot **M**ean **S**quare (RMS) value of the delay between components (σ_T) is given by [10]:

$$\sigma_T \approx D_p \sqrt{L}. \tag{3.23}$$

Assuming that a modern fibre has a worst case D_p=0.1ps/$\sqrt{\text{km}}$ [10] and noting that a typical PON system has a maximum reach of 20km (Table 1.1), the RMS of the delay between components is $\sigma_T \approx$0.45ps. This delay is negligible for the considered systems, therefore PMD is not considered.

Δ – phase matching condition
β – propagation constant
Ω – channel spacing
D_p – PMD parameter

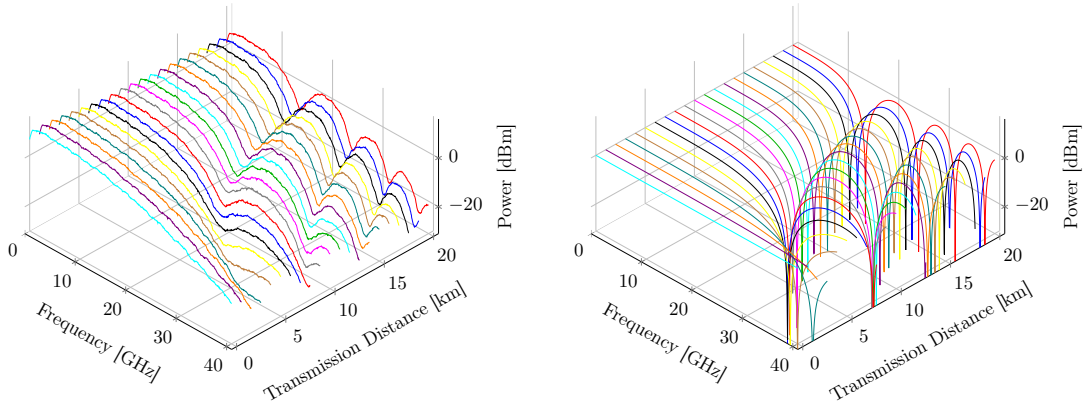

Figure 3.2: Left: simulated OFDM spectra showing power fading evolution with transmission distance [76]. Right: calculated power fading for ideal transmission with λ=1552.05×10^{-9} m and D_λ=15.04×10^{-6} s m^{-2}.

3.2 Power Fading

Intensity modulation of an optical carrier generates a **D**ouble **S**ide**b**and (DSB) signal. This signal is composed of the optical carrier and two side-bands: LSB and USB. In direct detection, each side-band beats with the optical carrier to create two beat components that constructively interfere to generate the detected signal. In the presence of CD, each side-band experiences a different phase shift relative to the optical carrier. Consequently, the beat components will have opposite phase shifts. These can lead to destructive interference [52] resulting in power nulls at specific frequencies. This effect is known as power fading and its effects for a simulated OFDM signal can be seen in Figure 3.2(left).

Power fading affects especially electrical baseband and single carrier systems. OFDM can cope with power fading in **P**oint to **P**oint (P2P) systems by disabling affected subcarriers and shifting power to the remaining ones. In OFDM-based PON systems, subcarrier assignment to users can take power fading into account by only assigning subcarriers that are not affected by power fading at each user's distance from the OLT.

By increasing system cost, power fading can be practically eliminated. This can be achieved by transmitting the optical carrier and only a single side-band using a modulator capable of intensity and phase control, more specifically a dual drive MZM [55], [77] or an IQ modulator [58], [78].

The profile of the detected signal for a given accumulated dispersion can be

calculated. Considering an ideal chirpless laser with unitary power, the intensity modulated (IM) optical field at its output is:

$$E_{in}(t) = \sqrt{1 + S_{mod}(t)}\ e^{j\omega_c t} = IM_{in}(t)\ e^{j\omega_c t}, \tag{3.24}$$

assuming modulation by two cosines of frequencies ω_a and ω_b with unitary amplitude and modulation index m:

$$S_{mod}(t) = m(\cos(\omega_a t) + \cos(\omega_b t)). \tag{3.25}$$

For $m \ll 1$, the square root of Eq. (3.24) can be approximated using Taylor series expansion to a first degree polynomial [72]. For increased accuracy, the Taylor expansion is instead performed up to a second degree polynomial [15]:

$$\sqrt{1 + S_{mod}(t)} = 1 + \frac{m}{2}\cos(\omega_a t) + \frac{m}{2}\cos(\omega_b t) - \frac{m^2}{8}\left(\cos(\omega_a t) + \cos(\omega_b t)\right)^2. \tag{3.26}$$

After expanding the squared binomial, the DC component is simplified by the variable replacement $A = 1 - m^2/8$:

$$\begin{aligned}\sqrt{1 + S_{mod}(t)} = A &+ \frac{m}{2}\cos(\omega_a t) + \frac{m}{2}\cos(\omega_b t) \\ &- \frac{m^2}{16}\cos(2\omega_a t) - \frac{m^2}{16}\cos(2\omega_b t) \\ &- \frac{m^2}{8}\cos((\omega_b - \omega_a)t) - \frac{m^2}{8}\cos((\omega_b + \omega_a)t).\end{aligned} \tag{3.27}$$

After expansion of the square root, the optical field is:

$$\begin{aligned}E_{in}(t) = e^{j\omega_c t}\Big(A &+ \frac{m}{2}\cos(\omega_a t) + \frac{m}{2}\cos(\omega_b t) \\ &- \frac{m^2}{16}\cos(2\omega_a t) - \frac{m^2}{16}\cos(2\omega_b t) \\ &- \frac{m^2}{8}\cos((\omega_b - \omega_a)t) - \frac{m^2}{8}\cos((\omega_b + \omega_a)t)\Big).\end{aligned} \tag{3.28}$$

At the fibre output, with CD applied using the dispersion operator $d(\omega)$ of Eq. (3.11),

the optical field is:

$$\begin{aligned}
E_{out}(t) = e^{j\omega_c t}\Big(A \\
&+\frac{m}{2}\cos(d(\omega_a))\cos(\omega_a t) + \frac{m}{2}\cos(d(\omega_b))\cos(\omega_b t) \\
&-\frac{m^2}{16}\cos(d(2\omega_a))\cos(2\omega_a t) - \frac{m^2}{16}\cos(d(2\omega_b))\cos(2\omega_b t) \\
&-\frac{m^2}{8}\cos(d(\omega_b-\omega_a))\cos((\omega_b-\omega_a)t) - \frac{m^2}{8}\cos(d(\omega_b+\omega_a))\cos((\omega_b+\omega_a)t) \\
&-j\frac{m}{2}\sin(d(\omega_a))\cos(\omega_a t) - j\frac{m}{2}\sin(d(\omega_b))\cos(\omega_b t) \\
&+j\frac{m^2}{16}\sin(d(2\omega_a))\cos(2\omega_a t) + j\frac{m^2}{16}\sin(d(2\omega_b))\cos(2\omega_b t) \\
&+j\frac{m^2}{8}\sin(d(\omega_b-\omega_a))\cos((\omega_b-\omega_a)t) + j\frac{m^2}{8}\sin(d(\omega_b+\omega_a))\cos((\omega_b+\omega_a)t)\Big).
\end{aligned} \tag{3.29}$$

After detection ($|E_{out}(t)|^2$=$I_{Det.}(t)$), only the larger components are considered, namely the real components beating with the carrier, the main components beating with themselves (real and imaginary components squared) and the main components beating with each other (real and imaginary). The terms landing in DC are also ignored:

$$\begin{aligned}
&I_{Det.}(t) = \\
&+Am\cos(d(\omega_a))\cos(\omega_a t) + Am\cos(d(\omega_b))\cos(\omega_b t) \\
&-A\frac{m^2}{8}\cos(d(2\omega_a))\cos(2\omega_a t) - A\frac{m^2}{8}\cos(d(2\omega_b))\cos(2\omega_b t) \\
&-A\frac{m^2}{4}\cos(d(\omega_b-\omega_a))\cos((\omega_b-\omega_a)t) - A\frac{m^2}{4}\cos(d(\omega_b+\omega_a))\cos((\omega_b+\omega_a)t) \\
&+\frac{m^2}{8}\cos(2\omega_a t) + \frac{m^2}{8}\cos(2\omega_b t) \\
&+\frac{m^2}{4}\cos(d(\omega_a))\cos(d(\omega_b))\cos((\omega_b-\omega_a)t) + \frac{m^2}{4}\cos(d(\omega_a))\cos(d(\omega_b))\cos((\omega_b+\omega_a)t) \\
&+\frac{m^2}{4}\sin(d(\omega_a))\sin(d(\omega_b))\cos((\omega_b-\omega_a)t) + \frac{m^2}{4}\sin(d(\omega_a))\sin(d(\omega_b))\cos((\omega_b+\omega_a)t).
\end{aligned} \tag{3.30}$$

For optical **B**ack-**t**o-**B**ack (BTB) or transmission without CD ($d(\omega)$=0) the modulator cosines are recovered, whereas all other components have a small residual amplitude due to the limited Taylor series expansion. In the presence of CD, the amplitudes of the detected modulator cosines vary according to transmission distance and frequency.

Cancellation occurs for:

$$d(\omega) = N\frac{\pi}{2},\ N = 1, 3, 5, \cdots . \tag{3.31}$$

Substituting Eq. (3.7) in Eq. (3.11) results in the expression:

$$d(\omega) = -\frac{1}{2}\frac{\lambda^2}{2\pi c}\omega^2 D_\lambda L. \tag{3.32}$$

Finally, combining Eq. (3.31) and Eq. (3.32) results in an expression indicating at which fibre lengths cancellation occurs [52]:

$$L = \frac{N2\pi^2 c}{\lambda^2\omega^2 D_\lambda},\ N = 1, 3, 5, \cdots . \tag{3.33}$$

The calculated power fading profile can be seen in Figure 3.2(right), showing a good agreement with the simulated power fading profile of Figure 3.2(left) in terms of the cancellation frequencies for the considered transmission distances.

3.3 Subcarrier-to-Subcarrier Intermixing Interference

An optical signal transmitted using a DML has a frequency modulation component denominated as chirp. The FM component of the signal beats with the IM component to create intermodulation products. These are not present after detection in optical BTB or when the channel has very low dispersion. Such are the cases of O-band transmission or whenever dispersion compensating techniques are implemented. For C-band transmission, the relative delay experienced by the different intermodulation products prevents their cancellation after detection [73]. They beat with the optical carrier and with each other to create what is known in multicarrier systems as **S**ubcarrier-to-**S**ubcarrier **I**ntermixing **I**nterference (SSII) [14]. The appearance of intermodulation products after detection is also known as FM-AM conversion [60]. SSII becomes of importance whenever large modulation indexes (m) are used to maximize the system power budget, leading to large laser chirp.

Implementing a similar approach to the derivation on Page 41 and subsequent, SSII can be explored. For simplicity of notation, laser chirp can be represented as **P**hase **M**odulation (PM) instead of FM. For this case, the IM optical field is taken from Eq. (3.24) and phase modulation is added:

$$E_{in}(t) = \sqrt{1 + S_{mod}(t)}\ e^{j\omega_c t + jp\phi(t)} = IM_{in}(t)\ PM_{in}(t)\ e^{j\omega_c t}, \tag{3.34}$$

where $\phi(t)$=$S_{mod}(t)$ and p is the parameter that controls the ratio of phase modulation to modulator signal amplitude. $S_{mod}(t)$ is assumed to represent two cosines, as seen in Eq. (3.25). The expansion of the square root (IM) is the same as of Eq. (3.27). The PM part is expanded using the Jacobi-Anger identity [15], [79]–[81]. For $p \ll 1$, the expansion can be limited to the same frequency range of the IM Taylor expansion. For a more compact notation, Bessel coefficients are represented in a simplified manner (J_x=$J_x(p)$):

$$PM_{in}(t) = (J_0 + j2J_1\cos(\omega_a t) - 2J_2\cos(2\omega_a t))(J_0 + j2J_1\cos(\omega_b t) - 2J_2\cos(2\omega_b t)). \tag{3.35}$$

The beating of the PM terms is also limited to the same frequency range of the IM expansion:

$$\begin{aligned} PM_{in}(t) =& J_0^2 + jJ_0 2J_1\cos(\omega_a t) + jJ_0 2J_1\cos(\omega_b t) \\ & -2J_0J_2\cos(2\omega_a t) - 2J_0J_2\cos(2\omega_b t) \\ & -2J_1^2\cos((\omega_b-\omega_a)t) - 2J_1^2\cos((\omega_b+\omega_a)t). \end{aligned} \tag{3.36}$$

The optical signal at the fibre input is given by the beating between IM (Eq. (3.27)) and PM (Eq. (3.36)), creating second order intermodulation products.

In this beating only the largest components are kept, namely the ones having the following combination of Bessel functions: J_0^2, J_0J_1, J_0J_2 and J_1^2. The DC components beat together to make AJ_0^2 which represents the optical carrier power (C). The IM components multiply with J_0^2 to create an intensity modulated copy of S_{mod} (S_{IM}) at ω_a and ω_b, as well as intermodulation products (IP) at other frequencies:

$$\begin{aligned} IM_{in}(t)J_0^2 =& J_0^2\frac{m}{2}\cos(\omega_a t) + J_0^2\frac{m}{2}\cos(\omega_b t) && (S_{IMin}) \\ & -J_0^2\frac{m^2}{16}\cos(2\omega_a t) - J_0^2\frac{m^2}{16}\cos(2\omega_b t) && (IP_{in}) \\ & -J_0^2\frac{m^2}{8}\cos((\omega_b-\omega_a)t) - J_0^2\frac{m^2}{8}\cos((\omega_b+\omega_a)t). && (IP_{in}) \end{aligned} \tag{3.37}$$

Similarly, PM components beat with A to create a frequency modulated copy of S_{mod} (S_{FM}) at ω_a and ω_b, as well as intermodulation products (IP) at other frequencies:

$$\begin{aligned} PM_{in}(t)A =& j2AJ_0J_1\cos(\omega_a t) + j2AJ_0J_1\cos(\omega_b t) && (S_{PMin}) \\ & -2AJ_0J_2\cos(2\omega_a t) - 2AJ_0J_2\cos(2\omega_b t) && (IP_{in}) \\ & -2AJ_1^2\cos((\omega_b-\omega_a)t) - 2AJ_1^2\cos((\omega_b+\omega_a)t). && (IP_{in}) \end{aligned} \tag{3.38}$$

Finally, only the beating IM and PM terms at modulator frequencies ω_a and ω_b are considered; these are also (IP). All other beating terms are discarded; any extra DC component is also discarded. The result of the beating is:

$$\begin{aligned} IM_{in}(t)PM_{in}(t)[\omega_a,\omega_b] =& jJ_0J_1\frac{m}{2}\cos(2\omega_a t)+jJ_0J_1\frac{m}{2}\cos(2\omega_b t) && (IP_{in})\\ &+jJ_0J_1\frac{m}{2}\cos((\omega_b-\omega_a)t)+jJ_0J_1\frac{m}{2}\cos((\omega_b-\omega_a)t) && (IP_{in})\\ &+jJ_0J_1\frac{m}{2}\cos((\omega_b+\omega_a)t)+jJ_0J_1\frac{m}{2}\cos((\omega_b+\omega_a)t). && (IP_{in}) \end{aligned} \tag{3.39}$$

Before presenting the final expression for the optical field the following variable replacements are used:

$$X_0 = AJ_0^2, \tag{3.40}$$

$$X_1 = J_0^2\frac{m}{2}, \tag{3.41}$$

$$X_2 = -J_0^2\frac{m^2}{16} - 2AJ_0J_2, \tag{3.42}$$

$$X_3 = -J_0^2\frac{m^2}{8} - 2AJ_1^2, \tag{3.43}$$

$$X_4 = 2AJ_0J_1, \tag{3.44}$$

$$X_5 = J_0J_1\frac{m}{2}, \tag{3.45}$$

$$X_6 = J_0J_1m. \tag{3.46}$$

The expression for the optical field at the fibre input is:

$$\begin{aligned} E_{in}(t) = e^{j\omega_c t}(&X_0 && (C_{in})\\ &+X_1\cos(\omega_a t) + X_1\cos(\omega_b t) && (S_{IMin})\\ &+jX_4\cos(\omega_a t) + jX_4\cos(\omega_b t) && (S_{PMin})\\ &+(X_2+jX_5)\cos(2\omega_a t) + (X_2+jX_5)\cos(2\omega_b t) && (IP_{in})\\ &+(X_3+jX_6)\cos((\omega_b-\omega_a)t) && (IP_{in})\\ &+(X_3+jX_6)\cos((\omega_b+\omega_a)t)). && (IP_{in}) \end{aligned} \tag{3.47}$$

At the fibre output, with CD applied using the dispersion operator $d(\omega)$ of Eq. (3.11),

the optical field is:

$$
\begin{aligned}
&E_{out}(t) = e^{j\omega_c t}(X_0 && (C)\\
&+(X_1\cos(d(\omega_a)) + X_4\sin(d(\omega_a)))\cos(\omega_a t) && (S_{IMout} + S_{PMout})\\
&+(X_1\cos(d(\omega_b)) + X_4\sin(d(\omega_b)))\cos(\omega_b t) && (S_{IMout} + S_{PMout})\\
&+(X_2\cos(d(2\omega_a)) + X_5\sin(d(2\omega_a)))\cos(2\omega_a t) && (IP_{out})\\
&+(X_2\cos(d(2\omega_b)) + X_5\sin(d(2\omega_b)))\cos(2\omega_b t) && (IP_{out})\\
&+(X_3\cos(d(\omega_b-\omega_a)) + X_6\sin(d(\omega_b-\omega_a)))\cos((\omega_b-\omega_a)t) && (IP_{out})\\
&+(X_3\cos(d(\omega_b+\omega_a)) + X_6\sin(d(\omega_b+\omega_a)))\cos((\omega_b+\omega_a)t) && (IP_{out})\\
&+j(-X_1\sin(d(\omega_a)) + X_4\cos(d(\omega_a)))\cos(\omega_a t) && (S_{IMout} + S_{PMout})\\
&+j(-X_1\sin(d(\omega_b)) + X_4\cos(d(\omega_b)))\cos(\omega_b t) && (S_{IMout} + S_{PMout})\\
&+j(-X_2\sin(d(2\omega_a)) + X_5\cos(d(2\omega_a)))\cos(2\omega_a t) && (IP_{out})\\
&+j(-X_2\sin(d(2\omega_b)) + X_5\cos(d(2\omega_b)))\cos(2\omega_b t) && (IP_{out})\\
&+j(-X_3\sin(d(\omega_b-\omega_a)) + X_6\cos(d(\omega_b-\omega_a)))\cos((\omega_b-\omega_a)t) && (IP_{out})\\
&+j(-X_3\sin(d(\omega_b+\omega_a)) + X_6\cos(d(\omega_b+\omega_a)))\cos((\omega_b+\omega_a)t). && (IP_{out}) \qquad (3.48)
\end{aligned}
$$

After direct detection, the resulting frequency components can be divided into several groups: carrier-carrier beating (C^2), carrier-signal beating (CS), carrier-IP beating (CIP), signal-signal beating (different frequencies) ($2S$), signal-signal beating (same frequency) (S^2), signal-IP (SIP) beating, IP-IP beating (different frequencies) ($2IP$) and IP-IP beating(same frequency) (IP^2). The S^2 and IP^2 products are dominant if the carrier is not strong; for a strong optical carrier the carrier-signal beating and carrier-noise beating become the dominant components [82]. Access systems typical transmission distances do not require multiple amplification stages. As such, optical noise is not a limiting factor. This relaxes the requirement of a strong carrier.

Detected current can be written as follows:

$$
\begin{aligned}
I_{Det.} =& 2\Re(CS_{IM}) + 2\Re(CS_{PM}) && (CS) && \{I_{Signal}\}\\
&+2\Re(S_{IM})\Re(S_{IM}) + 2\Im(S_{IM})\Im(S_{IM}) && (2S) && \{I_{SSII}\}\\
&+2\Re(S_{PM})\Re(S_{PM}) + 2\Im(S_{PM})\Im(S_{PM}) && (2S) && \{I_{SSII}\}\\
&+2\Re(S_{IM})\Re(S_{PM}) + 2\Im(S_{IM})\Im(S_{PM}) && (2S) && \{I_{SSII}\}\\
&+|S_{IM}|^2 + |S_{PM}|^2 && (S^2) && \{I_{SSII}\}
\end{aligned}
$$

$$
\begin{aligned}
&+2\Re(CIP) && (CIP) && \{I_{SSII}\}\\
&+|C|^2 && (C^2) && \{discarded\}\\
&+2\Re(S_{IM})\Re(IP)+2\Im(S_{IM})\Im(IP) && (SIP) && \{discarded\}\\
&+2\Re(S_{PM})\Re(IP)+2\Im(S_{PM})\Im(IP) && (SIP) && \{discarded\}\\
&+2\Re(IP)\Re(IP)+2\Im(IP)\Im(IP) && (2IP) && \{discarded\}\\
&+|IP|^2. && (IP^2) && \{discarded\}
\end{aligned}
\tag{3.49}
$$

where $\Re$ and $\Im$ are the real and imaginary parts of the component. The DC component ($|C|^2$) is discarded as it is of no interest. All IP-IP beating and Signal-IP beating are also not considered as these are the smallest components.

The kept components in Eq. (3.49) can be divided into four groups:

$$I_{Det.}(t) = I_{Signal}(t) + I_{SSII}\left[2S\right](t) + I_{SSII}\left[S^2\right](t) + I_{SSII}\left[CIP\right](t). \tag{3.50}$$

Each of the kept components after detection is now described. Carrier-signal beating (CS) is:

$$
\begin{aligned}
I_{Signal}(t) =& 2X_0(X_1\cos(d(\omega_a)) + X_4\sin(d(\omega_a)))\cos(\omega_a t)\\
&+2X_0(X_1\cos(d(\omega_b)) + X_4\sin(d(\omega_b)))\cos(\omega_b t),
\end{aligned}
\tag{3.51}
$$

signal-signal beating (different frequencies):

$$
\begin{aligned}
&I_{SSII}\left[2S\right](t) =\\
&(X_1\cos(d(\omega_a)) + X_4\sin(d(\omega_a)))(X_1\cos(d(\omega_b)) + X_4\sin(d(\omega_b)))\cos((\omega_b-\omega_a)t)\\
&+(X_1\cos(d(\omega_a)) + X_4\sin(d(\omega_a)))(X_1\cos(d(\omega_b)) + X_4\sin(d(\omega_b)))\cos((\omega_b+\omega_a)t)\\
&+(-X_1\sin(d(\omega_a))+X_4\cos(d(\omega_a)))(-X_1\sin(d(\omega_b))+X_4\cos(d(\omega_b)))\cos((\omega_b-\omega_a)t)\\
&+(-X_1\sin(d(\omega_a))+X_4\cos(d(\omega_a)))(-X_1\sin(d(\omega_b))+X_4\cos(d(\omega_b)))\cos((\omega_b+\omega_a)t),
\end{aligned}
\tag{3.52}
$$

signal-signal beating (same frequency):

$$
\begin{aligned}
I_{SSII}\left[S^2\right](t) =& \frac{1}{2}(X_1\cos(d(\omega_a)) + X_4\sin(d(\omega_a)))^2\cos(2\omega_a t)\\
&+\frac{1}{2}(X_1\cos(d(\omega_b)) + X_4\sin(d(\omega_b)))^2\cos(2\omega_b t)\\
&+\frac{1}{2}(-X_1\sin(d(\omega_a)) + X_4\cos(d(\omega_a)))^2\cos(2\omega_a t)\\
&+\frac{1}{2}(-X_1\sin(d(\omega_b)) + X_4\cos(d(\omega_b)))^2\cos(2\omega_b t),
\end{aligned}
\tag{3.53}
$$

finally the carrier-IP beating:

$$\begin{aligned} I_{SSII}\left[CIP\right](t) =& 2X_0(X_2\cos(d(2\omega_a)) + X_5\sin(d(2\omega_a)))\cos(2\omega_a t) \\ &+2X_0(X_2\cos(d(2\omega_b)) + X_5\sin(d(2\omega_b)))\cos(2\omega_b t) \\ &+2X_0(X_3\cos(d(\omega_b-\omega_a)) + X_6\sin(d(\omega_b-\omega_a)))\cos((\omega_b-\omega_a)t) \\ &+2X_0(X_3\cos(d(\omega_b+\omega_a)) + X_6\sin(d(\omega_b+\omega_a)))\cos((\omega_b+\omega_a)t). \end{aligned} \tag{3.54}$$

For optical BTB or transmission without CD ($d(\omega)$=0) the detected signal is:

$$\begin{aligned} I_{Det.}(t) &= 2X_0X_1\cos(\omega_a t) + 2X_0X_1\cos(\omega_b t) \\ &+\left(2X_0X_2 + \frac{1}{2}X_1^2 + \frac{1}{2}X_4^2\right)\cos(2\omega_a t) + \left(2X_0X_2 + \frac{1}{2}X_1^2 + \frac{1}{2}X_4^2\right)\cos(2\omega_b t) \\ &+(2X_0X_3 + X_1^2 + X_4^2)\cos((\omega_b-\omega_a)t) + (2X_0X_3 + X_1^2 + X_4^2)\cos((\omega_b+\omega_a)t), \end{aligned} \tag{3.55}$$

where $2X_0X_2+\frac{1}{2}X_1^2+\frac{1}{2}X_4^2\simeq 0$ and $2X_0X_3+X_1^2+X_4^2\simeq 0$. Therefore the detected signal will be:

$$I_{Det.}(t) = 2X_0X_1\cos(\omega_a t) + 2X_0X_1\cos(\omega_b t). \tag{3.56}$$

Both modulator tones are recovered despite the phase modulation.

In this example, it is clear that SSII components have different frequencies than the transmitted tones. Nevertheless, for larger numbers of subcarriers, SSII components land on frequencies occupied by other subcarriers causing interference. For the sake of simplicity, PM was used and the number of tones was kept to a minimum. In the next Section, an analytical formulation is presented using a similar derivation for an arbitrary number of subcarriers.

3.4 Prediction of SSII-induced SNR Degradation

The independent configuration of OFDM subcarriers allows adaptation to the transmission channel towards the goal of capacity increase. In access systems, different subscribers are located at different distances from the OLT. For this reason, the same subcarrier shows different performance for different subscribers. For instance, power fading can cause a subcarrier to have poor SNR at a specific transmission

distance. Knowledge of the system performance can aid in subcarrier assignment to subscribers.

An analytical formulation for SNR prediction in OFDM-based DMDD systems is presented in this Section. It can be used for subcarrier assignment as well as to provide a starting configuration in pre-emphasis algorithms such as bit-and-power loading. In this analytical formulation, the laser frequency responses in terms of intensity (IM) and frequency (FM) are taken into account. In order to ease the task of using data from real lasers in the formulation, an easy to configure laser model is firstly developed. Appendix E details the steps required for configuration of this simplified laser model. The full derivation of the analytical formulation can be seen in Appendix F.

3.4.1 Simplified Laser Model

A laser model based on the numerical solution of rate equations is commonly used in system level simulations. One such example is the *VPIphotonics'* "LaserSM_RE". Due to its high parameter count, configuring such a laser model to emulate a commercial laser is complex, as the information provided by the manufacturer is usually limited. A simple to configure laser model to enable SNR prediction in SSII-impaired systems is required.

IM Model

In its most basic form, a DML can be represented by an intensity modulated monochromatic wave of angular frequency (ω_c) with unitary power. When modulated by a cosine with angular frequency (ω) and modulation index (m), its output field will be:

$$E(t) = \sqrt{1 + m\cos(\omega t)}e^{j\omega_c t}. \tag{3.57}$$

Laser IM response (Δ_p) of Eq. (2.32) can now be added:

$$E(t) = \sqrt{1 + \Delta_p(\omega) m\cos(\omega t)}e^{j\omega_c t}. \tag{3.58}$$

m – modulation index
ω_c – optical carrier angular frequency
Δ_p – laser intensity response

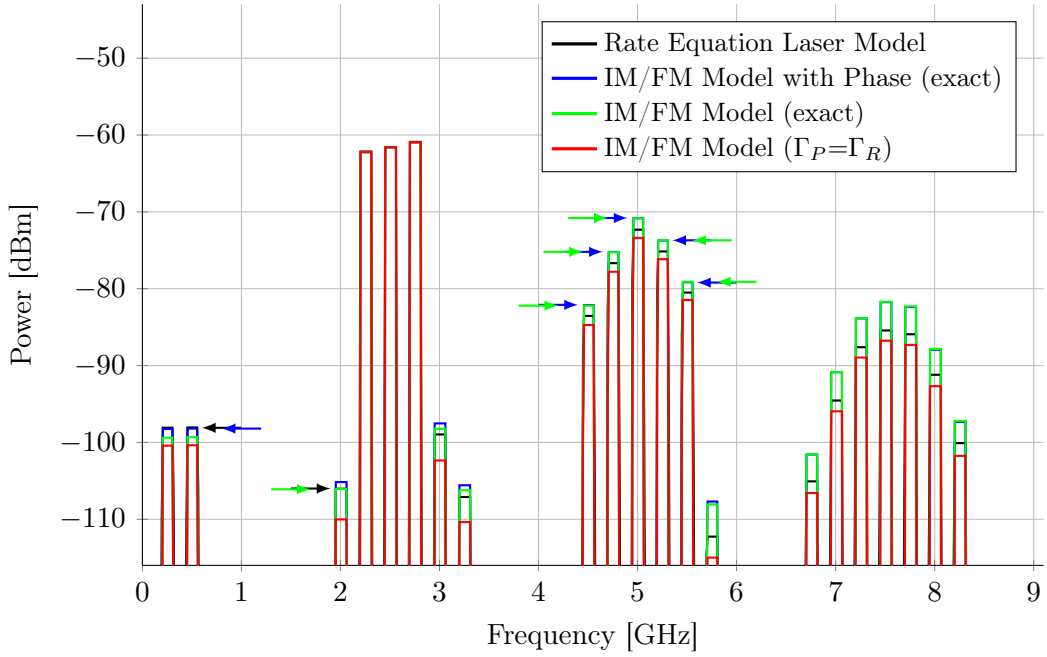

Figure 3.3: Simulation results of the transmission of three sines (2.25GHz, 2.5GHz and 2.75GHz) after 50km SSMF using different laser models. Ambiguous SSII levels due to overlap of the graph bars are clarified by arrows indicating the levels for different laser models (up to 6GHz).

IM/FM Model

The IM model can be extended by including the FM response (Δ_f) of Eq. (2.35):

$$E(t) = \sqrt{1 + \Delta_p(\omega) m \cos(\omega t)} e^{j\left(\omega_c t + 2\pi \int_0^t \Delta_f(\omega) m \cos(\omega t) dt\right)}. \tag{3.59}$$

As in the IM model, the FM response is frequency-dependent. Similarly to intensity in the IM model, also FM is modulation index (m) dependent.

This simplified laser model (IM/FM) is used in the subsequent analytical formulation derivations. The configuration of this laser model is detailed in Appendix E.

The lack of phase response simplifies derivations at the cost of accuracy. In the following Sections this simplified laser model is compared with a version including phase response and also with a rate equation model.

Δ_p – laser intensity response
m – modulation index
ω_c – optical carrier angular frequency
Δ_f – laser chirp response

IM/FM Model including Phase

The IM/FM model of Eq. (3.59) can be made more accurate through the inclusion of the frequency-dependent intensity modulation phase (θ_p) of Eq. (2.34) and the, also frequency-dependent, frequency modulation phase (θ_f) of Eq. (2.36):

$$E(t) = \sqrt{1 + \Delta_p(\omega) m \cos(\omega t + \theta_p(\omega))} e^{j\left(\omega_c t + 2\pi \int_0^t \Delta_f(\omega) m \cos(\omega t + \theta_f(\omega)) dt\right)}. \tag{3.60}$$

Comparison of Laser Models

Using simulations, the previously presented laser models, IM/FM and IM/FM including phase, are compared with the *VPIphotonics'* rate equation model "LaserSM_RE". The configuration of the laser models is the same as the one detailed in Appendix E. FM response of both IM/FM (with and without phase) laser models was configured using the exact approach detailed in Section E.2.2 (Appendix E). For completeness, one extra laser model was configured using the Γ_P simplification (Γ_P=Γ_R) of Section E.3 (Appendix E).

The laser models were fed with three sines with frequencies: 2.25GHz, 2.5GHz and 2.75GHz. The modulation index was set to m≃23%. After 50km SSMF the signals are detected with an ideal photodiode. The received spectra can be seen in Figure 3.3.

Comparing the two IM/FM models: with and without phase (Figure 3.3 red and green), shows that there is a good match for high power SSII landing around 5GHz. A larger mismatch can be seen for SSII landing close to DC. The loss of accuracy resulting from the lack of phase response in the IM/FM model is acceptable. The larger mismatch is seen for the model using the Γ_P simplification Figure 3.3(red). This is expected as the transmitted sines are in the frequency range of large chirp amplitude mismatch, as seen in Figure E.5 (Appendix E).

Δ_p – laser intensity response
m – modulation index
θ_p – laser intensity phase shift
ω_c – optical carrier angular frequency
Δ_f – laser chirp response
θ_f – laser chirp delay relative to intensity modulation

3.4.2 Analytical Formulation for SNR Prediction

In this Section, an analytical formulation for SNR prediction is derived and experimentally validated. A more in depth derivation is performed in Appendix F.

General Considerations

Signals considered for this formulation are: modulator input signal $S_{mod}(t)$, optical signal at fibre input $E_{in}(t)$, optical signal at fibre output $E_{out}(t)$ and detected current $I_{Det.}$.

The optical signal at the fibre input, assuming unitary laser power and having IM and FM components, is:

$$E_{in}(t) = \sqrt{1 + S_{mod}(t)}\ e^{j(\omega_c t + \phi(t))} = IM_{in}(t)\ FM_{in}(t)\ e^{j\omega_c t}. \tag{3.61}$$

IM

Assuming that $S_{mod}(t)$ is composed of N unmodulated cosines, each with U_k amplitude:

$$S_{mod}(t) = m \sum_{k=1}^{N} \Delta_p(\omega_k) U_k \cos(\omega_k t). \tag{3.62}$$

The square root of Eq. (3.61) can be approximated using Taylor series expansion to a first degree polynomial [72]. For increased accuracy, the Taylor expansion is performed up to a second degree polynomial [15], $m \ll 1$ is assumed. After introducing the replacement variables A, B, C and D:

$$A = 1 - \sum_{k=1}^{N} \frac{\Delta_p(\omega_k)^2 U_k^2 m^2}{16}, \tag{3.63}$$

$$B_k = \frac{\Delta_p(\omega_k) U_k m}{2}, \tag{3.64}$$

$$C_k = \frac{\Delta_p(\omega_k)^2 U_k^2 m^2}{16}, \tag{3.65}$$

$$D_{kp} = \frac{\Delta_p(\omega_k) \Delta_p(\omega_p) U_k U_p m^2}{8}, \tag{3.66}$$

ω_c – optical carrier angular frequency
$\phi(t)$ – phase modulation due to frequency modulation arising from laser chirp
$S_{mod}(t)$ – intensity modulating signal
m – modulation index
Δ_p – laser intensity response
ω_k – k subcarrier angular frequency
U_k – k subcarrier amplitude

IM_{in} will be:

$$IM_{in}(t) = A + \sum_{k=1}^{N} B_k \cos(\omega_k t) - \sum_{k=1}^{N} C_k \cos(2\omega_k t) - \sum_{k=1}^{N} \sum_{\substack{p \\ p<k}}^{N} D_{kp} \cos(\omega_k t \pm \omega_p t), \tag{3.67}$$

The largest frequency components arising from the truncated Taylor series expansion dictate the considered frequency range of the formulation. These are the signal (ω_k) and intermodulation products ($2\omega_k$ and $\omega_k \pm \omega_p$).

FM

The phase modulation representation of the chirp (FM) component is:

$$\phi(t) = 2\pi\ m \int \sum_{k=1}^{N} \Delta_f(\omega_k) U_k \cos(\omega_k t) dt, \tag{3.68}$$

which after solving the integral becomes:

$$\phi(t) = m \sum_{k=1}^{N} \frac{2\pi}{\omega_k} \Delta_f(\omega_k) U_k \sin(\omega_k t). \tag{3.69}$$

Using the following variable substitution:

$$z_k = m \frac{2\pi}{\omega_k} \Delta_f(\omega_k) U_k, \tag{3.70}$$

a compact form for phase modulation is created:

$$\phi(t) = \sum_{k=1}^{N} z_k \sin(\omega_k t). \tag{3.71}$$

The phase modulation component can now be expanded using the Jacobi-Anger identity [15], [79]–[81], the expansion is limited to the same frequency range of the IM Taylor expansion. Also here $m \ll 1$ is assumed:

$$e^{j\phi(t)} = FM_{in}(t) = \prod_{k}^{N} \Big[J_0(z_k) + j2J_1(z_k) \sin(\omega_k t) + 2J_2(z_k) \cos(2\omega_k t) \Big]. \tag{3.72}$$

The notation is simplified by replacing $J_x(z_k)$ with $J_{x(k)}$:

$$e^{j\phi(t)} = FM_{in}(t) = \prod_{k}^{N} \Big[J_{0(k)} + j2J_{1(k)} \sin(\omega_k t) + 2J_{2(k)} \cos(2\omega_k t) \Big]. \tag{3.73}$$

Multiplication leads to a high number of components, only the largest of which are kept, namely the ones having combinations of the Bessel functions with the orders: J_0^N, $J_0^{N-1}J_1$, $J_0^{N-1}J_2$ and $J_0^{N-2}J_1J_1$. Note that all the Bessel functions arise from different components that are grouped into: DC component $\Phi{=}\prod_{k=1}^{N}[J_{0(k)}]$, FM signal components at ω_k, $2\omega_k$ and $\omega_k{\pm}\omega_p$. The Φ component is considered to be DC relative to the carrier frequency, and it influences carrier power. The FM spectral components are:

$$\begin{aligned} FM_{in}(t) = \Phi &+ j2\sum_{k=1}^{N}\frac{\Phi}{J_{0(k)}}J_{1(k)}\sin(\omega_k t) \\ &+ 2\sum_{k=1}^{N}\frac{\Phi}{J_{0(k)}}J_{2(k)}\cos(2\omega_k t) \\ &\pm 2\sum_{k=1}^{N}\sum_{\substack{p \\ p<k}}^{N}\frac{\Phi}{J_{0(k)}J_{0(p)}}J_{1(k)}J_{1(p)}\cos(\omega_k t \pm \omega_p t). \end{aligned} \tag{3.74}$$

To obtain the optical signal at the fibre input, given by Eq. (3.61): Eqs. (3.67) and (3.74) are multiplied, generating many spectral components, among which are the IM and FM representations of the signal as well as intermodulation products. In order to limit their number, the same rational that was applied to Eq. (3.74) is used.

After the product, carrier power becomes $A\Phi$. The IM components multiply with Φ to create an intensity modulated copy of S_{mod} at ω_k (S_{IM}) and intermodulation products (IP) at other frequencies. Similarly, FM components multiply with A to create a frequency modulated copy of S_{mod} at ω_k (S_{FM}) and intermodulation products (IP) at other frequencies. In addition, mixing between terms B_k and $\frac{\Phi}{J_{0(k)}}J_{1(k)}$ is also considered (IP). The optical field at the laser output is written in short form as:

$$E_{in} = e^{j\omega_c t}\left(A\Phi + S_{IM} + S_{FM} + IP\right). \tag{3.75}$$

Transmission and detection

Following the fibre transmission, dispersion ($d(\omega_k)$ of Eq. (3.11)) is applied to each frequency component. The optical field at the output of the fibre is:

$$E_{out} = e^{j\omega_c t}\left(A\Phi + S_{IMout} + S_{FMout} + IP_{out}\right). \tag{3.76}$$

ω_c – optical carrier angular frequency

After direct detection, components can be divided into several groups: carrier-carrier beating (C^2), carrier-signal beating (CS), carrier-IP beating (CIP), signal-signal beating (different subcarriers beating with each other) ($2S$), signal-signal beating (each subcarrier beating with itself) (S^2), signal-IP (SIP) beating, IP-IP beating (different subcarriers beating with each other) ($2IP$) and IP-IP beating (IP^2).

Detected current can be written as follows:

$$\begin{aligned}
I_{Det.} =& \Re(2A\Phi S_{IMout}) + \Re(2A\Phi S_{FMout}) && (CS) && \{I_{Signal}\}\\
&+2\Re(S_{IMout})\Re(S_{IMout}) + 2\Im(S_{IMout})\Im(S_{IMout}) && (2S) && \{I_{SSII}\}\\
&+2\Re(S_{FMout})\Re(S_{FMout}) + 2\Im(S_{FMout})\Im(S_{FMout}) && (2S) && \{I_{SSII}\}\\
&+2\Re(S_{IMout})\Re(S_{FMout}) + 2\Im(S_{IMout})\Im(S_{FMout}) && (2S) && \{I_{SSII}\}\\
&+|S_{IMout}|^2 + |S_{FMout}|^2 && (S^2) && \{I_{SSII}\}\\
&+\Re(2A\Phi IP_{out}) && (CIP) && \{I_{SSII}\}\\
&+|A\Phi|^2 && (C^2) && \{discarded\}\\
&+2\Re(S_{IMout})\Re(IP_{out}) + 2\Im(S_{IMout})\Im(IP_{out}) && (SIP) && \{discarded\}\\
&+2\Re(S_{FMout})\Re(IP_{out}) + 2\Im(S_{FMout})\Im(IP_{out}) && (SIP) && \{discarded\}\\
&+2\Re(IP_{out})\Re(IP_{out}) + 2\Im(IP_{out})\Im(IP_{out}) && (2IP) && \{discarded\}\\
&+|IP_{out}|^2, && (IP^2) && \{discarded\}
\end{aligned} \tag{3.77}$$

where $\Re$ and $\Im$ are the real and imaginary parts of the component. The DC component ($|A\Phi|^2$) is discarded as it is of no interest. All IP-IP beating and Signal-IP beating are also not considered as these are the smallest components.

After derivation, the expression of the signal for a single subcarrier at ω_k is:

$$I_{k(Signal)}(t) = \zeta_{1(k)}\cos(\omega_k t) + \eta_{1(k)}\sin(\omega_k t), \tag{3.78}$$

and SSII landing on subcarrier ω_k:

$$\begin{aligned}
I_{k(SSII)}(t) =& \zeta_{2(k)}\cos(\omega_k t) + \eta_{2(k)}\sin(\omega_k t)\\
&+ \sum_{p=1}^{\lceil k/2\rceil-1} \zeta_{3(kp)}\cos(\omega_k t) + \sum_{p=1}^{\lceil k/2\rceil-1} \eta_{3(kp)}\sin(\omega_k t)\\
&+ \sum_{p=k+1}^{N} \zeta_{4(kp)}\cos(\omega_k t) + \sum_{p=k+1}^{N} \eta_{4(kp)}\sin(\omega_k t).
\end{aligned} \tag{3.79}$$

Several phasors are represented through their sine (ζ) and cosine (η) tributaries. Phasor $1(k)$ represents the signal current (variables $\zeta_{1(k)}$ and $\eta_{1(k)}$). Phasor $2(k)$ is composed of a group of correlated SSII frequency components (variables $\zeta_{2(k)}$ and $\eta_{2(k)}$). Each of the phasors $3(k)$ and phasors $4(k)$ is composed of a group of correlated SSII frequency components (variables $\zeta_{3..4(kp)}$ and $\eta_{3..4(kp)}$). These replacement variables are as follows:

$$\zeta_{1(k)} = A\Phi^2 2B_k \cos(d(\omega_k)), \tag{3.80}$$

$$\eta_{1(k)} = A^2\Phi^2 \frac{4J_{1(k)}}{J_{0(k)}} \sin(d(\omega_k)), \tag{3.81}$$

$$\zeta_{2(k)} = \Phi^2 \left(\left(-2AC_{k/2} + \frac{4A^2 J_{2(k/2)}}{J_{0(k/2)}} \right) \cos(d(\omega_k)) + \frac{B_{k/2}^2}{2} - \frac{2A^2 J_{1(k/2)}^2}{J_{0(k/2)}^2} \right), \tag{3.82}$$

$$\eta_{2(k)} = A\Phi^2 \frac{2B_{k/2} J_{1(k/2)}}{J_{0(k/2)}} \sin(d(\omega_k)), \tag{3.83}$$

$$\begin{aligned} \zeta_{3(kp)} =& 2A\Phi^2 \left(-D_{(k-p)p} + \frac{2AJ_{1(k-p)}J_{1(p)}}{J_{0(k-p)}J_{0(p)}} \right) \cos(d(\omega_k)) + \\ &+ \Phi^2 \left(B_{(k-p)}B_p - \frac{4A^2 J_{1(k-p)}J_{1(p)}}{J_{0(k-p)}J_{0(p)}} \right) \cos(d(\omega_{(k-p)}) - d(\omega_p)), \end{aligned} \tag{3.84}$$

$$\eta_{3(kp)} = 2A\Phi^2 \left(\frac{B_{(k-p)}J_{1(p)}}{J_{0(p)}} + \frac{B_p J_{1(k-p)}}{J_{0(k-p)}} \right) \sin(d(\omega_k)), \tag{3.85}$$

$$\begin{aligned} \zeta_{4(kp)} =& 2A\Phi^2 \left(-D_{p(p-k)} - \frac{2AJ_{1(p)}J_{1(p-k)}}{J_{0(p)}J_{0(p-k)}} \right) \cos(d(\omega_k)) + \\ &+ \Phi^2 \left(B_p B_{(p-k)} + \frac{4A^2 J_{1(p)}J_{1(p-k)}}{J_{0(p)}J_{0(p-k)}} \right) \cos(d(\omega_p) - d(\omega_{(p-k)})), \end{aligned} \tag{3.86}$$

$$\begin{aligned} \eta_{4(kp)} =& 2A\Phi^2 \left(\frac{B_{(p-k)}J_{1(p)}}{J_{0(p)}} - \frac{B_p J_{1(p-k)}}{J_{0(p-k)}} \right) \sin(d(\omega_k)) + \\ &+ 2A\Phi^2 \left(\frac{B_p J_{1(p-k)}}{J_{0(p-k)}} + \frac{B_{(p-k)}J_{1(p)}}{J_{0(p)}} \right) \sin(d(\omega_p) - d(\omega_{(p-k)})). \end{aligned} \tag{3.87}$$

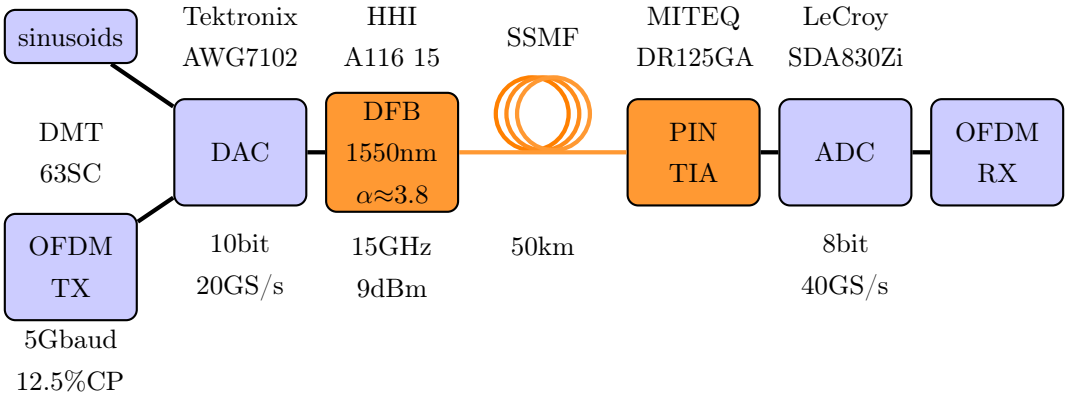

Figure 3.4: 5Gbaud experimental setup used for the analytical formulation experimental validation [15].

SNR prediction

Equations (3.78) and (3.79) can predict the amplitude and phase of a given subcarrier as well as the SSII landing on that subcarrier. For SNR prediction, signal and SSII amplitudes are calculated. This calculation differs for the case of unmodulated and modulated subcarriers.

For the unmodulated case, all phasors are correlated allowing sine and cosine amplitudes to be added separately and finally combined through the linear sum of sinusoids. For the modulated case, all phasors are assumed to be uncorrelated and the signal phasor magnitude is given by:

$$I_{k(Signal)} = \sqrt{\zeta_{1(k)}^2 + \eta_{1(k)}^2}, \tag{3.88}$$

whereas SSII is given by:

$$I_{k(SSII\cos)} = \zeta_{2(k)}^2 + \sum_{p=1}^{\lceil k/2 \rceil - 1} \zeta_{3(kp)}^2 + \sum_{p=k+1}^{N} \zeta_{4(kp)}^2, \tag{3.89}$$

$$I_{k(SSII\sin)} = \eta_{2(k)}^2 + \sum_{p=1}^{\lceil k/2 \rceil - 1} \eta_{3(kp)}^2 + \sum_{p=k+1}^{N} \eta_{4(kp)}^2, \tag{3.90}$$

$$I_{k(SSII)} = \sqrt{I_{k(SSII\cos)} + I_{k(SSII\sin)}}. \tag{3.91}$$

This SNR prediction formulation assumes that SSII is the dominant impairment in the system, nevertheless other noise sources can be added using BTB measurements. Other relevant noise sources are: quantization noise, photodiode noise and laser

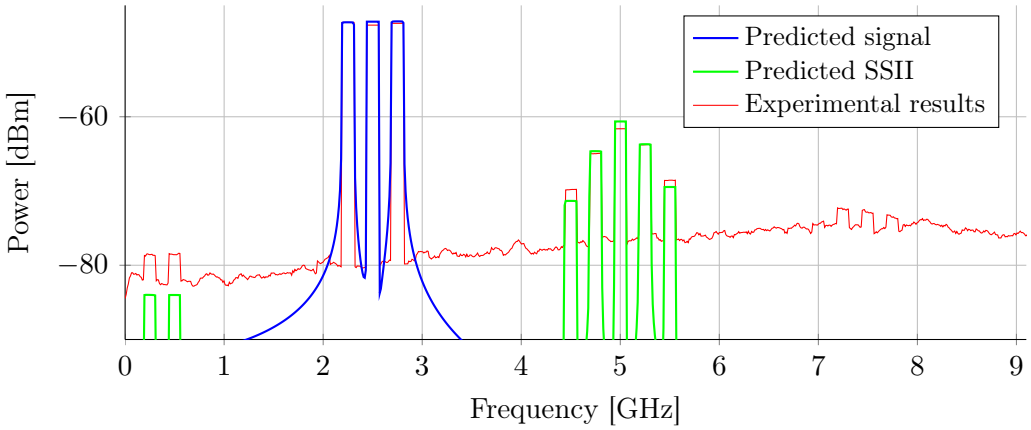

Figure 3.5: Predicted signal and SSII alongside experimental results for transmission after 50km SSMF using the 5Gbaud setup [15].

Relative **I**ntensity **N**oise (RIN). The total SNR for a single subcarrier is calculated as:

$$SNR_k = \frac{I_{k(Signal)}}{I_{k(SSII)} + \text{Noise}_{BTB}}. \tag{3.92}$$

3.4.3 Experimental Validation of the Analytical Formulation

The accuracy of the formulation is experimentally validated for both unmodulated and modulated signals. Initially one experimental setup is used having a low bandwidth **A**rbitrary **W**aveform **G**enerator (AWG) where sinusoids and a 5Gbaud DMT signal are transmitted; this setup is referred to as the 5Gbaud setup. In order to further test the formulation's accuracy a second experimental setup is used, this time having a larger bandwidth AWG. In this setup the transmitted signal is 20Gbaud DMT; it is referred to as the 20Gbaud setup.

5Gbaud Experimental Setup

In this setup (seen in Figure 3.4), two different signals are considered: unmodulated sinusoids and DMT. The 1024 symbol 5Gbaud **Q**uadrature **P**hase **S**hift **K**eying (QPSK) DMT signal contains 64 subcarriers (FFT size of 128) and includes 12.5% cyclic prefix. The AWG is a 10bit@20GS/s *Tektronix AWG7102*. The laser is a *Module A116 15* manufactured by the *Fraunhofer Heinrich-Hertz-Institut*. This module has a 3dB bandwidth of 15GHz@60mA with 9dBm peak output power and 3.8 α-factor. Laser bias is set at 1.4V (60mA, 6.5mW) and the driving signal swing

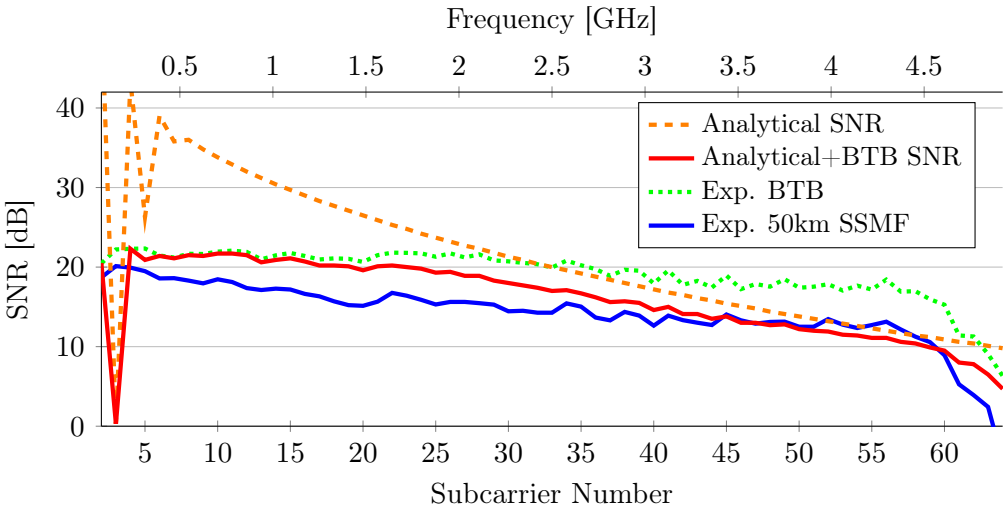

Figure 3.6: 5Gbaud DMT transmission after 50km SSMF. Analytical SNR prediction is shown with and without including BTB experimental SNR. Experimental SNR is also shown [15].

is 1Vpp ($m \approx 100\%$) to maximize the power budget. After 50km SSMF, the receiver *MITEQ DR-125G-A* PIN+TIA is used. The oscilloscope is a *LeCroy SDA830Zi*.

Validation for Unmodulated Signal

Using the 5Gbaud setup and unmodulated sinusoid transmission, the accuracy of the analytical formulation is tested in terms of amplitude prediction for both signal and SSII. Experimental results and predictions are shown in Figure 3.5(red).

It can be seen that the signal (blue at ≈2.5GHz) is correctly predicted with minimal error. Also the SSII landing at $2\omega_k$ and $\omega_k+\omega_p$ (green at ≈5GHz) are correctly predicted. SSII landing at $\omega_k-\omega_p$ (green at ≈0.3GHz) shows a prediction error of around 5dB. The components seen in the experimental signal (red at ≈7.5GHz) are outside the range of the considered frequency components of the analytical formulation.

Validation for 5Gbaud DMT

Using the 5Gbaud setup, a DMT signal is transmitted in BTB and after 50km SSMF. After demodulation and decoding, **E**rror **V**ector **M**agnitude (EVM) is measured for each subcarrier. Using the procedure described in [83], EVM is converted into SNR.

Results can be observed in Figure 3.6(solid blue). The analytical formulation

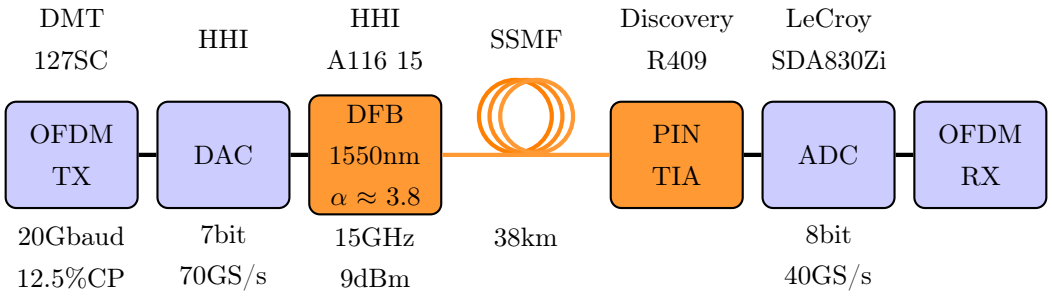

Figure 3.7: 20Gbaud experimental setup used for the experimental validation of the analytical formulation [15].

correctly predicts larger impact of SSII on high frequencies (dashed orange) [84]. As the lower frequency subcarriers are mainly limited by noise, experimentally measured BTB noise (dotted green) was included in the prediction (solid orange).

The analytical formulation on its own does not predict the degradation of the last five subcarriers; this is due to the low-pass characteristic of the system. The first three odd subcarriers are estimated incorrectly, showing very low SNR; the noted inaccuracy is due to simplifications during the derivation process, a more in-depth analysis is performed in Section 3.4.4.

20Gbaud Experimental Setup

In this setup (Figure 3.7), a 1024 symbol 20Gbaud QPSK DMT signal with 128 subcarriers (FFT size of 256) and 12.5% cyclic prefix is used. The AWG has 6bit@70GS/s and is manufactured by the *Fraunhofer Heinrich-Hertz-Institut*. The laser is the same as in the previous setup, biased at 1.6V (80mA, 8mW) and the driving signal swing is 1.6Vpp having ≈10% voltage swing below the laser threshold resulting in clipping. After 38km SSMF the receiver *Discovery Semiconductor R409* PIN+TIA is used. The oscilloscope is the same as in the previous setup.

Validation for 20Gbaud DMT

Having shown that the analytical formulation correctly predicts SSII, a second test is performed using the 20Gbaud setup. The combination of higher bandwidth and a larger modulation index leads to higher chirp and therefore higher SSII, even though the fibre is shorter.

Experimental results for DMT transmission can be observed in Figure 3.8(solid

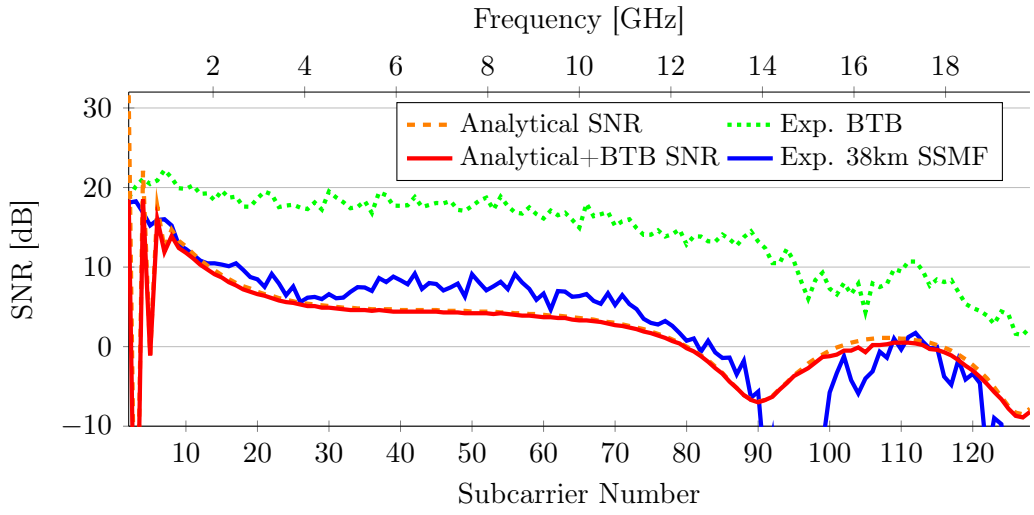

Figure 3.8: 20Gbaud DMT transmission after 38km SSMF. Analytical SNR prediction is shown with and without including BTB experimental SNR. Experimental SNR is also shown [15].

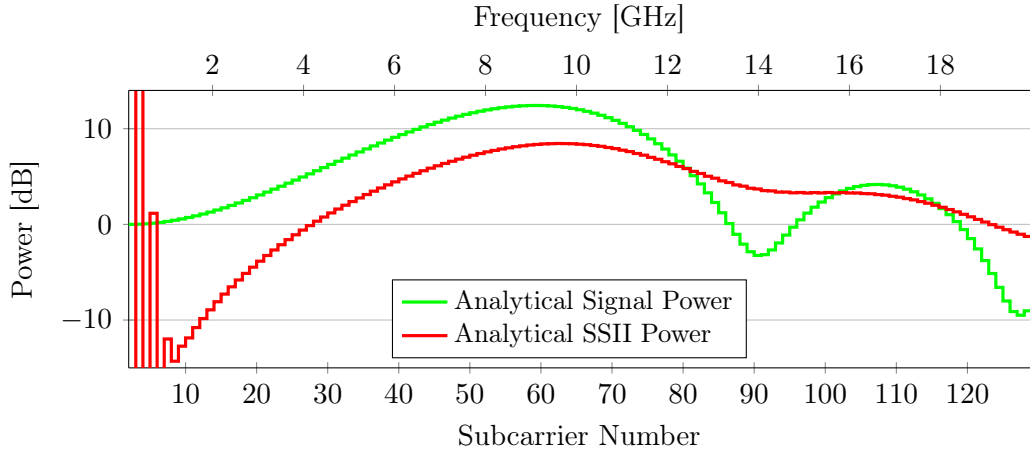

Figure 3.9: 20Gbaud DMT transmission after 38km SSMF. Analytical signal and SSII powers prediction used to calculate analytical SNR of Figure 3.8.

blue). Similarly to the lower bandwidth DMT transmission, BTB noise measurements were included (dashed green) in the prediction (solid orange). The predicted relative powers for signal and SSII can be seen in Figure 3.9.

Odd low frequency subcarriers are estimated incorrectly for high m (Figures 3.6, 3.8 and 3.9). This occurrence was already verified for the previous validation (Section 3.4.4 offers an in-depth analysis). The SSII for odd low frequency subcarriers can be estimated by interpolating the prediction for even neighbouring subcarriers.

The predicted power fading has an offset relative to the experimental data (subcar-

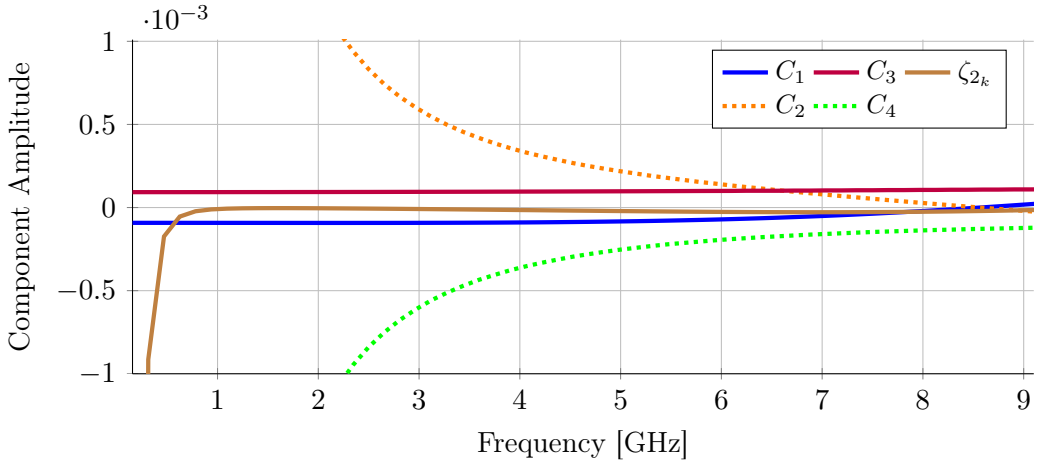

Figure 3.10: Frequency of $2\omega_k$ landing SSII due to $\zeta_{2(k)}$ and its components C_1−C_4 of Eqs. (3.93) and (3.96).

riers 90–102). This is due to the usage of the simplified laser model in the formulation. This model does not consider intensity and frequency modulation phase of Eqs. (2.34) and (2.36) respectively.

The analytical formulation is generally accurate as shown by experimental results, even for large m.

3.4.4 Analytical Formulation Low Frequency Accuracy

Figures 3.6, 3.8 and 3.9 show incorrect predictions for the first three odd subcarriers: 3, 5 and 7 (subcarrier 1 was discarded). These inaccuracies are present only for low frequencies subcarriers where the $\zeta_{2(k)}$ phasor (Eqs. (3.79) and (3.82)) lands in odd subcarriers. This is due to a high magnitude of $\phi(t)$ (Eq. (3.69)) for high frequency subcarriers (ω_k in the denominator). This, in turn, leads to large $J_{1(k)}$ and $J_{2(k)}$ magnitudes. The magnitude of this phasor is compounded by an asymmetrical cancellation of its components. This leads to inaccurate SNR prediction for low frequency subcarriers. An expansion of Eq. (3.82) can be performed yielding its four components $\zeta_{2(k)}$=C_1+C_2+C_3+C_4:

$$C_1 = -\Phi^2 2AC_{k/2}\cos(d(\omega_k)), \tag{3.93}$$

$$C_2 = \Phi^2 \frac{4A^2 J_{2(k/2)}}{J_{0(k/2)}}\cos(d(\omega_k)), \tag{3.94}$$

$$C_3 = \Phi^2 \frac{B_{k/2}^2}{2}, \tag{3.95}$$

$$C_4 = -\Phi^2 \frac{2A^2 J_{1(k/2)}^2}{J_{0(k/2)}^2}. \tag{3.96}$$

The value of each component, as well as the value of $\zeta_{2(k)}$, can be seen in Figure 3.10. The components that are not cancelling each other can be seen to be C_2(dashed orange) and C_4(dashed green). Note that for high frequencies C_2 and C_4 converge to a negative value. This is partially compensated by a signal shift of C_1(solid blue), leading to a small contribution of $\zeta_{2(k)}$ to the total SSII.

Derivation of the formulation with less simplifications would lead to other components that would correct the deviation of $\zeta_{2(k)}$, but would be less compact.

3.5 Conclusion

In this Chapter, transmission impairments of cost-effective OFDM-based systems were characterized. Initially, fibre transmission was described with special attention given to CD. Fibre effects, not considered in this work, were briefly mentioned and justification was provided for their non-inclusion.

CD-induced power fading was described for an ideal intensity modulation case and an expression for a detected signal was derived. The expression predicting the location of power fading nulls was derived from the detected signal.

To support the description of SSII, the previous derivation for power fading was extended to include phase modulation. This introduced, in part, simplifications that were used in subsequent derivations of this chapter.

To enable prediction for experimental transmission systems, a simplified laser model was created along with means to configure it using datasheet information and simplified measurements. Several versions of the laser model were compared, using simulations, with a rate equation model justifying simplification choices.

Expanding on previous derivations, a formulation was derived that is capable of predicting signal and SSII powers. Here a bigger emphasis was given to the description of the underlying cause of SSII as well as the concept leading to the derivation. An in-depth derivation is presented in Appendix F.

This formulation is capable of predicting SNR for both modulated and unmodulated sinusoids. Using a low bandwidth experimental setup the formulation was experimentally validated, initially for unmodulated sinusoids and later for OFDM transmission. A second, larger bandwidth experimental setup was used to validate

the formulation, in this case only for OFDM transmission. The formulation was found to be accurate in the prediction of SNR degradation due to SSII.

Limitations were found in the prediction for low frequency subcarriers. These can be attributed to simplifications performed, the components responsible for this limitation were identified.

Chapter 4

Equalization

Equalization is the compensation of distortions introduced by the transmission channel. It can be performed either at the transmitter or at the receiver side.

At the transmitter side, the signal is pre-distorted to counteract channel distortions. This type of equalization is also known as pre-distortion. Bit loading and power loading are two common pre-distortion techniques generally used in multicarrier communication systems [85], [86]. These are especially advantageous in OFDM systems where commonly high number of subcarriers allow finer adaptation to the channel characteristics. The iterative bit-and-power loading algorithm [16] used in this work's experiments is presented in this Chapter.

At the receiver side, equalization can be used as a means to mitigate channel non-linearities [87]. Later in this Chapter, Volterra filtering is introduced and an adaptive Volterra filter based equalizer capable of mitigating SSII is presented. An optimization procedure using experimental data is detailed. The equalizer is then optimized using experimental data. Finally its ability to mitigate SSII and increase capacity is assessed.

4.1 Bit-and-power Loading

Bit loading and power loading are two pre-distortion techniques commonly used in tandem. Bit loading adapts subcarriers to the transmission channel in terms of constellation density. It has the goal of maximising total capacity for a given SNR.

Power loading aims to equalize a common metric among all subcarriers, for instance **B**it **E**rror **R**ate (BER). This is achieved by transferring power from better

performing subcarriers to worse performing ones. When a subcarrier is disabled, its power is distributed among all other subcarriers. Subcarrier disabling due to low SNR prevents inefficient use of power, for instance in frequency ranges affected by power fading.

Whenever changes in subcarrier powers lead to linear variations in SNR, power distribution can be performed if the SNR is foreknown. This procedure uses a single SNR measurement and is denominated as a water filling (or water pouring) algorithm. One use for this type of algorithms is in the telephone line digital system DSL [85], [88], [89].

For some systems, changes in the power of a given subcarrier can also affect the SNR of other subcarriers. This behaviour can be caused by SSII, where the SNR of each subcarrier is affected by intermixing products from other subcarriers. In such systems it is not straightforward to predict which subcarrier's SNR will be affected by a change in power of any of the other subcarriers. The lack of knowledge of this dependence can be circumvented with the use of an iterative algorithm. An algorithm of this type performs changes in the transmitted signal, analyses the resulting BER and adapts to these changes to converge to a solution.

An iterative bit-and-power loading algorithm [16] is described in detail. This algorithm is used in experiments presented in this work.

4.1.1 Iterative Bit-and-Power Loading Algorithm

The developed bit-and-power loading algorithm aims to maximize system capacity with all subcarriers respecting a given metric. This is achieved by a combination of constellation density selection (coarse granularity) and power control (fine granularity). Subcarriers with high SNR can support more capacity and have their constellation density increased; conversely, when suffering from low SNR, a subcarrier has its constellation density reduced or is disabled. Power changes serve to finely equalize subcarriers. BER is the metric used to determine if a subcarrier can support a given constellation or whether power transfer should occur.

Bit loading and power loading are implemented separately with power loading serving as a subset of two distinct bit loading adaptation steps: coarse adaptation and fine tuning. Coarse adaptation starts by transmitting all subcarriers with equal power and large constellation densities and aims to reduce the capacity of each subcarrier to quickly find a solution where all subcarriers perform better than the

B group			Power Transfer		W group		
index	SC num.	BER			index	SC num.	BER
B_1	3	10×10^{-10}	20%	(ΔA)	W_8	8	10×10^{-1}
B_2	2	10×10^{-9}	15%		W_7	7	10×10^{-2}
B_3	4	10×10^{-7}	10%		W_6	1	10×10^{-4}
B_4	5	10×10^{-6}	5%	(ΔA_m)	W_5	6	10×10^{-5}

Table 4.1: Exemplary power transfer between eight subcarriers during power loading. Subcarriers are initially sorted according to performance and divided in two groups, indexes are assigned: B_n for best performing and W_n for worst performing. The B group (left) transfers power to the W group (right) according to the power transfer (centre) distribution defined between ΔA and ΔA_m. Each subcarrier number and BER is also shown [16].

target BER (BER_T). Fine tuning increases the constellation density of a given carrier and tests if the BER target condition is violated. If this is the case, the previous configuration represents maximum system capacity.

Power Loading

Power loading's goal is to equalize BER among all active subcarriers. This is achieved by power transfer between better and worse performing subcarriers. Active subcarriers are sorted according to performance and divided into two groups for power transfer: B is the best performing group and W is the worst performing group. Both groups are of the same size, implying that for an odd number of subcarriers the middle performing subcarrier belongs to neither group and sees no power change. The total number of subcarriers taken into account for power transfer is denoted by N, making each group size to be $N/2$. Indexing is performed according to BER performance B_1 being the best performing subcarrier overall and W_N the worst performing subcarrier overall. The worst performing subcarrier of the B group is $B_{N/2}$, whereas the best performing subcarrier of the W group is $W_{N/2+1}$.

Both groups are aligned with inverse ordering creating subcarrier pairs for power transfer. Subcarrier B_1 transfers power to W_N and $B_{N/2}$ transfers power to $W_{N/2+1}$. The performance difference (BER) between the subcarrier pair B_1 and W_N is larger than the one of the subcarrier pair $B_{N/2}$ and $W_{N/2+1}$. This is reflected in the amount of power transferred between the two subcarrier pairs, which varies linearly between the maximum (ΔA) and the minimum (ΔA_m), both user defined. Table 4.1 shows

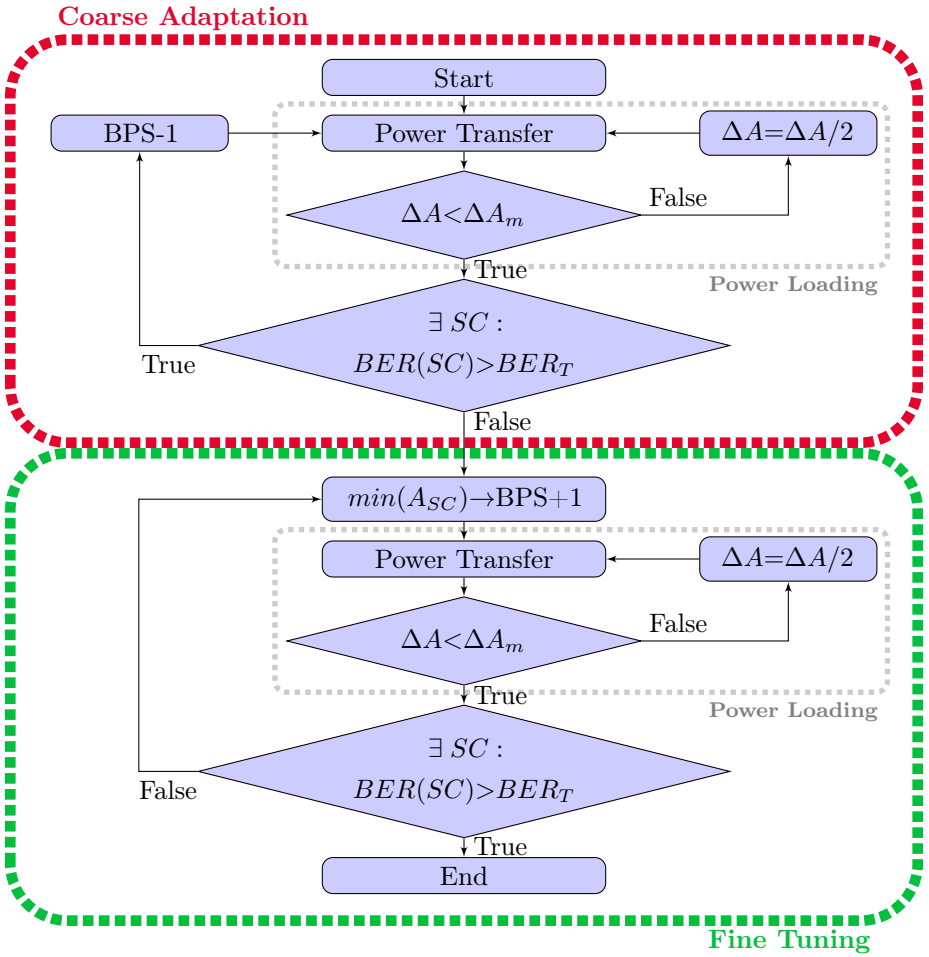

Figure 4.1: Flowchart of the bit-and-power loading algorithm where ΔA is halved every iteration [16].

an example of power transfer.

In order to improve convergence, ΔA is halved after each iteration due to the difference in performance between B_1 and W_N becoming closer. When the halving of ΔA would cause it to be smaller than ΔA_m, the power loading run is complete. At the start of subsequent runs ΔA is set to its original value.

Whenever all subcarriers have BER below the target BER (BER_T), power loading is stopped in order to reduce the total number of iterations. Power loading can be seen as part of the bit-and-power loading flowchart in Figure 4.1.

Coarse Adaptation

This step starts with all subcarriers having large constellation sizes chosen by the user (**Start** in Figure 4.1). One run of power loading strives to equalize BER among all

subcarriers. Each subcarrier having BER above target (BER_T) has its constellation size reduced by one bit-per-symbol (**BPS-1** in Figure 4.1), subsequent power loading and constellation size reduction sequences are performed until all subcarriers have their BER below BER_T.

Convergence speed is improved in this step by performing constellation changes on several subcarriers at once. This allows a wide diversity of configurations to be tested in a short time frame. Due to bit-per-symbol changes in several subcarriers at once, capacity might not be maximized.

Fine Tuning

Fine tuning aims to achieve maximum system capacity. By starting from a known good solution, this step is able to identify the best candidate subcarrier for capacity increase: the lowest amplitude subcarrier ($min(A_{SC})$ in Figure 4.1). The power loading sequence is run afterwards. This process is repeated until, after the power loading sequence, one or more subcarriers have BER above BER_T. The previous solution is taken as the one leading to maximum capacity achieved by the algorithm for the defined BER target.

Subcarrier Disabling

When a subcarrier has very low SNR, for example due to power fading, its capacity is decreased and its amplitude is increased in subsequent iterations. This can lead to the subcarrier consuming high power for its low capacity, thus reducing total system capacity. To prevent this, a user defined limit for the ratio between bits-per-symbol and subcarrier power is defined. Whenever a subcarrier exhibits a ratio lower than the limit, is an indication of a too high power usage for a given constellation density and the subcarrier is disabled.

4.2 Volterra Equalization

Nonlinear filtering has been successfully used to increase power budget and capacity in OFDM-based access systems [84], [90]. Equalization using Volterra filters has been proven to mitigate CD and channel nonlinearities in baseband binary DD systems [87]. SSII reduction was also shown in IMDD OFDM 100Gb/s transmission systems [91].

This Section presents an adaptive receiver side equalizer that is based on a Volterra filter and is capable of dynamically adjusting its coefficients to channel conditions.

4.2.1 Volterra Filter

The Volterra filter is based on the discrete causal Volterra series [87]:

$$\vec{y}[n] = \sum_{p=1}^{P} \left[\sum_{\tau_1=0}^{M-1} \cdots \sum_{\tau_p=0}^{M-1} h_p(\tau_1, \ldots, \tau_p) \prod_{j=1}^{p} \vec{x}[n-\tau_j] \right]. \tag{4.1}$$

The series input and output are the discrete vectors $\vec{x}[n]$ and $\vec{y}[n]$ respectively. The series kernel is $h_p(\tau_1, \ldots, \tau_p)$. The kernel size (number of taps) for each order is given by the number of permutations with repetition:

$$|h_p| = M^p. \tag{4.2}$$

Kernel size and number of multiplications can be reduced by combining products of samples that occur more than once. For instance, the second order scalar product $\vec{x}[n-\tau_1]\vec{x}[n-\tau_2]$ occurs twice for $\tau_1{=}0, \tau_2{=}1$ and $\tau_1{=}1, \tau_2{=}0$. The two kernel values $h_2(0,1)$ and $h_2(1,0)$ are averaged and stored as $h_2(0,1)$. Applying this simplification to Eq. (4.1):

$$\vec{y}[n] = \sum_{p=1}^{P} \left[\sum_{\tau_1=0}^{M-1} \sum_{\tau_2=\tau_1}^{M-1} \cdots \sum_{\tau_p=\tau_p-1}^{M-1} h_p(\tau_1, \ldots, \tau_p) \prod_{j=1}^{p} \vec{x}[n-\tau_j] \right], \tag{4.3}$$

the kernel size (number of taps) is now given by the number of combinations with repetition [92]:

$$|h_p| = \left(\!\!\binom{M}{p}\!\!\right) = \frac{(M+p-1)!}{p!(M-1)!}. \tag{4.4}$$

Studied SSII is limited to the 2nd order, as such the Volterra series is truncated to the 2nd order ($P{=}2$) and represented by:

$$\vec{y}[n] = \sum_{\tau_1=0}^{M-1} h_1(\tau_1)\vec{x}[n-\tau_1] + \sum_{\tau_1=0}^{M-1} \sum_{\tau_2=\tau_1}^{M-1} h_2(\tau_1, \tau_2)(\vec{x}[n-\tau_1]\vec{x}[n-\tau_2]). \tag{4.5}$$

$\vec{y}[n]$ – output vector
$\vec{x}[n]$ – input vector
P – Volterra series order
$h_p(\tau_1, \ldots, \tau_p)$ – Volterra series kernels for order p
M – Volterra series memory

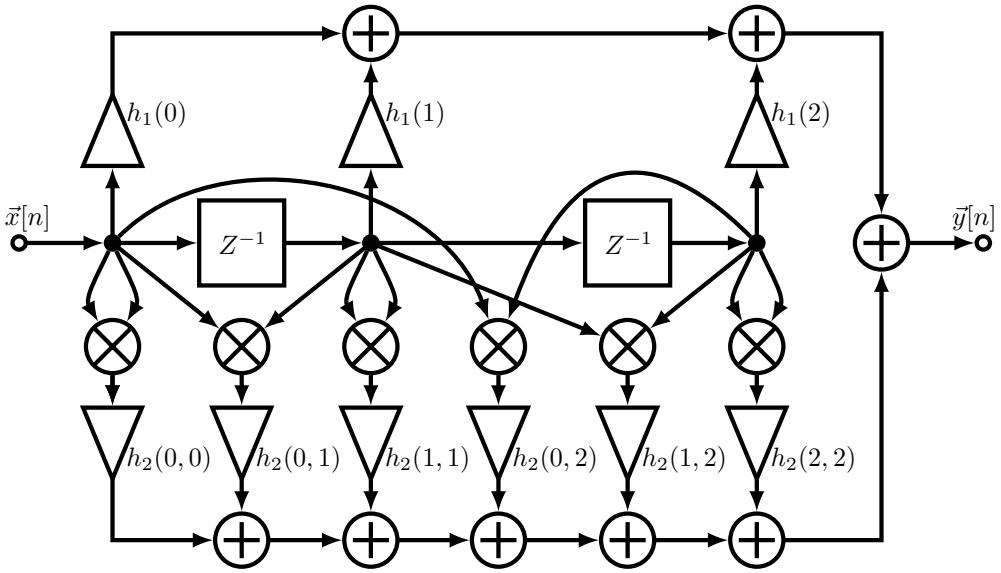

Figure 4.2: Volterra implementation for N=3 and M=3 [17].

The series has a linear (1st order) and a nonlinear part (2nd order). The linear part of Eq. (4.5) represents a **F**inite **I**mpulse **R**esponse (FIR) filter. The nonlinear part can be implemented as a nonlinear FIR filter.

To have separate control of the linear and nonlinear filter parts, linear filter memory (N) is introduced:

$$\vec{y}[n] = \sum_{\tau_1=0}^{N-1} h_1(\tau_1)\vec{x}[n-\tau_1] + \sum_{\tau_1=0}^{M-1}\sum_{\tau_2=\tau_1}^{M-1} h_2(\tau_1,\tau_2)(\vec{x}[n-\tau_1]\vec{x}[n-\tau_2]). \tag{4.6}$$

Separate control of filter memories enables better convergence in systems with different linear and nonlinear memories. Figure 4.2 shows an exemplary Volterra filter schematic representation of Eq. (4.6).

4.2.2 Filter Implementation and Adaptation

The Volterra filter is placed in the digital signal path after the sampled output of the ADC and before the OFDM decoder. The filter processes the digital representation of the analogue OFDM signal. The output of the filter is desirably the original transmitted signal. In this case all distortions would have been cancelled.

For distortion mitigation to occur, filter taps (kernel values) need to be carefully optimized. One option for tap optimization is to use an algorithm to automatically adapt the taps.

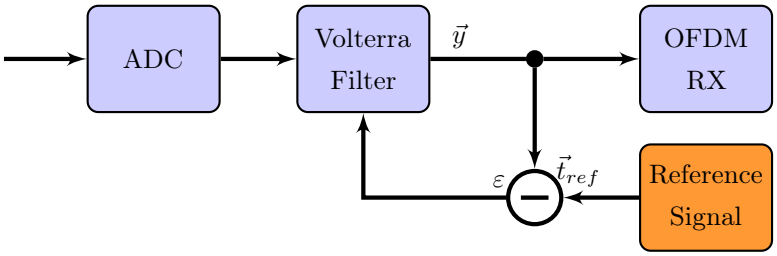

Figure 4.3: Volterra equalizer in the OFDM digital signal path [17].

A metric is needed to aid the algorithm in adapting the taps. One option is to use received symbols to generate a metric, such is the case of a **D**ecision **F**eedback **E**qualizer (DFE), where the difference between received symbols and decided symbols (after threshold) is used [93]. For an OFDM system, **S**ymbol **E**rror **R**ate (SER) could be used instead. Having the OFDM decoder inside the filter adaptation loop, in order to access SER, does not require the storage of training signals. This approach is challenging to implement.

A less complex solution is to compare the filter output samples with the transmitted signal in order to produce an error signal that can be used for tap adaptation. The disadvantage is that in practical systems the receiver has no information on the transmitted signal. This can be overcome by storing a specific signal (training sequence) at the receiver and transmitting it whenever filter adaptation is required. As both sequences must be synchronized, this approach can also be used for system synchronization. The conceptual representation of such an equalizer can be seen in Figure 4.3.

Tap adaptation is performed through the minimization of the error signal ε: the difference between the stored training sequence $\vec{t}_{ref}$ and its received and filtered version $\vec{y}$. The coefficients can be trained using the **L**east **M**ean **S**quares (LMS) algorithm [87] or alternatively using **R**ecursive **L**east **S**quares (RLS) [87]. In this work, the LMS algorithm is used.

The pseudocode representation of the Volterra equalizer is presented in Page 73 (Algorithm 1). The equalizer code takes as input: the received signal ($x[n]$), the reference signal ($t_{ref}[n]$), the linear filter memory size (N), the nonlinear filter memory size (M) and the adaptation step size (μ). Here, for each input sample, two sets of samples ($l_{samples}$ and nl_{buffer}) are collected according to the memory lengths N and M (lines: 6 and 7). These contain current and past samples. Sample multiplication is performed for the nonlinear part (lines: 8 and 9). Both the linear samples ($l_{samples}$)

Algorithm 1 Pseudocode of the Volterra filter with adaptation

1: **Input:** $x[n], t_{ref}[n], N, M, \mu$
2: $h_1 \leftarrow \{0, \ldots, 0, 1, 0, \ldots, 0\}$ (size=N)
3: $h_2 \leftarrow \{0, \ldots, 0, 1, 0, \ldots, 0\}$ (size=M)
4: $n \leftarrow$ length of x
5: **for** $i \leftarrow 0, n$ **do**
6: $\quad l_{samples} \leftarrow x[i - N : i]$
7: $\quad nl_{buffer} \leftarrow x[i - M : i]$
8: $\quad$ **for** $j \leftarrow 0, M$ **do**
9: $\quad\quad nl_{samples}[j] \leftarrow nl_{buffer}[j] * nl_{buffer}[j : M]$
10: $\quad$ **end for**
11: $\quad y[i] \leftarrow h_1 \cdot l_{samples} + h_2 \cdot nl_{samples}$
12: $\quad \varepsilon \leftarrow t_{ref}[i] - y[i]$
13: $\quad h_1 \leftarrow h_1 + \mu * \varepsilon * l_{samples}/(l_{samples} \cdot l_{samples})$
14: $\quad h_2 \leftarrow h_2 + \mu * \varepsilon * nl_{samples}/(nl_{samples} \cdot nl_{samples})$
15: **end for**

and the results of sample multiplication ($nl_{samples}$) are themselves multiplied by the taps h_1 and h_2 (line 11), generating the equalizer output $y[n]$. The error ε is calculated by subtracting the reference signal $\vec{t}_{ref}$ from the equalizer output (line 12). Finally, both taps are updated (lines: 13 and 14) by dividing the samples by their self scalar product which is multiplied by the error and adaptation step (μ) and finally added to the current taps.

4.2.3 Volterra Equalizer Optimization

Volterra filter memory size impacts its performance. A filter shorter than the channel memory may not compensate transmission distortions. A long filter may not compensate distortions adequately due to convergence difficulties of the training algorithm [94]. This Section presents an optimization procedure for the Volterra equalizer using experimental results.

In Section 4.2.2, the notions of linear (N) and nonlinear (M) memories were introduced. Performance comparison between filters with different memories can only be performed when both filters operate at the same ADC sample rate. When this is not the case, both the ADC sample rate and the filter memory can be defined in

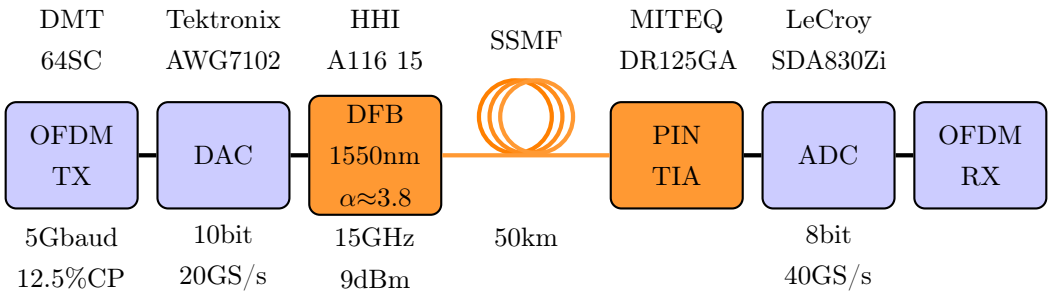

Figure 4.4: 5Gbaud experimental setup [18].

terms of samples-per-symbol and symbol periods respectively. For large numbers of subcarriers, the period of an OFDM frame can be longer than the effect the filter aims to mitigate. For this reason, both the symbol rate and period are defined relatively to the baudrate. The ADC sample rate (r) is measured in multiples of the baudrate, whereas the memory length is measured in symbol periods (T_s=baudrate^{-1}). For instance, a filter operating at r=2 with memories N=3T_s and M=3T_s has half the size of a filter with the same memory size operating at r=4.

5Gbaud Experimental Setup

In this setup (Figure 4.4), 1024 symbol 5Gbaud **c**ircular **Q**uadrature **A**mplitude **M**odulation (cQAM) DMT signal with 64 subcarriers (FFT size of 128) and 12.5% cyclic prefix is transmitted. The AWG is a 10bit@20GS/s *Tektronix AWG7102*. The laser is a *Module A116 15* manufactured by the *Fraunhofer Heinrich-Hertz-Institut*. This module has a 3dB bandwidth of 15GHz@60mA having 9dBm peak output power and 3.8 α-factor. Laser bias is set at 1.4V (60mA, 6.5mW) and the driving signal swing is set at 1Vpp (m≈100%) to maximize the power budget. After 50km SSMF, the receiver *MITEQ DR-125G-A* PIN+TIA is used. The LeCroy SDA830Zi oscilloscope serves as an 8bit@40GS/s ADC. The values for laser bias and digital signal clipping are optimized in conjunction with the bit-and-power loading algorithm to maximize system capacity for a target BER of 1×10^{-3}. Signal generation, decoding and BER estimation is performed using *VPItransmissionMaker Optical Systems*.

Optimization Results

Unequalized (Volterra off) transmission after 50km SSMF yields a net capacity of 11.48Gb/s using a bit-and-power loading target BER of 1×10^{-3}. Without changing

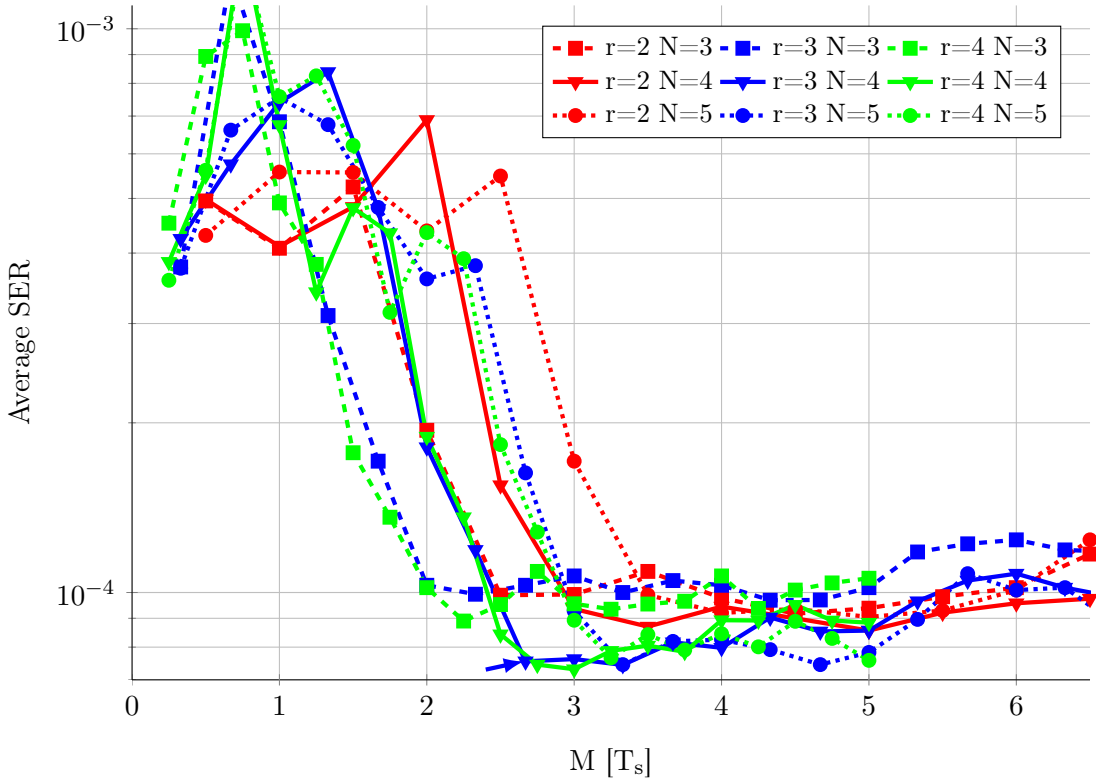

Figure 4.5: Averaged SER for different designs of the Volterra equalizer having different sampling rates, linear (N) and nonlinear (M) memory sizes. The blue arrow indicates the selected configuration [18].

the bit-and-power loading profile, several configurations of the Volterra equalizer are tested. Each equalizer is optimized using the same training sequence and afterwards the same test signal is used to evaluate equalizer performance. This is done by comparison of average SER. In order to facilitate the visualization of filter performance variations, average SER is plotted against the nonlinear memory size M in terms of symbol periods (T_s). The resulting graph can be seen in Figure 4.5. Different filters are grouped by colour, according to the used ADC sample rate, and by line and marker types, according to the linear memory size N. The ADC sample rate is in the range of r=[2, 4]. Linear filter sizes are in the range of N=[3, 5]T_s. The smallest nonlinear filter is of size one and therefore has zero delay elements. Due to different sample rates used for different filters, the minimum nonlinear memory in terms of symbol periods (T_s) is different. Depicted nonlinear memory is in the range M=]0, 6.5]T_s.

There is a general trend of SER reduction for increasing nonlinear memory sizes. For larger sample rates and low nonlinear memory (M) sizes an initial degradation

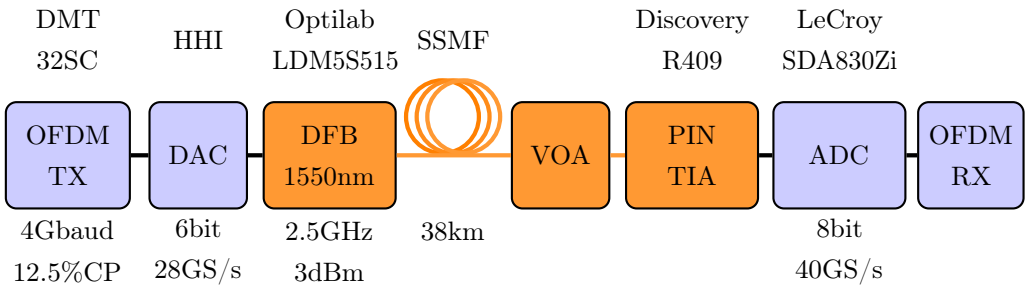

Figure 4.6: 4Gbaud experimental setup [17].

is noted, especially for larger linear memory (N) sizes. Small M is not enough for distortion mitigation, especially in conjunction with larger N.

For large M ($>3.5\mathrm{T_s}$), performance begins to degrade in most cases. This is due to exponential nonlinear tap increase (Eq. (4.4)) which hampers convergence. Also, this shows that the nonlinear memory of the considered link does not exceed $3.5\mathrm{T_s}$.

Filters with $N{=}3\mathrm{T_s}$ converge quicker, but show a residual penalty. For $N{=}5\mathrm{T_s}$, there is slower convergence while showing no significant performance improvement. This indicates that the linear memory of the link does not exceed $5\mathrm{T_s}$.

The optimum value for N is $4\mathrm{T_s}$. For 2 samples-per-symbol, a residual error due to sampling at the Nyquist rate is observed. For 3 and 4 samples-per-symbol the convergence is quicker. Their performance is similar but $r{=}4$ shows a marginal improvement at the cost of a larger filter.

Selection of the equalizer configuration is performed using two criteria: performance and size. The lowest SER results are seen in Figure 4.5 around $M{=}3\mathrm{T_s}$ for $r{=}3$ and $r{=}4$, where the smallest filters have the optimum value of $N{=}4\mathrm{T_s}$. The smallest filter with BER$<8{\times}10^{-5}$ is selected. It has the configuration $r{=}3$, $N{=}4\mathrm{T_s}$ (12 samples) and $M{=}2.67\mathrm{T_s}$ (8 samples), indicated by a blue arrow in Figure 4.5.

4.2.4 Volterra Equalizer Performance

Volterra equalization is experimentally validated using two IMDD P2P experimental setups: a 4Gbaud setup using a cost-effective laser suited for the uplink of access systems [17], the schematic for this setup can be seen in Figure 4.6; and the 5Gbaud setup that was already used to investigate Volterra equalizer optimization in Section 4.2.3.

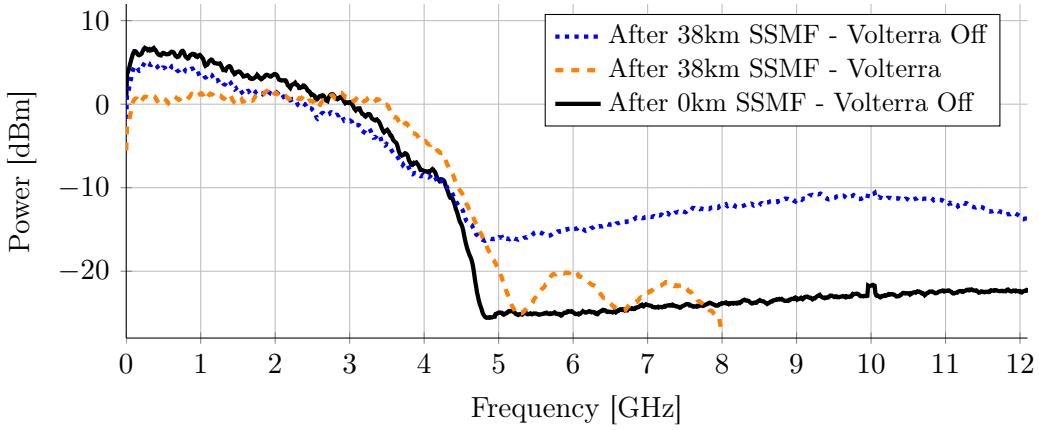

Figure 4.7: 4Gbaud experimental received spectra (BTB and 38km) for a 16cQAM transmission with all subcarriers having the same power. The effect of Volterra equalization on out-of-band SSII can be seen (dotted blue vs. dashed orange) [17].

4Gbaud Experimental Setup

In this setup (Figure 4.6), a 1024 symbol 4Gbaud cQAM DMT signal with 32 subcarriers (FFT size of 64) and 12.5% cyclic prefix is transmitted. The AWG has 6bit@28GS/s and is manufactured by the *Fraunhofer Heinrich-Hertz-Institut*. The laser is an *Optilab LDM5S515* with an analogue bandwidth of 2.5GHz@30mA and 3dBm maximum output power. This laser is intended for CWDM analogue communication schemes and for cable television transmission systems return paths. Laser bias is set at 1.1V (41mA) and the modulation index is set at 60%, allowing enough power budget for the considered transmission distance. After 38km SSMF a **V**ariable **O**ptical **A**ttenuator (VOA) controls ROP. The receiver is a *Discovery Semiconductor R409* PIN+TIA. The oscilloscope is a *LeCroy SDA830Zi*. Signal equalization, OFDM decoding and BER estimation are performed offline using *VPItransmissionMaker Optical Systems*.

4Gbaud results

In order to show the effect of Volterra equalization in signal spectra, a DMT signal is used with all subcarriers having the same power and modulation (16cQAM). Transmission was performed at optical BTB and after 38km SSMF. The signal received after 38km SSMF was also Volterra equalized. The Volterra filter was configured with r=4, N=12T_s (48 samples) and M=8T_s (32 samples).

The resulting spectra can be seen in Figure 4.7. The BTB spectrum (solid black)

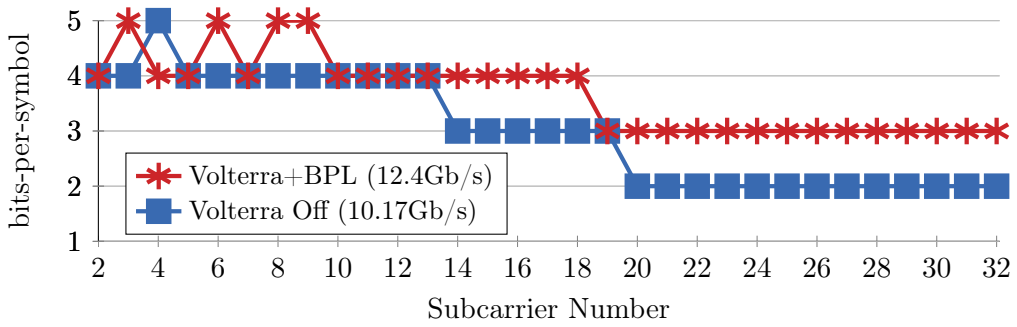

Figure 4.8: 4Gbaud system bit loading resulting of: bit-and-power loading algorithm on the unequalized system (Volterra Off) and bit-and-power loading algorithm using Volterra equalization (Volterra+BPL).

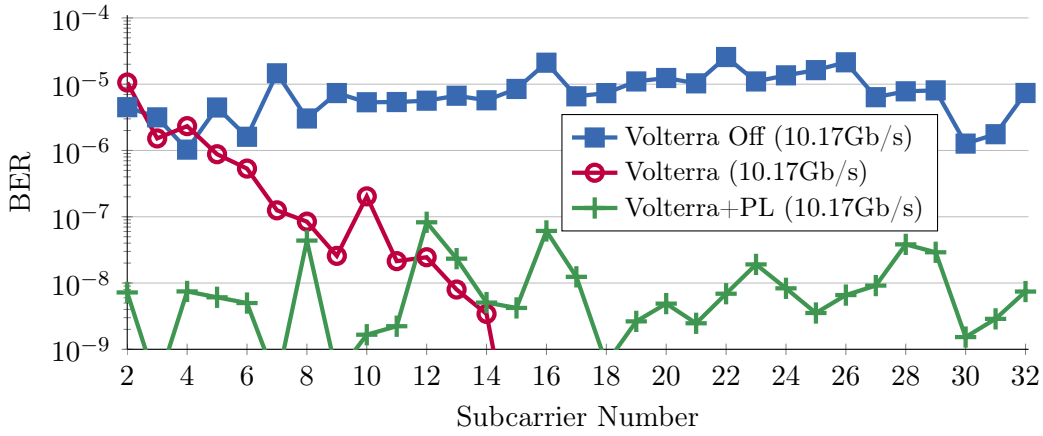

Figure 4.9: 4Gbaud experimental BER results for transmission after 38km SSMF for: unequalized system after bit-and-power loading (Volterra Off), after enabling Volterra equalization without changing the bit-and-power loading profile (Volterra) and after running power loading on the Volterra equalized system (Volterra+PL) [17].

clearly shows the low-pass characteristic of the system. The received spectrum after 38km SSMF (dotted blue) shows out-of-band SSII not present in the BTB spectrum. The magnitude of the out-of-band SSII can be used as an indication of the magnitude of SNR degradation due to SSII landing inside the signal band. The reduction of the out-of-band SSII (above 5GHz) is seen in the equalized spectrum (dashed orange). This indicates SSII mitigation, which is confirmed by BER results.

Before examining BER improvement due to Volterra equalization, the system capacity was gauged. For this, the bit-and-power loading algorithm was run on the unequalized system. The target BER was set to a conservative 1×10^{-5}, net capacity was found to be 10.17Gb/s. The resulting bit loading and BER can be seen in Figure 4.8 and Figure 4.9(blue squares) respectively.

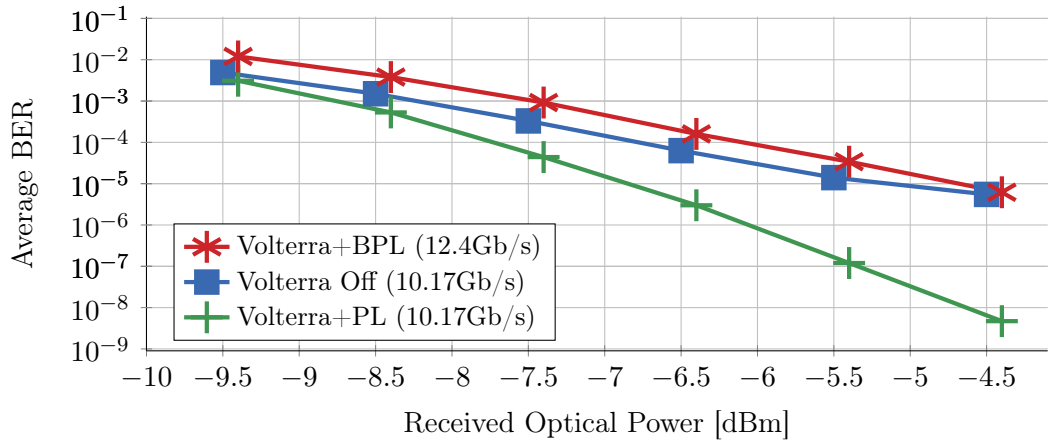

Figure 4.10: 4Gbaud BER vs. ROP for transmission after 38km SSMF for: unequalized system after bit-and-power loading (Volterra Off), after running power loading on the Volterra equalized system (Volterra+PL) and after running bit-and-power loading on the Volterra equalized system (Volterra+BPL) [17].

The results of Volterra equalization are shown in Figure 4.9(purple circles). The higher frequency subcarriers experience a greater reduction in BER. This result agrees with the prediction of Section 3.4.3.

Finally, a new power loading was run to gauge the reduction in BER. These results are shown in Figure 4.10(green crosses), where the signal is close to being error free (BER$\simeq 5\times10^{-9}$). A new bit-and-power loading was performed to increase system capacity allowing an improvement of $\approx$22.6% to a net capacity of 12.4Gb/s.

Three configurations are compared at different ROP in Figure 4.10: unequalized (blue squares), Volterra equalized with power loading (green crosses) and Volterra equalized with bit-and-power loading (red stars).

For a ROP of -4.4dBm, both signals: unequalized (blue squares) and equalized with bit-and-power loading (red stars), show the same BER. This is due to the bit-and-power loading algorithm being run on both systems (VOA off) at this ROP and with the same BER threshold. For ROP above -5.5dBm the unequalized signal (blue squares) shows an error floor caused by SSII being the dominant impairment as the effect of receiver noise is reduced. Below -5.5dBm the behaviour of the equalized signal with new bit-and-power loading (red stars) is similar to the unequalized signal (blue squares), the former having slightly worse BER. This is due to the higher capacity signal (red stars) being more sensitive to increases in receiver noise. Receiver noise is now the dominant noise source, since SSII was mitigated.

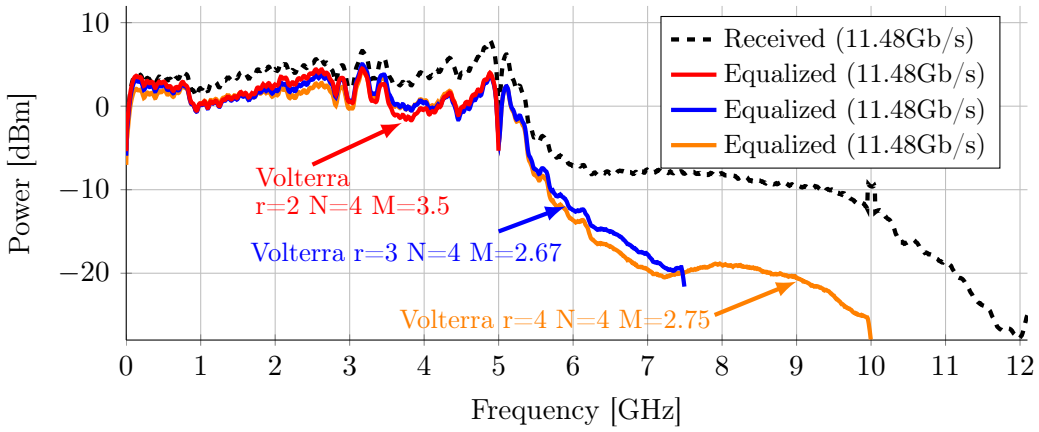

Figure 4.11: 5Gbaud experimentally received spectra with bit-and-power loading. The unequalized signal (black) and three different Volterra configurations are shown [18].

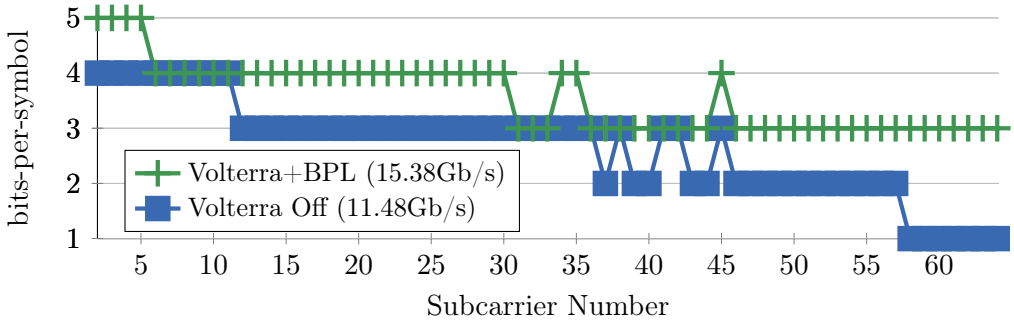

Figure 4.12: Initial bit loading for the unequalized system (5Gbaud) and new bit loading performed after Volterra equalization [18].

When comparing the unequalized signal (blue squares) against the equalized signal with power loading (green crosses), the difference in performance is noticeable for higher ROP, where receiver noise becomes less dominant and SSII is mitigated. At low ROP all signals have similar performance as the Volterra equalizer is unable to compensate for the stochastic receiver noise. The noise floor seen in the unequalized signal (blue squares) indicates that even though SSII is the dominant impairment, there is still contribution from the receiver noise. Volterra equalization is able to compensate for SSII allowing for more than 20% capacity increase.

5Gbaud results

This setup was previously used in Section 4.2.3 for optimization of the Volterra equalizer; details are shown in Figure 4.4. Compared with the 4Gbaud setup, both higher bandwidth and transmission length (50km instead of 38km) contribute to

higher SSII. The capacity of the unequalized system after running the bit-and-power loading algorithm was found to be 11.48Gb/s net; bit loading results are shown in Figure 4.12(blue squares).

The selected Volterra equalizer configuration is r=3, N=4T_s(12 samples) and M=2.67T_s(8 samples). Its effect on out-of-band SSII can be seen, along with a good performing configuration having r=4 in Figure 4.11. For r=2 the effect is not seen due to the limited sample rate.

The bit-and-power loading algorithm is run with the Volterra equalizer on. Bit loading results can be seen in Figure 4.12(green crosses). Net capacity improved from 11.48Gb/s to 15.38Gb/s, which represents an improvement of $\simeq$33%.

4.3 Conclusion

In this Chapter, an iterative bit-and-power loading algorithm, suitable for systems having nonlinear SNR dependence on subcarrier power, was presented and validated. This algorithm was used, in part or full, to perform equalization of subcarrier BER and to maximize system capacity.

Also in this chapter, an adaptive equalizer capable of mitigating SSII arising from chirp-CD interaction was presented, optimized and had its performance experimentally verified. For this, two different experimental setups were used, one with a rate of 4Gbaud using a low bandwidth DML suitable for uplink, another operating at 5Gbaud using a higher bandwidth laser. Both setups used transmission distances well in excess of the maximum distance prescribed in PON standards. Using the 5Gbaud setup, a filter optimization procedure was demonstrated. It was used to obtain a filter configuration that could provide a compromise between filter size and performance. The optimization procedure showed better performance for longer filters when compared with shorter ones. The best performing filter configuration is long enough to compensate for channel effects, with performance slowly degrading for further size increases. Progressively larger filters show increasing convergence difficulties.

Making use of the Volterra equalization, capacity was shown to increase by more than 20% for the 4Gbaud system. The longer length and larger bandwidth 5Gbaud system, consequentially having larger SSII, saw its capacity improved by $\simeq$33%.

Volterra equalization was demonstrated to be of value for the mitigation of SSII

arising from chirp-CD interaction.

Chapter 5

Summary

This work encompasses contributions to the analysis and efficient mitigation of impairments for cost-effective OFDM-based access systems. A simplified laser model and the procedure to configure it, using datasheet parameters, were presented. Means of predicting SNR degradation due to SSII were developed in the form of a compact formulation, which was derived and experimentally validated. Mitigation of SSII using Volterra-based equalization was demonstrated.

Initially, a discussion of access systems' state of the art was performed. The differences between AONs and PONs were presented. The latter, being the most common one, was subject of special attention in the form of: historical evolution of standards, possible network topologies, components and frequency allocation. The requirement for C-band usage was therefore justified. Commonly used modulation formats used in access systems were also presented. The motivation for using OFDM in access systems was justified.

After an in-depth review of the OFDM modulation format attention was given to other key technologies such as electro-optic and analogue-digital conversions. Transmission impairments were also characterized, with special emphasis given to CD and the by-product of its interaction with chirp (SSII), which is the most significant impairment in DMDD access systems operating in the C-band. The generation of SSII was briefly discussed in terms of the components arising from direct detection.

One main achievement of this work was to derive a compact analytical formulation capable of predicting SNR degradation. SSII generation was discussed in greater detail during the derivation. In this process, the simplified laser model was employed

to provide IM and FM responses. The process of deriving the analytical formulation is presented in the main body of this work. A more in-depth derivation is relegated to Appendix F. This compact analytical formulation was found to be accurate in predicting the amplitudes of OFDM subcarriers after transmission in DMDD, CD-impaired access systems. The interactions between signal and intermixing interference products (SSII) were used to produce SNR predictions. Even though in the analytical modelling process subcarriers are represented with unmodulated sinusoids, the analytical formulation was able to predict SSII-induced SNR degradation for both unmodulated and modulated subcarriers. For the latter, the individual contribution of the many interference components was considered to be uncorrelated. Experimental results showed good agreement except for very low frequency subcarriers. This is due to performed simplifications, the components leading to the mismatch were identified. During the derivation process, it was shown that intermixing interferences are limited to the second order. This fact enabled a correct choice of the order of the equalizer used for SSII mitigation. The derived compact analytical formulation can be a valid tool for system analysis especially in terms of gaining a deeper understanding of SNR degradation for specific subcarriers.

An iterative bit-and-power loading algorithm was developed to aid in subcarrier equalization and capacity maximization. It can take into account nonlinear changes in SNR caused by changes in subcarrier power. The applicability of this algorithm was validated in several experiments and is used throughout this work to equalize subcarrier's bit error rate.

Another main achievement of this work is the development of an adaptive equalizer capable of mitigating SSII arising from chirp-CD interaction. The equalizer is based on a second order Volterra filter and is able to adapt to channel conditions using the **L**east **M**ean **S**quares (LMS) algorithm. During training, a signal known as a training sequence is transmitted. Being stored at the receiver, it is compared with the equalizer output to generate the error signal used by the LMS algorithm to adapt the filter. A study of equalizer performance for different sample rates and memories was presented. This was found to be dependent on filter size. Small memories are unable to correctly compensate SSII, whereas progressively large memories show convergence difficulties. Results obtained from the equalizer's experimental validation show not only its ability in SSII mitigation but also served to further prove SNR trends predicted by the derived analytical formulation. For a particular OFDM-based

DMDD system focusing on low-cost broadband access application, this equalizer enabled an improvement in capacity of $\simeq$33%.

Outlook

One of the objectives of this work was to derive a compact analytical formulation to aid in system analysis through SNR estimation. Throughout its derivation, several decisions were made in terms of which components to discard. Studies can be performed to ascertain the impact of each simplification on precision and compactness of the derivation. The related low frequency subcarrier mismatch detailed in Section 3.4.4 can also be resolved by investigating the origin of the missing parameter that enables the cancellation of the C_2 and C_4 components of $\zeta_{2(k)}$.

The development of a hybrid bit-and-power loading algorithm, making use of the analytical formulation, can be investigated. The formulation usage can provide a good starting configuration, speeding up convergence; alternatively, the formulation can be used to predict the consequences of subcarrier power changes, enabling the algorithm to require less iterations to converge.

The emergence of the use of low cost VCSEL in the C-band prompts experimental trials of the formulation to infer on its suitability for SNR prediction for these devices in cost-effective OFDM-based access systems.

Implementation of the Volterra equalizer in real-time systems can also be investigated. Filter parallelization could be performed and its maximum memory sizes inferred for specific hardware implementations.

Appendix A

List of Symbols

ω_k	k subcarrier angular frequency
rect	rectangular function
$\xrightarrow{\mathcal{F}}$	Fourier transform
$*$	convolution
δ	Dirac delta function
sinc	normalized sinc function: $\text{sinc}(x)=\sin(\pi x)/(\pi x)$ where $\text{sinc}(0)=1$
$\mathcal{F}^{-1}[t']$	inverse discrete Fourier transform
R_s	symbol rate (N/T)
β	roll-off factor
T	OFDM frame period
I	injection current
q	magnitude of the electron charge
γ_e	carrier recombination rate
N	carrier population
G	nonlinear gain
P	photon population
γ_p	photon decay rate
R_{sp}	spontaneous emission rate
ω_0	lasing mode frequency
ω_{th}	lasing mode frequency at threshold
α_c	linewidth enhancement factor, or α-factor
m	modulation index

ΔI_{mod}	variation of the modulation current
I_{bias}	bias current
I_{th}	threshold current
$\frac{\partial G}{\partial N}$	gain derivative relative to the carrier population
I_p	peak value of the modulation current
Ω_R	angular frequency of the relaxation oscillation peak
Γ_R	relaxation oscillation decay rate
Γ_P	small signal decay rate of the fluctuations in the photon population
$\alpha(dB/km)$	fibre loss parameter
L	fibre length in km
P_{out}	output power at the fibre end
P_{in}	input power coupled at the fibre input
ω_c	optical carrier angular frequency
β	propagation constant
v_φ	phase velocity
$\bar{n}$	fibre effective refractive index
c	speed of light in vacuum
v_g	group velocity
$\bar{n}_g$	fibre group index
ω_g	group angular frequency
β_g	group propagation constant
λ	wavelength
γ	fibre nonlinear coefficient
L_{eff}	effective interaction length $L_{eff} \approx \left[1 - \exp\left(-\left(\frac{\alpha(dB/km)}{4343}\right) L\right)\right] / \left(\frac{\alpha(dB/km)}{4343}\right)$
Δ	phase matching condition
Ω	channel spacing
D_p	PMD parameter
Δ_p	laser intensity response
Δ_f	laser chirp response
θ_p	laser intensity phase shift
θ_f	laser chirp delay relative to intensity modulation

$\phi(t)$	phase modulation due to frequency modulation arising from laser chirp
$S_{mod}(t)$	intensity modulating signal
U_k	k subcarrier amplitude
$\vec{y}[n]$	output vector
$\vec{x}[n]$	input vector
P	Volterra series order
$h_p(\tau_1, \ldots, \tau_p)$	Volterra series kernels for order p
M	Volterra series memory
Γ_N	small signal carrier decay rate

Appendix B

Acronyms

AC **A**lternating **C**urrent

ADC **A**nalogue to **D**igital **C**onverter

ADSL **A**symmetric **D**igital **S**ubscriber **L**ine

AM **A**mplitude **M**odulation

AON **A**ctive **O**ptical **N**etwork

APD **A**valanche **P**hoto**d**iode

ASK **A**mplitude-**s**hift **K**eying

AWG **A**rbitrary **W**aveform **G**enerator

BER **B**it **E**rror **R**ate

BTB **B**ack-**t**o-**B**ack

CAP **C**arrierless **A**mplitude **P**hase Modulation

CD **C**hromatic **D**ispersion

CO **C**entral **O**ffice

CO-OFDM **C**oherent **O**ptical **OFDM**

CP **C**yclic **P**refix

cQAM **c**ircular **Q**uadrature **A**mplitude **M**odulation

CW **C**ontinuous **W**ave

DAC **D**igital to **A**nalogue **C**onverter

DC **D**irect **C**urrent

DD **D**irect **D**etection

DDO-OFDM **D**irect **D**etection **O**ptical **OFDM**

DFB **D**istributed **F**eed**b**ack

DFE **D**ecision **F**eedback **E**qualizer

DFT **D**iscrete **F**ourier **T**ransform

DM **D**irect **M**odulation

DMDD **D**irect **M**odulation **D**irect **D**etection

DML **D**irectly **M**odulated **L**aser

DMT **D**iscrete **M**ulti**T**one

DSB **D**ouble **S**ide**b**and

DSL **D**igital **S**ubscriber **L**ine

EAM **E**lectro-**A**bsorption **M**odulator

EDFA **E**rbium-**d**oped **F**ibre **A**mplifier

EVM **E**rror **V**ector **M**agnitude

FBMC **F**ilter **B**ank **M**ulti**c**arrier

FDM **F**requency **D**ivision **M**ultiplexing

FDMA **F**requency **D**ivision **M**ultiple **A**ccess

FFT **F**ast **F**ourier **T**ransform

FIR **F**inite **I**mpulse **R**esponse

FM **F**requency **M**odulation

FMF **F**ew **M**ode **F**ibre

FP **F**abry-**P**erot

FSR **F**ull **S**cale **R**ange

FTTX **F**ibre **t**o **t**he **X**

FWM **F**our-**W**ave **M**ixing

GVD **G**roup-**V**elocity **D**ispersion

ICI **I**nter**c**arrier **I**nterference

iDFT **i**nverse **D**iscrete **F**ourier **T**ransform

IEEE **I**nstitute of **E**lectrical and **E**lectronics **E**ngineers

IF **I**ntermediate **F**requency

IM **I**ntensity **M**odulation

IMDD **I**ntensity **M**odulation **D**irect **D**etection

ISI **I**nter**s**ymbol **I**nterference

ITU **I**nternational **T**elecommunication **U**nion

LMS **L**east **M**ean **S**quares

LSB **L**ower **S**ide-**B**and

MCF **M**ulti-**C**ore **F**ibre

MIMO **M**ultiple-**I**nput **M**ultiple-**O**utput

MMF **M**ulti-**M**ode **F**ibre

MZM **M**ach–**Z**ehnder **M**odulator

NRZ **N**on-**R**eturn-to-**Z**ero

OFDM **O**rthogonal **F**requency **D**ivision **M**ultiplexing

OLT **O**ptical **L**ine **T**erminal

ONT **O**ptical **N**etwork **T**erminal

ONU **O**ptical **N**etwork **U**nit

OOK **O**n-**O**ff **K**eying

P2P **P**oint to **P**oint

PAM **P**ulse **A**mplitude **M**odulation

PAPR **P**eak-to-**A**verage **P**ower **R**atio

PM **P**hase **M**odulation

PMD **P**olarization **M**ode **D**ispersion

PON **P**assive **O**ptical **N**etwork

PSK **P**hase-**s**hift **K**eying

QAM **Q**uadrature **A**mplitude **M**odulation

QPSK **Q**uadrature **P**hase **S**hift **K**eying

RF **R**adio **F**requency

RIN **R**elative **I**ntensity **N**oise

RLS **R**ecursive **L**east **S**quares

RMS **R**oot **M**ean **S**quare

ROP **R**eceived **O**ptical **P**ower

SBS **S**timulated **B**rillouin **S**cattering

SCMA **S**ub**c**arrier **M**ultiple **A**ccess

SDMA **S**pace **D**ivision **M**ultiple **A**ccess

SER **S**ymbol **E**rror **R**ate

SMF **S**ingle-**M**ode **F**ibre

SNR **S**ignal-to-**N**oise **R**atio

SOA **S**emiconductor **O**ptical **A**mplifier

SPM **S**elf-**P**hase **M**odulation

SRS **S**timulated **R**aman **S**cattering

SSB **S**ingle **S**ide-**B**and

SSB-OFDM **S**ingle **S**ide-**B**and OFDM

SSII **S**ubcarrier-to-**S**ubcarrier **I**ntermixing **I**nterference

SSMF **S**tandard **S**ingle-**M**ode **F**ibre

TDM **T**ime **D**ivision **M**ultiplexing

TDMA **T**ime **D**ivision **M**ultiple **A**ccess

USB **U**pper **S**ide-**B**and

VCSEL **V**ertical **C**avity **S**urface **E**mitting **L**aser

VOA **V**ariable **O**ptical **A**ttenuator

WDM **W**avelength **D**ivision **M**ultiplexing

WDMA **W**avelength **D**ivision **M**ultiple **A**ccess

XPM Cross-**P**hase **M**odulation

Appendix C

Real and Imaginary notation in OFDM

Devices, such as DACs, are either limited in terms of bandwidth or have a prohibitive cost for the required bandwidth. This imposes a limitation on the direct generation of OFDM signals at high frequencies. The alternative is to generate the OFDM signal at a lower frequency and up-convert it to a higher frequency (RF). The usual means for this conversion is the IQ modulator as it offers a compact spectrum.

Initially, this Appendix highlights the difference between RF carrier and IQ modulator up-conversion.

Finally, the process of OFDM generation and up-conversion using a DFT is described. More specifically, the relationship between: DFT frequency bins, iDFT outputs and IQ modulated signal is shown.

C.1 RF Carrier Up-conversion

As seen in Eq. (2.12), an OFDM signal can simply be described as a sum of modulated RF subcarriers:

$$s(t) = \sum_{k=1}^{N} I_k(t)\cos(\omega_k t) - Q_k(t)\sin(\omega_k t). \tag{C.1}$$

This equation can also be described using a phasor as seen in Eq. (2.14):

$$s(t) = \Re\left\{\sum_{k=1}^{N}(I_k(t) + jQ_k(t))e^{j\omega_k t}\right\}. \tag{C.2}$$

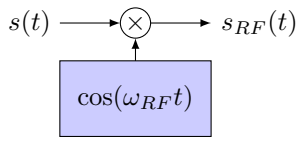

Figure C.1: Baseband OFDM signal up-conversion by multiplication with an RF carrier.

OFDM subcarriers in baseband can be up-converted to a higher frequency through multiplication with an RF carrier. An example of such a setup can be seen in Figure C.1. The resulting signal is:

$$s_{RF}(t) = \cos(\omega_{RF}t)\left(\sum_{k=1}^{N} I_k(t)\cos(\omega_k t) - Q_k(t)\sin(\omega_k t)\right). \tag{C.3}$$

Noting the following relations:

$$\cos\alpha\cos\beta = \frac{1}{2}(\cos(\alpha-\beta)+\cos(\alpha+\beta)), \tag{C.4}$$

$$\cos\alpha\sin\beta = \frac{1}{2}(-\sin(\alpha-\beta)+\sin(\alpha+\beta)), \tag{C.5}$$

carrier multiplication results in:

$$\begin{aligned} s_{RF}(t) = \sum_{k=1}^{N} &\frac{I_k(t)}{2}\cos((\omega_{RF}-\omega_k)t) + \frac{Q_k(t)}{2}\sin((\omega_{RF}-\omega_k)t) \\ &+\frac{I_k(t)}{2}\cos((\omega_{RF}+\omega_k)t) - \frac{Q_k(t)}{2}\sin((\omega_{RF}+\omega_k)t). \end{aligned} \tag{C.6}$$

The resulting Eq. (C.6) shows that after multiplication with an RF carrier, the up-converted OFDM signal is modulated into the upper and lower side-bands. The bandwidth of the up-converted signal is double of the baseband signal. Modulation of both side-bands occurs due to the control of the RF carrier being limited to amplitude (phase is not controlled), similarly to laser direct modulation.

C.2 IQ Modulator Up-conversion

In order to also control the carrier phase, an IQ modulator is used. This type of modulator requires two input signals, QAM symbols for example. For the case of OFDM, the real and imaginary parts of each OFDM subcarrier are fed to the modulator instead. Knowing that:

$$e^{j\omega t} = \cos(\omega t) + j\sin(\omega t), \tag{C.7}$$

the OFDM baseband signal representation can be converted from polar to rectangular form:

$$\sum_{k=1}^{N}(I_k(t)+jQ_k(t))e^{j\omega_k t}=\sum_{k=1}^{N}(I_k(t)+jQ_k(t))(\cos(\omega_k t)+j\sin(\omega_k t)). \tag{C.8}$$

The right side of Eq. (C.8) is now expanded:

$$S(t)=\sum_{k=1}^{N}I_k(t)\cos(\omega_k t)-Q_k(t)\sin(\omega_k t)+jI_k(t)\sin(\omega_k t)+jQ_k(t)\cos(\omega_k t). \tag{C.9}$$

IQ modulation is performed as in Eq. (2.16):

$$s_{RF}(t)=\cos(\omega_{RF}t)\Re\{S(t)\}-\sin(\omega_{RF}t)\Im\{S(t)\}, \tag{C.10}$$

using also the relations:

$$\sin\alpha\sin\beta=\frac{1}{2}(\cos(\alpha-\beta)-\cos(\alpha+\beta)), \tag{C.11}$$

$$\sin\alpha\cos\beta=\frac{1}{2}(\sin(\alpha-\beta)+\sin(\alpha+\beta)), \tag{C.12}$$

IQ modulation leads to:

$$\begin{aligned}s_{RF}(t)=&\sum_{k=1}^{N}\frac{I_k(t)}{2}\cos((\omega_{RF}-\omega_k)t)+\frac{I_k(t)}{2}\cos((\omega_{RF}+\omega_k)t)\\&+\frac{Q_k(t)}{2}\sin((\omega_{RF}-\omega_k)t)-\frac{Q_k(t)}{2}\sin((\omega_{RF}+\omega_k)t)\\&-\frac{I_k(t)}{2}\cos((\omega_{RF}-\omega_k)t)+\frac{I_k(t)}{2}\cos((\omega_{RF}+\omega_k)t)\\&-\frac{Q_k(t)}{2}\sin((\omega_{RF}-\omega_k)t)-\frac{Q_k(t)}{2}\sin((\omega_{RF}+\omega_k)t),\end{aligned} \tag{C.13}$$

removing the cancelling terms:

$$s_{RF}(t)=\sum_{k=1}^{N}I_k(t)\cos((\omega_{RF}+\omega_k)t)-Q_k(t)\sin((\omega_{RF}+\omega_k)t). \tag{C.14}$$

By using an IQ modulator, an equation similar to Eq. (C.1) is obtained. The process can also be interpreted as SSB modulation. In this case only the upper side-band is obtained ($\omega_{RF}+\omega_k$).

$1+\cos(\omega_2 t)+\cos(\omega_3 t)+\cos(\omega_4 t) \overset{(i)DFT}{\Leftrightarrow}$

ω_1 (DC)	ω_2	ω_3	ω_4	ω_5 $(\omega_{Nyq.})$	$-\omega_4$	$-\omega_3$	$-\omega_2$

Figure C.2: Fourier transform representation in terms of frequency bins of a real valued signal using (i)DFT. Complex numbers are not shown.

C.3 IQ Modulation of DFT Output

Due to the efficiency of FFT algorithms, DFTs are commonly used to generate OFDM signals. The frequency bins resulting from the DFT of a real signal can be seen in Figure C.2. The values at negative frequencies are complex conjugates (Hermitian symmetry) of values at positive frequencies and $\omega_{Nyq.}$ is the Nyquist frequency. Note that it is not possible to control the phase of the subcarrier at the Nyquist frequency as it has only two samples-per-period. The DFT performs the conversion of a time domain signal to complex frequency domain representation. The inverse operation makes use of an iDFT. By respecting Hermitian symmetry, DMT can be generated.

Using different symbols in the positive and negative frequency bins breaks the Hermitian symmetry leading to a complex output of the iDFT. The complex signal can be separated in its real and imaginary components. Each of the subcarriers of the baseband signals contains information of the positive and negative frequency subcarriers. After up-converting the signal using an IQ modulator, the overlapping baseband subcarriers are separated, as seen in Figure C.3.

The complex signal of the *DC* bin will modulate the RF carrier. The complex signal of the $\omega_{Nyq.}$ bin will be modulated into both side-bands of the RF carrier. The remaining frequency bins will generate real and imaginary subcarriers. As aforementioned, each of these contains information of both the positive and negative frequency subcarriers. After up-conversion, each subcarrier modulates one of the side-bands of the RF carrier. Taking as an example the frequency bins $\pm\omega_2$ of Figure C.3 and the subcarriers at frequency ω_2 in the same figure, the up-conversion result can be calculated. Renaming the symbol variables from (I_2, Q_2) to (I_a, Q_a) and (I_b, Q_b) for ω_2 and $-\omega_2$ respectively, the following equation can be written as:

$$S(t) = (I_a(t) + jQ_a(t))e^{j\omega_2 t} + (I_b(t) + jQ_b(t))e^{-j\omega_2 t}, \tag{C.15}$$

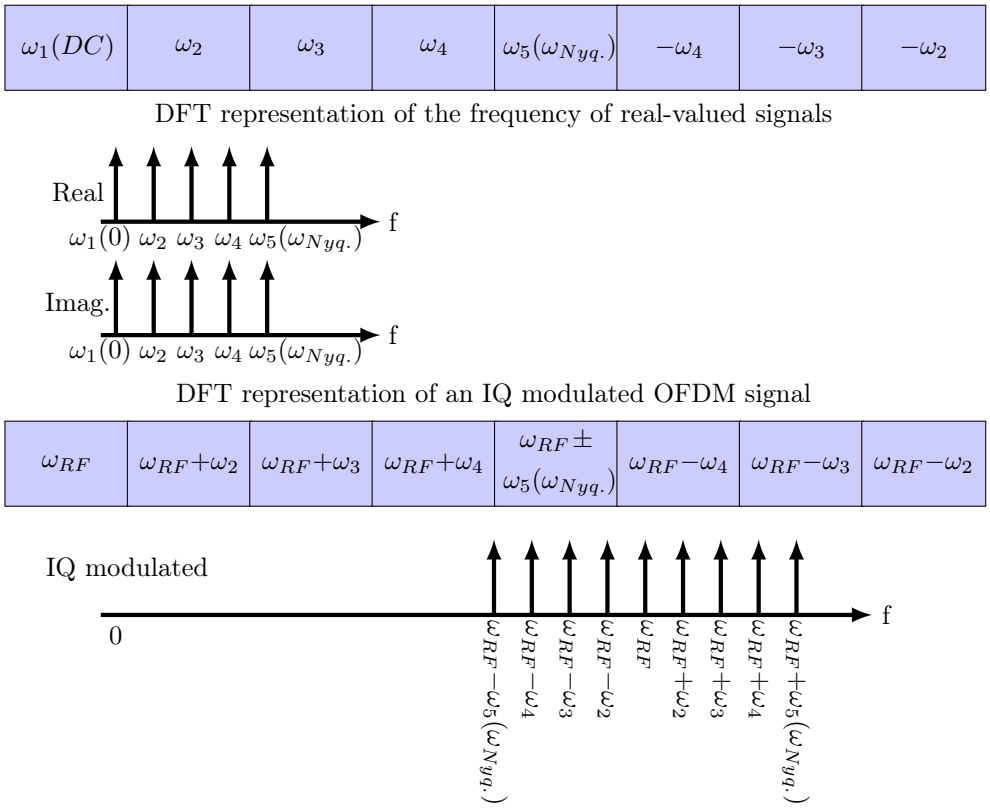

Figure C.3: DFT representations and subcarrier assignment of real-valued signals and IQ modulated OFDM. Spectra are also shown.

which can be converted to rectangular form:

$$\begin{aligned} S(t) =& I_a(t)\cos(\omega_2 t) - Q_a(t)\sin(\omega_2 t) + jI_a(t)\sin(\omega_2 t) + jQ_a(t)\cos(\omega_2 t) \\ &+ I_b(t)\cos(\omega_2 t) + Q_b(t)\sin(\omega_2 t) - jI_b(t)\sin(\omega_2 t) + jQ_b(t)\cos(\omega_2 t). \end{aligned} \tag{C.16}$$

The in-phase and quadrature contribution of I_a, Q_a and I_b, Q_b to the real and imaginary subcarriers at ω_2 is apparent. The complex signal $s(t)$ is up-converted using an IQ modulator:

$$\begin{aligned} &\cos(\omega_{RF}t)\Re\{s(t)\} = \\ &\frac{I_a(t)+I_b(t)}{2}\cos((\omega_{RF}-\omega_2)t) + \frac{Q_a(t)-Q_b(t)}{2}\sin((\omega_{RF}-\omega_2)t) \\ &+\frac{I_a(t)+I_b(t)}{2}\cos((\omega_{RF}+\omega_2)t) + \frac{-Q_a(t)+Q_b(t)}{2}\sin((\omega_{RF}+\omega_2)t), \end{aligned} \tag{C.17}$$

$$
\begin{aligned}
&- \sin(\omega_{RF}t)\Im\{s(t)\} = \\
&\frac{-I_a(t) + I_b(t)}{2}\cos((\omega_{RF} - \omega_2)t) + \frac{-Q_a(t) - Q_b(t)}{2}\sin((\omega_{RF} - \omega_2)t) \\
&+\frac{I_a(t) - I_b(t)}{2}\cos((\omega_{RF} + \omega_2)t) + \frac{-Q_a(t) - Q_b(t)}{2}\sin((\omega_{RF} + \omega_2)t), \qquad \text{(C.18)}
\end{aligned}
$$

the signals are now added and sorted by frequency:

$$
\begin{aligned}
s_{RF}(t) =&\frac{I_a(t) + I_b(t)}{2}\cos((\omega_{RF} - \omega_2)t) + \frac{Q_a(t) - Q_b(t)}{2}\sin((\omega_{RF} - \omega_2)t) \\
&+\frac{-I_a(t) + I_b(t)}{2}\cos((\omega_{RF} - \omega_2)t) + \frac{-Q_a(t) - Q_b(t)}{2}\sin((\omega_{RF} - \omega_2)t) \\
&+\frac{I_a(t) + I_b(t)}{2}\cos((\omega_{RF} + \omega_2)t) + \frac{-Q_a(t) + Q_b(t)}{2}\sin((\omega_{RF} + \omega_2)t) \\
&+\frac{I_a(t) - I_b(t)}{2}\cos((\omega_{RF} + \omega_2)t) + \frac{-Q_a(t) - Q_b(t)}{2}\sin((\omega_{RF} + \omega_2)t), \qquad \text{(C.19)}
\end{aligned}
$$

cancellation of components leads to:

$$
\begin{aligned}
s_{RF}(t) =&I_b(t)\cos((\omega_{RF} - \omega_2)t) - Q_b(t)\sin((\omega_{RF} - \omega_2)t) \\
&+I_a(t)\cos((\omega_{RF} + \omega_2)t) - Q_a(t)\sin((\omega_{RF} + \omega_2)t). \qquad \text{(C.20)}
\end{aligned}
$$

As can be seen, even though I_a, Q_a and I_b, Q_b contribute to the modulation of the subcarriers at ω_2 after the iDFT they land in different frequencies after up-conversion using an IQ modulator. Part of the components cancel and I_b, Q_b modulate $\omega_{RF}-\omega_2$ whereas I_a, Q_a modulate $\omega_{RF}+\omega_2$.

Appendix D

Derivation of Laser Intensity and Frequency Responses

Equations (2.32), (2.34), (2.35) and (2.36) that were presented in Chapter 2 and used in the laser model in Chapter 3 are derived in this Appendix. The derivation is based on the linearisation of laser rate equations.

D.1 Rate Equations

The laser is modelled by a system of ordinary differential equations. These provide a description of the evolution of the photon and carrier populations as well as the phase of the output signal. The photon population is governed by Eq. (2.29), here repeated:

$$\dot{P} = (G - \gamma_p)P + R_{sp}. \tag{D.1}$$

The carrier population is governed by Eq. (2.28), here repeated:

$$\dot{N} = \frac{I}{q} - \gamma_e N - GP. \tag{D.2}$$

G – nonlinear gain
γ_p – photon decay rate
P – photon population
R_{sp} – spontaneous emission rate
I – injection current
q – magnitude of the electron charge
γ_e – carrier recombination rate
N – carrier population

Phase is governed by Eq. (2.30), here repeated:

$$\dot{\phi} = -(\omega_0 - \omega_{th}) + \frac{1}{2}\alpha_c(G - \gamma_p). \tag{D.3}$$

D.2 Steady State Solutions

Steady state solutions are obtained by setting the derivatives to zero:

$$\gamma_p = \frac{\overline{R}_{sp}}{\overline{P}} + \overline{G}, \tag{D.4}$$

$$\frac{\overline{I}}{q} = \gamma_e \overline{N} + \overline{GP}, \tag{D.5}$$

$$\gamma_p = -\frac{2}{\alpha_c}(\omega_0 - \omega_{th}) + \overline{G}. \tag{D.6}$$

D.3 Perturbation of P

Nonlinear gain (G) is dependent on both the number of carriers and of photons. It is linearised into a steady state gain $\overline{G}$ and two small signal dependences:

$$G(N, P) = \overline{G} + \frac{\partial G}{\partial N}\Delta N + \frac{\partial G}{\partial P}\Delta P. \tag{D.7}$$

The same procedure is performed for P:

$$P = \overline{P} + \Delta P. \tag{D.8}$$

Spontaneous emission rate depends on the number of carriers:

$$R_{sp} = \overline{R}_{sp} + \frac{\partial R_{sp}}{\partial N}\Delta N. \tag{D.9}$$

Substituting Eqs. (D.7), (D.8) and (D.9) into Eq. (D.1) yields:

$$\Delta\dot{P} = \left(\overline{G} + \frac{\partial G}{\partial N}\Delta N + \frac{\partial G}{\partial P}\Delta P - \gamma_p\right)\left(\overline{P} + \Delta P\right) + \overline{R}_{sp} + \frac{\partial R_{sp}}{\partial N}\Delta N. \tag{D.10}$$

ω_0 – lasing mode frequency
ω_{th} – lasing mode frequency at threshold
α_c – linewidth enhancement factor, or α-factor
G – nonlinear gain
γ_p – photon decay rate

Second and higher powers of ΔP and ΔN, as well as mixed products, are discarded:

$$\Delta\dot{P} = \left(\overline{G} + \frac{\partial G}{\partial P}\overline{P} - \gamma_p\right)\Delta P + \left(\frac{\partial G}{\partial N}\overline{P} + \frac{\partial R_{sp}}{\partial N}\right)\Delta N + \overline{GP} - \gamma_p\overline{P} + \overline{R}_{sp}, \quad \text{(D.11)}$$

substituting Eq. (D.4) in Eq. (D.11) and performing the following substitution:

$$\Gamma_P = \frac{\overline{R}_{sp}}{\overline{P}} - \frac{\partial G}{\partial P}\overline{P}, \quad \text{(D.12)}$$

yields:

$$\Delta\dot{P} = -\Gamma_P\Delta P + \left(\frac{\partial G}{\partial N}\overline{P} + \frac{\partial R_{sp}}{\partial N}\right)\Delta N. \quad \text{(D.13)}$$

D.4 Perturbation of N

The number of photons is separated into the steady state and small signal parts:

$$N = \overline{N} + \Delta N. \quad \text{(D.14)}$$

The carrier recombination rate is separated into a steady state value and on its dependence on the number of carriers:

$$\gamma_e = \overline{\gamma_e} + \frac{\partial\gamma_e}{\partial N}\Delta N. \quad \text{(D.15)}$$

Under direct modulation, current consists of two parts, bias and modulation current:

$$I = \overline{I} + I_m \quad \text{(D.16)}$$

Substituting N, γ_e and I, as well as Eqs. (D.7) and (D.8) into Eq. (D.2) leads to the expression:

$$\Delta\dot{N} = \frac{\overline{I} + I_m}{q} - \left(\overline{\gamma_e} + \frac{\partial\gamma_e}{\partial N}\Delta N\right)\left(\overline{N} + \Delta N\right) - \left(\overline{G} + \frac{\partial G}{\partial N}\Delta N + \frac{\partial G}{\partial P}\Delta P\right)\left(\overline{P} + \Delta P\right). \quad \text{(D.17)}$$

Second and higher powers of ΔP and ΔN, as well as mixed products, are discarded:

$$\Delta\dot{N} = \frac{\overline{I}}{q} + \frac{I_m}{q} - \overline{\gamma_e}\overline{N} - \overline{GP} - \left(\overline{\gamma_e} + \frac{\partial\gamma_e}{\partial N}\overline{N} + \frac{\partial G}{\partial N}\overline{P}\right)\Delta N - \left(\overline{G} + \frac{\partial G}{\partial P}\overline{P}\right)\Delta P. \quad \text{(D.18)}$$

Substituting Eq. (D.5) into Eq. (D.18) and performing the following substitution:

$$\Gamma_N = \overline{\gamma_e} + \frac{\partial\gamma_e}{\partial N}\overline{N} + \frac{\partial G}{\partial N}\overline{P}, \quad \text{(D.19)}$$

Γ_N – small signal carrier decay rate

leads to:

$$\Delta\dot{N} = -\Gamma_N \Delta N - \left(\overline{G} + \frac{\partial G}{\partial P}\overline{P}\right)\Delta P + \frac{I_m}{q}. \tag{D.20}$$

D.5 Perturbation of ϕ

Substituting Eq. (D.7) in Eq. (D.3) yields:

$$\Delta\dot{\phi} = -(\omega_0 - \omega_{th}) + \frac{1}{2}\alpha_c\left(\overline{G} + \frac{\partial G}{\partial N}\Delta N + \frac{\partial G}{\partial P}\Delta P - \gamma_p\right). \tag{D.21}$$

Equation (D.6) is substituted in Eq. (D.21):

$$\Delta\dot{\phi} = \frac{1}{2}\alpha_c\left(\frac{\partial G}{\partial N}\Delta N + \frac{\partial G}{\partial P}\Delta P\right). \tag{D.22}$$

The contribution of $\frac{\partial G}{\partial P}$ is neglected since the carrier-induced phase change is expected to be dominant [13]. Equation (D.22) is simplified to become:

$$\Delta\dot{\phi} = \frac{1}{2}\alpha_c\left(\frac{\partial G}{\partial N}\Delta N\right). \tag{D.23}$$

D.6 Intensity Response

In Eqs. (D.13) and (D.20) the following substitutions are performed:

$$\Delta P = \Delta_p(\omega)e^{j(\omega t + \theta_p)}, \tag{D.24}$$

$$\Delta N = \Delta_n(\omega)e^{j(\omega t + \theta_n)}, \tag{D.25}$$

$$I_m = I_p e^{j\omega t}. \tag{D.26}$$

The corresponding derivatives are:

$$\Delta\dot{P} = j\omega\Delta_p(\omega)e^{j(\omega t + \theta_p)}, \tag{D.27}$$

$$\Delta\dot{N} = j\omega\Delta_n(\omega)e^{j(\omega t + \theta_n)}. \tag{D.28}$$

These are now replaced into Eqs. (D.13) and (D.20) yielding:

$$j\omega\Delta_p(\omega)e^{j(\omega t+\theta_p)} = -\Gamma_P\Delta_p(\omega)e^{j(\omega t+\theta_p)} + \left(\frac{\partial G}{\partial N}\overline{P} + \frac{\partial R_{sp}}{\partial N}\right)\Delta_n(\omega)e^{j(\omega t+\theta_n)}, \quad \text{(D.29)}$$

$$j\omega\Delta_n(\omega)e^{j(\omega t+\theta_n)} = -\Gamma_N\Delta_n(\omega)e^{j(\omega t+\theta_n)} - \left(\overline{G} + \frac{\partial G}{\partial P}\overline{P}\right)\Delta_p(\omega)e^{j(\omega t+\theta_p)} + I_p/qe^{j\omega t}. \quad \text{(D.30)}$$

Equation (D.29) is solved for $\Delta_p(\omega)e^{j(\omega t+\theta_p)}$:

$$\Delta_p(\omega)e^{j(\omega t+\theta_p)} = \frac{\left(\frac{\partial G}{\partial N}\overline{P} + \frac{\partial R_{sp}}{\partial N}\right)}{j\omega + \Gamma_P}\Delta_n(\omega)e^{j(\omega t+\theta_n)}. \quad \text{(D.31)}$$

Equation (D.30) is solved for $\Delta_n(\omega)e^{j(\omega t+\theta_n)}$:

$$\Delta_n(\omega)e^{j(\omega t+\theta_n)} = -\frac{\left(\overline{G} + \frac{\partial G}{\partial P}\overline{P}\right)}{j\omega + \Gamma_N}\Delta_p(\omega)e^{j(\omega t+\theta_p)} + \frac{I_p/qe^{j\omega t}}{j\omega + \Gamma_N}. \quad \text{(D.32)}$$

Equation (D.32) is replaced in Eq. (D.31):

$$\Delta_p(\omega)e^{j\theta_p} = \frac{\left(\frac{\partial G}{\partial N}\overline{P} + \frac{\partial R_{sp}}{\partial N}\right)I_p/q}{-\omega^2 + j\omega(\Gamma_N + \Gamma_P) + \Gamma_N\Gamma_P + \left(\frac{\partial G}{\partial N}\overline{P} + \frac{\partial R_{sp}}{\partial N}\right)\left(\overline{G} + \frac{\partial G}{\partial P}\overline{P}\right)}. \quad \text{(D.33)}$$

The magnitude $\Delta_p(\omega)$ is given by:

$$\Delta_p(\omega) = \frac{\sqrt{\left(\left(\frac{\partial G}{\partial N}\overline{P} + \frac{\partial R_{sp}}{\partial N}\right)I_p/q\right)^2}}{\sqrt{\left(-\omega^2 + \Gamma_N\Gamma_P + \left(\frac{\partial G}{\partial N}\overline{P} + \frac{\partial R_{sp}}{\partial N}\right)\left(\overline{G} + \frac{\partial G}{\partial P}\overline{P}\right)\right)^2 + (\omega(\Gamma_N + \Gamma_P))^2}}. \quad \text{(D.34)}$$

The phase $\theta_p(\omega)$ is:

$$\theta_p(\omega) = \arctan\left(-\frac{\omega(\Gamma_N + \Gamma_P)}{-\omega^2 + \Gamma_N\Gamma_P + \left(\frac{\partial G}{\partial N}\overline{P} + \frac{\partial R_{sp}}{\partial N}\right)\left(\overline{G} + \frac{\partial G}{\partial P}\overline{P}\right)}\right). \quad \text{(D.35)}$$

Using the simplifications: $\frac{\partial R_{sp}}{\partial N} \ll \frac{\partial G}{\partial N}\overline{P}$ and $\frac{\partial G}{\partial P}\overline{P} \ll \overline{G}$ and the following substitutions [13]:

$$\Gamma_R = \frac{1}{2}(\Gamma_N + \Gamma_P), \quad \text{(D.36)}$$

$$\Omega_R = \left(\left(\overline{G} + \frac{\partial G}{\partial P}\overline{P}\right) + \left(\frac{\partial G}{\partial N}\overline{P}\frac{\partial R_{sp}}{\partial N}\right) - \frac{(\Gamma_N - \Gamma_P)^2}{4}\right)^{1/2}, \tag{D.37}$$

Eqs. (D.34) and (D.35) can be rewritten as:

$$\Delta_p(\omega) = \frac{\frac{\partial G}{\partial N}\overline{P}I_p/q}{\left((\omega^2 - \Omega_R^2 - \Gamma_R^2)^2 + 4\omega^2\Gamma_R^2\right)^{1/2}}, \tag{D.38}$$

and

$$\theta_p(\omega) = \arctan\left(\frac{2\omega\Gamma_R}{\omega^2 - \Omega_R^2 - \Gamma_R^2}\right). \tag{D.39}$$

These are Eqs. (2.32) and (2.34) respectively.

D.7 Frequency Response

The frequency shift arising from phase shift is given by [13]:

$$\Delta f = \frac{\Delta\dot{\phi}}{2\pi}, \tag{D.40}$$

consequently Eq. (D.23) becomes:

$$\Delta f = \frac{1}{4\pi}\alpha_c\left(\frac{\partial G}{\partial N}\Delta N\right). \tag{D.41}$$

Equation (D.25) is replaced in Eq. (D.41) and the following substitution is also performed:

$$\Delta f = \Delta_f(\omega)e^{j(\omega t + \theta_f)}, \tag{D.42}$$

yielding:

$$\Delta_f(\omega)e^{j(\omega t+\theta_f)} = \frac{1}{4\pi}\alpha_c\left(\frac{\partial G}{\partial N}\Delta_n(\omega)e^{j(\omega t+\theta_n)}\right). \tag{D.43}$$

Equation (D.31) is substituted in Eq. (D.32) and solved for $\Delta_n(\omega)e^{j(\omega t+\theta_n)}$:

$$\Delta_n(\omega)e^{j(\omega t+\theta_n)} = \frac{I_p/qe^{j\omega t}(j\omega + \Gamma_P)}{(j\omega + \Gamma_N)(j\omega + \Gamma_P) + \left(\overline{G} + \frac{\partial G}{\partial P}\overline{P}\right)\left(\frac{\partial G}{\partial N}\overline{P} + \frac{\partial R_{sp}}{\partial N}\right)}. \tag{D.44}$$

Finally Eq. (D.44) is substituted in Eq. (D.43):

$$\Delta_f(\omega)e^{j\theta_f} = \frac{\alpha_c I_p \frac{\partial G}{\partial N}}{4\pi q} \frac{\Gamma_P + j\omega}{-\omega^2 + j\omega(\Gamma_N + \Gamma_P) + \Gamma_N\Gamma_P + \left(\overline{G} + \frac{\partial G}{\partial P}\overline{P}\right)\left(\frac{\partial G}{\partial N}\overline{P} + \frac{\partial R_{sp}}{\partial N}\right)}. \tag{D.45}$$

The magnitude $\Delta_f(\omega)$ is:

$$\Delta_f(\omega) = \frac{\alpha_c I_p \frac{\partial G}{\partial N}}{4\pi q} \frac{\sqrt{\Gamma_P^2 + \omega^2}}{\sqrt{\left(-\omega^2 + \Gamma_N\Gamma_P + \left(\overline{G} + \frac{\partial G}{\partial P}\overline{P}\right)\left(\frac{\partial G}{\partial N}\overline{P} + \frac{\partial R_{sp}}{\partial N}\right)\right)^2 + \left(\omega(\Gamma_N + \Gamma_P)\right)^2}}. \tag{D.46}$$

The phase $\theta_f(\omega)$ is:

$$\theta_f(\omega) = \arctan\left(\frac{\omega}{\Gamma_P}\right) + \arctan\left(\frac{\omega(\Gamma_N + \Gamma_P)}{-\omega^2 + \Gamma_N\Gamma_P + \left(\overline{G} + \frac{\partial G}{\partial P}\overline{P}\right)\left(\frac{\partial G}{\partial N}\overline{P} + \frac{\partial R_{sp}}{\partial N}\right)}\right). \tag{D.47}$$

As previously performed, the simplifications $\frac{\partial R_{sp}}{\partial N} \ll \frac{\partial G}{\partial N}\overline{P}$ and $\frac{\partial G}{\partial P}\overline{P} \ll \overline{G}$ as well as Eqs. (D.36) and (D.37) [13] are used to rewrite Eqs. (D.46) and (D.47) as:

$$\Delta_f(\omega) = \frac{\alpha_c I_p \frac{\partial G}{\partial N}}{4\pi q} \left(\frac{\Gamma_P^2 + \omega^2}{\left(\omega^2 - \Omega_R^2 - \Gamma_R^2\right)^2 + 4\omega^2\Gamma_R^2}\right)^{1/2}, \tag{D.48}$$

and:

$$\theta_f(\omega) = \arctan\left(\frac{\omega}{\Gamma_P}\right) + \arctan\left(\frac{2\omega\Gamma_R}{\omega^2 - \Omega_R^2 - \Gamma_R^2}\right). \tag{D.49}$$

These are Eqs. (2.35) and (2.36) respectively.

Appendix E

Laser model configuration

In this Appendix, procedures to configure the laser model presented in Section 3.4.1 are described. For this, the output of a laser is used to calculate model parameters.

The chosen commercial laser's parameters [95] are used to configure the *VPI-photonics'* "LaserSM_RE" rate equation laser model, which is then subjected to stimuli and its output is recorded. For this example, a modulation index of ≃23% was chosen, the used parameters can be seen in Table E.1.

Table E.1: LaserSM_RE simulation parameters and biasing.

LaserSM_RE parameter	**Value**	**Unit**
ActiveRegionWidth	3×10^{-6}	m
ActiveRegionThickness	2.2×10^{-8}	m
OpticalCouplingEfficiency	0.38	-
LinearMaterialGainCoefficient	7.5×10^{-20}	m^2
TransparencyCarrierDensity	1.5×10^{24}	$1/m^3$
ConfinementFactor	0.07	-
GroupEffectiveIndex	3.2203	s
MaterialLinewidthEnhancementFactor	3	-
CarrierLifetime	10×10^{-9}	s
NonlinearGainCoefficient	7.4×10^{-23}	m^3
Bias current	36×10^{-3}	A
Drive amplitude	8×10^{-3}	A

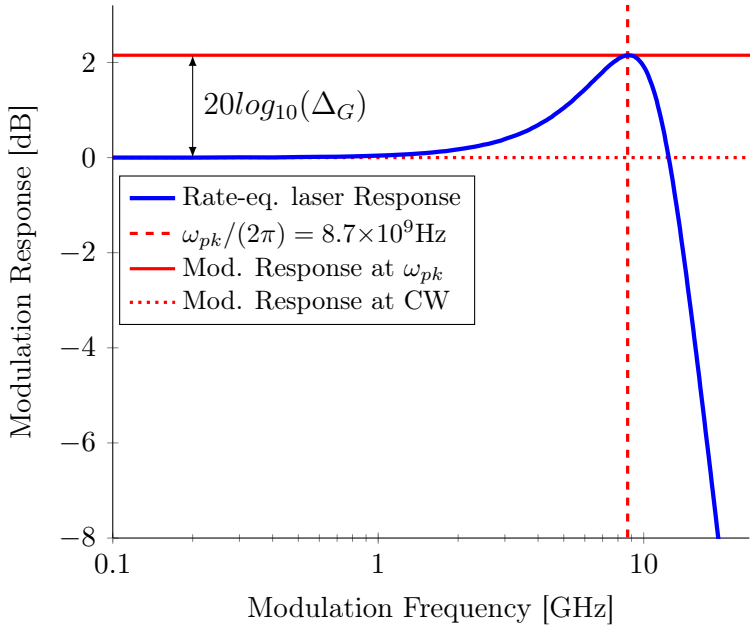

Figure E.1: Small signal modulation response of the rate equation laser configured with the parameters of Table E.1. The gain ratio (Δ_G) is also shown.

E.1 Intensity Response

Small signal measurements are used to configure the laser model response. From these, two values can be inferred, the peak response angular frequency (ω_{pk}) and the gain ratio between **C**ontinuous **W**ave (CW) and ω_{pk}, Δ_G=$\Delta_p(\omega_{pk})/\Delta_p(0)$, seen in Figure E.1. Note that the peak response frequency is not the same as Ω_R.

To configure Eq. (2.32) Ω_R and Γ_R are calculated. The expression $\frac{\partial G}{\partial N}\overline{P}I_p/q$ is composed of constants and is replaced by a single value. Starting with the derivative of Eq. (2.32), its zeros are found to calculate the angular peak response frequency:

$$\omega_{pk} = \sqrt{-(\Gamma_R - \Omega_R)(\Gamma_R + \Omega_R)}, \tag{E.1}$$

solving for Ω_R:

$$\Omega_R = \sqrt{\Gamma_R^2 + \omega_{pk}^2}. \tag{E.2}$$

The gain ratio can now be used to calculate Γ_R, substituting the frequencies of interest in Eq. (2.32):

$$\Delta_p(0) = \frac{\frac{\partial G}{\partial N}\overline{P}I_p/q}{\Omega_R^2 + \Gamma_R^2}, \tag{E.3}$$

$$\Delta_p(\omega_{pk}) = \frac{\frac{\partial G}{\partial N}\overline{P}I_p/q}{[(\omega_{pk}^2 - \Omega_R^2 - \Gamma_R^2)^2 + 4\omega_{pk}^2\Gamma_R^2]^{1/2}}, \tag{E.4}$$

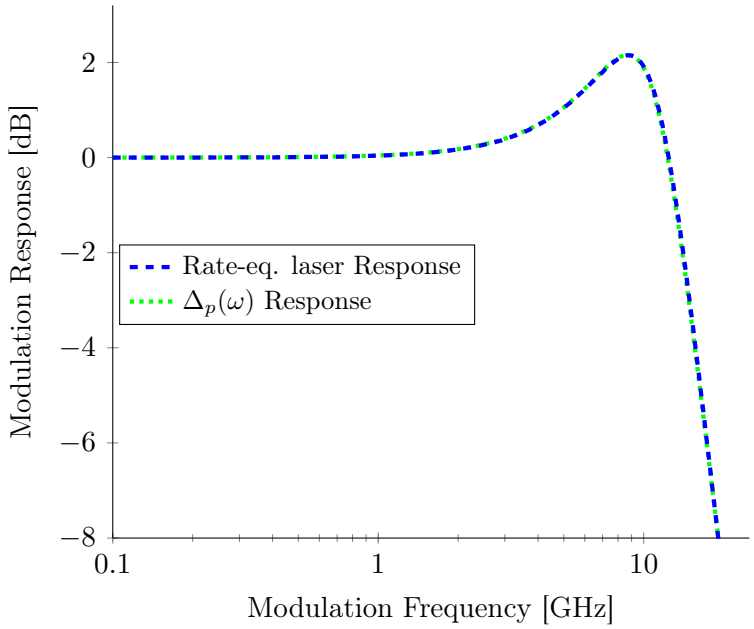

Figure E.2: Small signal response of the rate equation laser and the response of $\Delta_p(\omega)$, Eq. (2.32), using the parameters of Table E.2.

noting that the gain ratio is given by:

$$\Delta_G = \frac{\Delta_p(\omega_{pk})}{\Delta_p(0)}, \tag{E.5}$$

replacing Eq. (E.3) and Eq. (E.4) in Eq. (E.5):

$$\Delta_G = \frac{\Omega_R^2 + \Gamma_R^2}{[(\omega_{pk}^2 - \Omega_R^2 - \Gamma_R^2)^2 + 4\omega_{pk}^2\Gamma_R^2]^{1/2}}, \tag{E.6}$$

Ω_R of Eq. (E.6) can be replaced by Eq. (E.2):

$$\Delta_G = \frac{\omega_{pk}^2 + 2\Gamma_R^2}{[4\Gamma_R^4 + 4\Gamma_R^2\omega_{pk}^2]^{1/2}}, \tag{E.7}$$

solving for Γ_R:

$$\Gamma_R = \sqrt{-\frac{\Delta_G^2\omega_{pk}^2}{2\Delta_G^2 - 2} \pm \frac{\Delta_G\omega_{pk}^2\sqrt{\Delta_G - 1}\sqrt{\Delta_G + 1}}{2\Delta_G^2 - 2} + \frac{\omega_{pk}^2}{2\Delta_G^2 - 2}}, \tag{E.8}$$

due to the $\pm$, the result can be non-real. Only the real result is meaningful. Finally, $\frac{\partial G}{\partial N}\overline{P}I_p/q$ can be calculated using the peak response:

$$\frac{\partial G}{\partial N}\overline{P}I_p/q = \Delta_p(\omega_{pk})[(\omega_{pk}^2 - \Omega_R^2 - \Gamma_R^2)^2 + 4\omega_{pk}^2\Gamma_R^2]^{1/2}. \tag{E.9}$$

Table E.2: Laser model configuration.

Parameter	**Value**	**Unit**
ω_{pk}	$2\pi 8.7\times 10^9$	rad./s
Δ_G	1.281	-
Ω_R	$2\pi 9.92\times 10^9$	rad./s
Γ_R	$2\pi 4.76\times 10^9$	rad./s
$\frac{\partial G}{\partial N}\overline{P}I_p/q$	4.78×10^{21}	-

Using the measurements from Figure E.1 in Eqs. (E.2), (E.8) and (E.9) the configuration Table E.2 is obtained.

The response obtained using Table E.2 can be seen in Figure E.2 showing a good match.

E.2 FM Response (Chirp)

FM response is configured using Eq. (2.35). Two alternative approaches to finding the configuration parameters are presented. Initially the simple approach is used, where chirp is measured at Γ_R and Ω_R leading to simplified calculations. An exact approach is then derived where chirp is measured at 0.1GHz and Ω_R yielding more accurate results at the cost of more complex derivations. Both approaches require measurements of the chirp amplitude. Similarly to the intensity response, small signal measurements are used.

E.2.1 Simple Approach

Starting with Eq. (2.35), frequencies are selected that lead to the simplest form (ω=Ω_R and ω=Γ_R):

$$\Delta_f(\Omega_R) = \frac{\alpha_c I_p \frac{\partial G}{\partial N}}{4\pi q}\left(\frac{\Omega_R^2+\Gamma_P^2}{\Gamma_R^4+4\Omega_R^2\Gamma_R^2}\right)^{1/2}, \tag{E.10}$$

$$\Delta_f(\Gamma_R) = \frac{\alpha_c I_p \frac{\partial G}{\partial N}}{4\pi q}\left(\frac{\Gamma_R^2+\Gamma_P^2}{\Omega_R^4+4\Gamma_R^4}\right)^{1/2}, \tag{E.11}$$

taking Δ_F to be:

$$\Delta_F = \Delta_f(\Omega_R)/\Delta_f(\Gamma_R), \tag{E.12}$$

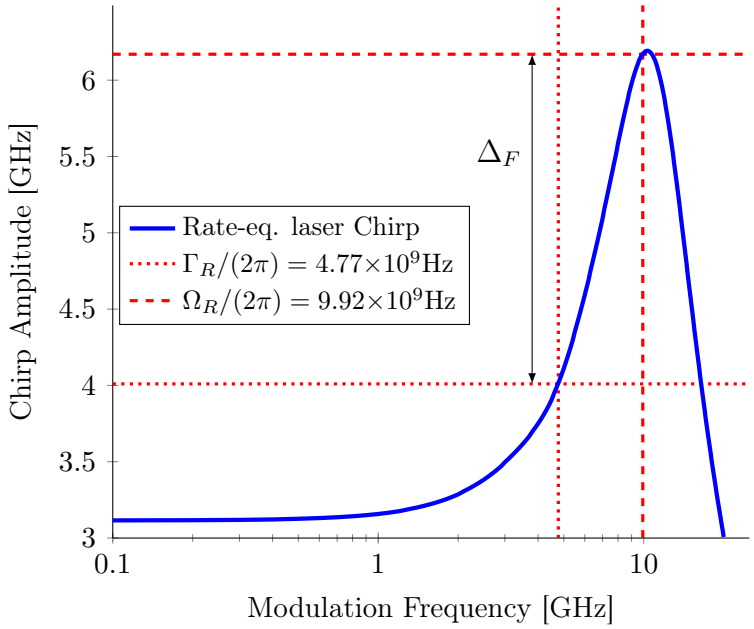

Figure E.3: Chirp response of the rate equation laser configured with the parameters of Table E.1. The chirp ratio (Δ_F) measured at Γ_R and Ω_R is also shown.

one unknown remains (Γ_P):

$$\Delta_F = \left(\frac{(\Omega_R^2 + \Gamma_P^2)(\Omega_R^4 + 4\Gamma_R^4)}{(\Gamma_R^4 + 4\Omega_R^2\Gamma_R^2)(\Gamma_R^2 + \Gamma_P^2)} \right)^{1/2}. \tag{E.13}$$

The previous equation is solved for Γ_P:

$$\Gamma_P = \sqrt{\frac{-4\Delta_F^2\Omega_R^2\Gamma_R^4 - \Delta_F^2\Gamma_R^6 + \Omega_R^6 + 4\Omega_R^2\Gamma_R^4}{4\Delta_F^2\Omega_R^2\Gamma_R^2 + \Delta_F^2\Gamma_R^4 - \Omega_R^4 - 4\Gamma_R^4}}, \tag{E.14}$$

finally, the expression $\alpha_c I_p \frac{\partial G}{\partial N}/4\pi q$ can be calculated at Ω_R. Note that I_p must be known as it is not a constant and influences chirp amplitude.

$$\frac{\alpha_c \frac{\partial G}{\partial N}}{4\pi q} = \frac{\Delta_f(\Omega_R)}{I_p} \frac{1}{\left(\frac{\Omega_R^2 + \Gamma_P^2}{\Gamma_R^4 + 4\Omega_R^2\Gamma_R^2} \right)^{1/2}}. \tag{E.15}$$

Using measurements from Figure E.3 in Eq. (E.14) and Eq. (E.15) the configuration parameters are calculated and can be seen in Table E.3.

E.2.2 Exact Approach

Instead of selecting the lowest frequency point to be Γ_R, the derivation can also be performed for an arbitrary lower frequency point. The ratio of Eq. (E.12) will

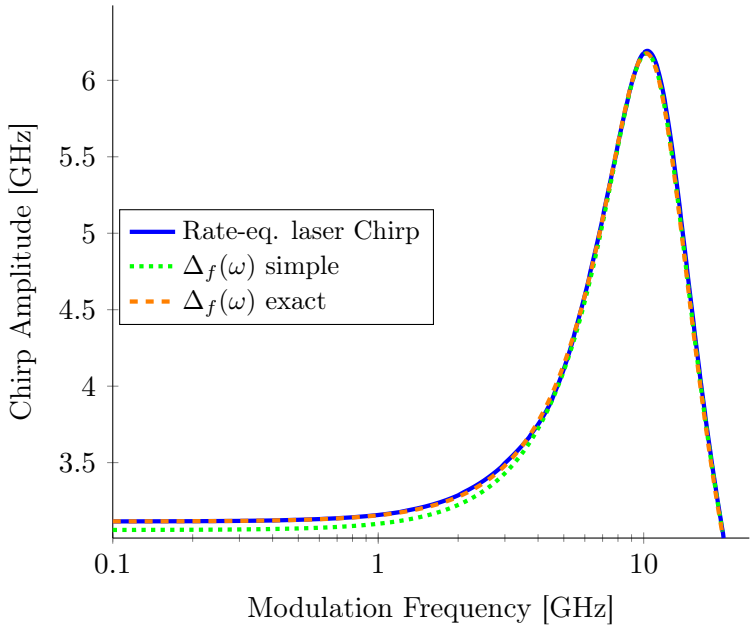

Figure E.4: Chirp response of the rate equation laser and the responses of $\Delta_f(\omega)$, Eq. (2.35), using the simple and exact approaches (parameters of Table E.3).

Table E.3: Laser model configuration.

Parameter	**Value**	**Unit**
I_p	8×10^{-3}	A
Δ_F	6.17/3.12	-
$\Gamma_P(simple)$	$2\pi7.82\times10^9$	rad./s
$\alpha_c\frac{\partial G}{\partial N}/4\pi q(simple)$	3.72×10^{22}	-
$\Gamma_P(exact)$	$2\pi8.05\times10^9$	rad./s
$\alpha_c\frac{\partial G}{\partial N}/4\pi q(exact)$	3.68×10^{22}	-

now be:

$$\Delta_F = \sqrt{\frac{(\Omega_R^2+\Gamma_P^2)((\omega^2-\Omega_R^2-\Gamma_R^2)^2+4\omega^2\Gamma_R^2)}{(\Gamma_R^4+4\Omega_R^2\Gamma_R^2)(\omega^2+\Gamma_P^2)}}, \tag{E.16}$$

solved for Γ_P:

$$\Gamma_P = \sqrt{\frac{\Omega_R^2(4\Delta_F^2\Gamma_R^2\omega^2-\Omega_R^4-2\Omega_R^2\Gamma_R^2+2\Omega_R^2\omega^2-\Gamma_R^4-2\Gamma_R^2\omega^2-\omega^4)+\Delta_F^2\Gamma_R^4\omega^2}{-4\Delta_F^2\Omega_R^2\Gamma_R^2-\Delta_F^2\Gamma_R^4+\Omega_R^4+2\Omega_R^2\Gamma_R^2-2\Omega_R^2\omega^2+\Gamma_R^4+2\Gamma_R^2\omega^2+\omega^4}}. \tag{E.17}$$

With the more precise Γ_P, $\alpha_c\frac{\partial G}{\partial N}/4\pi q$ is calculated at Ω_R using Eq. (E.15). The configuration values can be seen in Table E.3.

The results can be seen in Figure E.4(dotted green). Note that choosing a

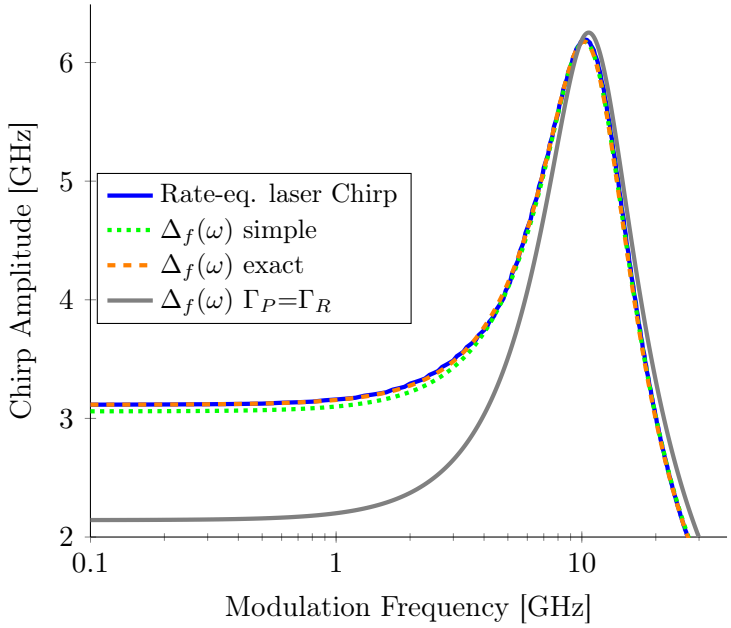

Figure E.5: Chirp response of the rate equation laser and the response of $\Delta_f(\omega)$, Eq. (2.35), using the Γ_P=Γ_R simplification (parameters of Table E.4). The responses using simple and exact approaches are also shown for comparison.

frequency lower than Γ_R for the low frequency measurements ensures a better match as seen in Figure E.4(dashed orange).

E.3 Γ_P Simplification

It is not always possible to measure chirp amplitude experimentally. The Γ_P parameter or the $\alpha_c \frac{\partial G}{\partial N}/4\pi q$ expression has to be estimated to obtain a match. The parameter Γ_P can be approximated with the simplification Γ_P=Γ_R. Equation (2.35) is simplified:

$$\Delta_f(\Omega_R) = \frac{\alpha_c I_p \frac{\partial G}{\partial N}}{4\pi q} \left(\frac{\Omega_R^2 + \Gamma_R^2}{\Gamma_R^4 + 4\Omega_R^2 \Gamma_R^2} \right)^{1/2}, \tag{E.18}$$

the expression $\alpha_c \frac{\partial G}{\partial N}/4\pi q$ can be calculated at ω=Ω_R:

$$\frac{\alpha_c \frac{\partial G}{\partial N}}{4\pi q} = \frac{\Delta_f(\Omega_R)}{I_p} \frac{1}{\left(\frac{\Omega_R^2+\Gamma_R^2}{\Gamma_R^4+4\Omega_R^2\Gamma_R^2} \right)^{1/2}}. \tag{E.19}$$

The configuration using Γ_P=Γ_R can be seen in the Table E.4.

The results of this simplification can be seen in Figure E.5(solid grey) where the low frequency mismatch is readily apparent. For this reason, this simplification

Table E.4: Laser model configuration using Γ_P=Γ_R simplification.

Parameters	**Values**	**Units**
Γ_P=Γ_R	$2\pi 4.76\times 10^9$	rad./s
$\alpha_c \frac{\partial G}{\partial N}/4\pi q$	4.28×10^{22}	-

should only be used when not enough measurements are available to infer the Γ_P parameter.

Appendix F

Derivation of the Analytical Formulation for SNR Prediction

In this Appendix, the analytical formulation for SNR prediction is derived in more detail. This complements the derivation of Section 3.4.2 on Page 52. Similarly to what is presented in Section 3.4.2 and for derivation purposes, subcarriers are composed of unmodulated cosines, albeit with different amplitudes. The IM and FM signals, represented by Eq. (3.67) and Eq. (3.74), are combined to form the optical signal at the fibre input (laser output). The components of the optical signal are described and formulas are presented. Chromatic dispersion is imposed on the signal and direct detection is performed. The terms arising from detection are presented and aggregated. This final form of the terms is used as the replacement variables of Eq. (3.80)-Eq. (3.87).

F.1 Optical Signal

The optical field at the laser output (fibre input) is described by Eq. (3.75):

$$E_{in} = e^{j\omega_c t} \left(A\Phi + S_{IM} + S_{FM} + IP \right), \tag{F.1}$$

the terms of this equation arise from the multiplication of Eq. (3.67):

$$IM_{in}(t) = A + \sum_{k=1}^{N} B_k \cos(\omega_k t) - \sum_{k=1}^{N} C_k \cos(2\omega_k t) - \sum_{k=1}^{N} \sum_{\substack{p \\ p<k}}^{N} D_{kp} \cos(\omega_k t \pm \omega_p t), \tag{F.2}$$

with Eq. (3.74):

$$\begin{aligned} FM_{in}(t) = \Phi &+ j2 \sum_{k=1}^{N} \frac{\Phi}{J_{0(k)}} J_{1(k)} \sin(\omega_k t) \\ &+ 2 \sum_{k=1}^{N} \frac{\Phi}{J_{0(k)}} J_{2(k)} \cos(2\omega_k t) \\ &\pm 2 \sum_{k=1}^{N} \sum_{\substack{p \\ p<k}}^{N} \frac{\Phi}{J_{0(k)} J_{0(p)}} J_{1(k)} J_{1(p)} \cos(\omega_k t \pm \omega_p t), \end{aligned} \tag{F.3}$$

The term $A\Phi$ is not frequency-dependent and can be seen as DC relatively to the optical carrier, influencing its power. Part of the product of IM with FM is obtained by cross multiplying the DC terms (A, Φ) with the frequency components.

The product between frequency components is limited to those of frequency ω_k. The resulting components land in ω_{2k} for subcarriers multiplying with themselves, and also in $\omega_k \pm \omega_p$ for multiplication of subcarriers with different frequencies.

The frequency of each product (parentheses) as well as the respective term of Eq. (3.75), also Eq. (F.1), are shown alongside the multiplication results:

$$\begin{aligned} E_{in} = e^{j\omega_c t}(& A\Phi && (\text{DC}) && \{A\Phi\} \\ & +\Phi \text{ IM}(\omega_k) + A \text{ FM}(\omega_k) && (\omega_k) && \{S_{IM} + S_{FM}\} \\ & +\Phi \text{ IM}(2\omega_k) + A \text{ FM}(2\omega_k) && (2\omega_k) && \{IP\} \\ & +\Phi \text{ IM}(\omega_k \pm \omega_p) + A \text{ FM}(\omega_k \pm \omega_p) && (\omega_k \pm \omega_p) && \{IP\} \\ & +\text{IM}(\omega_k)\text{FM}(\omega_k) && (2\omega_k) && \{IP\} \\ & +\text{IM}(\omega_k)\text{FM}(\omega_p) && (\omega_k \pm \omega_p) && \{IP\} \\ & +\text{FM}(\omega_k)\text{IM}(\omega_p)), && (\omega_k \pm \omega_p) && \{IP\} \end{aligned} \tag{F.4}$$

with each line of Eq. (F.4) being:

$$\Phi \text{ IM}(\omega_k) + A \text{ FM}(\omega_k) = \sum_{k=1}^{N} \left[B_k \Phi \cos(\omega_k t) + j2A \frac{\Phi}{J_{0(k)}} J_{1(k)} \sin(\omega_k t) \right], \tag{F.5}$$

$$\Phi\ \mathrm{IM}(2\omega_k) + A\ \mathrm{FM}(2\omega_k) = \sum_{k=1}^{N}\left[- C_k\Phi\cos(2\omega_k t) + 2A\frac{\Phi}{J_{0(k)}}J_{2(k)}\cos(2\omega_k t)\right], \tag{F.6}$$

$$\Phi\ \mathrm{IM}(\omega_k + \omega_p) = \sum_{k=1}^{N}\sum_{\substack{p\\p<k}}^{N}\left[- D_{kp}\Phi\cos(\omega_k t + \omega_p t)\right], \tag{F.7}$$

$$\Phi\ \mathrm{IM}(\omega_k - \omega_p) = \sum_{k=1}^{N}\sum_{\substack{p\\p<k}}^{N}\left[- D_{kp}\Phi\cos(\omega_k t - \omega_p t)\right], \tag{F.8}$$

$$A\ \mathrm{FM}(\omega_k + \omega_p) = \sum_{k=1}^{N}\sum_{\substack{p\\p<k}}^{N}\left[2A\frac{\Phi}{J_{0(k)}J_{0(p)}}J_{1(k)}J_{1(p)}\cos(\omega_k t + \omega_p t)\right], \tag{F.9}$$

$$A\ \mathrm{FM}(\omega_k - \omega_p) = \sum_{k=1}^{N}\sum_{\substack{p\\p<k}}^{N}\left[- 2A\frac{\Phi}{J_{0(k)}J_{0(p)}}J_{1(k)}J_{1(p)}\cos(\omega_k t - \omega_p t)\right], \tag{F.10}$$

$$\mathrm{IM}(\omega_k)\mathrm{FM}(\omega_k) = j\sum_{k=1}^{N}\left[B_k\frac{\Phi}{J_{0(k)}}J_{1(k)}\sin(2\omega_k t)\right], \tag{F.11}$$

$$\mathrm{IM}(\omega_k)\mathrm{FM}(\omega_p) = j\sum_{k=1}^{N}\sum_{\substack{p\\p<k}}^{N}\left[B_k\frac{\Phi}{J_{0(p)}}J_{1(p)}\sin(\omega_k t + \omega_p t) - B_k\frac{\Phi}{J_{0(p)}}J_{1(p)}\sin(\omega_k t - \omega_p t)\right], \tag{F.12}$$

$$\mathrm{FM}(\omega_k)\mathrm{IM}(\omega_p) = j\sum_{k=1}^{N}\sum_{\substack{p\\p<k}}^{N}\left[B_p\frac{\Phi}{J_{0(k)}}J_{1(k)}\sin(\omega_k t + \omega_p t) + B_p\frac{\Phi}{J_{0(k)}}J_{1(k)}\sin(\omega_k t - \omega_p t)\right]. \tag{F.13}$$

F.2 Transmission

CD is applied to the transmitted signal using the dispersion operator of Eq. (3.11):

$$d(\omega) = \frac{\beta_2}{2}\omega^2 L. \tag{F.14}$$

F.3 Direct Detection

Detected current is written as in Eq. (3.77) of Page 55:

$$\begin{aligned}
I_{Det.} =& \Re(2A\Phi S_{IMout}) + \Re(2A\Phi S_{FMout}) && (CS) \ \{I_{Signal}\} \\
&+2\Re(S_{IMout})\Re(S_{IMout}) + 2\Im(S_{IMout})\Im(S_{IMout}) && (2S) \ \{I_{SSII}\} \\
&+2\Re(S_{FMout})\Re(S_{FMout}) + 2\Im(S_{FMout})\Im(S_{FMout}) && (2S) \ \{I_{SSII}\} \\
&+2\Re(S_{IMout})\Re(S_{FMout}) + 2\Im(S_{IMout})\Im(S_{FMout}) && (2S) \ \{I_{SSII}\} \\
&+|S_{IMout}|^2 + |S_{FMout}|^2 && (S^2) \ \{I_{SSII}\} \\
&+\Re(2A\Phi IP_{out}) && (CIP) \ \{I_{SSII}\} \\
&+|A\Phi|^2 && (C^2) \ \{discarded\} \\
&+2\Re(S_{IMout})\Re(IP_{out}) + 2\Im(S_{IMout})\Im(IP_{out}) && (SIP) \ \{discarded\} \\
&+2\Re(S_{FMout})\Re(IP_{out}) + 2\Im(S_{FMout})\Im(IP_{out}) && (SIP) \ \{discarded\} \\
&+2\Re(IP_{out})\Re(IP_{out}) + 2\Im(IP_{out})\Im(IP_{out}) && (2IP) \ \{discarded\} \\
&+|IP_{out}|^2, && (IP^2) \ \{discarded\}
\end{aligned} \tag{F.15}$$

Each non-discarded component yields:

$$\Re(2A\Phi S_{IMout}) = 2A\Phi \sum_{k=1}^{N} \left[B_k \Phi \cos(\omega_k t)\cos(d(\omega_k)) \right], \tag{F.16}$$

$$\Re(2A\Phi S_{FMout}) = 2A\Phi \sum_{k=1}^{N} \left[2A\frac{\Phi}{J_{0(k)}} J_{1(k)} \sin(\omega_k t)\sin(d(\omega_k)) \right], \tag{F.17}$$

$$\begin{aligned}
&2\Re(S_{IMout})\Re(S_{IMout}) = \\
&\sum_{k=1}^{N}\sum_{\substack{p \\ p<k}}^{N} \Big[B_k B_p \Phi^2 \cos(\omega_k t + \omega_p t)\cos(d(\omega_k))\cos(d(\omega_p)) + \\
&\qquad B_k B_p \Phi^2 \cos(\omega_k t - \omega_p t)\cos(d(\omega_k))\cos(d(\omega_p)) \Big],
\end{aligned} \tag{F.18}$$

$$2\Im(S_{IMout})\Im(S_{IMout}) =$$
$$\sum_{k=1}^{N}\sum_{\substack{p\\p<k}}^{N}\Bigg[B_kB_p\Phi^2\cos(\omega_kt+\omega_pt)\sin(d(\omega_k))\sin(d(\omega_p))$$
$$+B_kB_p\Phi^2\cos(\omega_kt-\omega_pt)\sin(d(\omega_k))\sin(d(\omega_p))\Bigg], \tag{F.19}$$

$$2\Re(S_{FMout})\Re(S_{FMout}) =$$
$$\sum_{k=1}^{N}\sum_{\substack{p\\p<k}}^{N}\Bigg[-4A^2\frac{\Phi^2}{J_{0(k)}J_{0(p)}}J_{1(k)}J_{1(p)}\cos(\omega_kt+\omega_pt)\sin(d(\omega_k))\sin(d(\omega_p))$$
$$+4A^2\frac{\Phi^2}{J_{0(k)}J_{0(p)}}J_{1(k)}J_{1(p)}\cos(\omega_kt-\omega_pt)\sin(d(\omega_k))\sin(d(\omega_p))\Bigg], \tag{F.20}$$

$$2\Im(S_{FMout})\Im(S_{FMout}) =$$
$$\sum_{k=1}^{N}\sum_{\substack{p\\p<k}}^{N}\Bigg[-4A^2\frac{\Phi^2}{J_{0(k)}J_{0(p)}}J_{1(k)}J_{1(p)}\cos(\omega_kt+\omega_pt)\cos(d(\omega_k))\cos(d(\omega_p))$$
$$+4A^2\frac{\Phi^2}{J_{0(k)}J_{0(p)}}J_{1(k)}J_{1(p)}\cos(\omega_kt-\omega_pt)\cos(d(\omega_k))\cos(d(\omega_p))\Bigg], \tag{F.21}$$

$$2\Re(S_{IMout})\Re(S_{FMout}) =$$
$$\sum_{k=1}^{N}\sum_{\substack{p\\p<k}}^{N}\Bigg[-B_k\Phi 2A\frac{\Phi}{J_{0(p)}}J_{1(p)}\sin(\omega_kt-\omega_pt)\cos(d(\omega_k))\sin(d(\omega_p))$$
$$+B_p\Phi 2A\frac{\Phi}{J_{0(k)}}J_{1(k)}\sin(\omega_kt-\omega_pt)\sin(d(\omega_k))\cos(d(\omega_p))\Bigg], \tag{F.22}$$

$$2\Im(S_{IMout})\Im(S_{FMout}) =$$
$$\sum_{k=1}^{N}\sum_{\substack{p\\p<k}}^{N}\Bigg[B_k\Phi 2A\frac{\Phi}{J_{0(p)}}J_{1(p)}\sin(\omega_kt-\omega_pt)\sin(d(\omega_k))\cos(d(\omega_p))$$
$$-B_p\Phi 2A\frac{\Phi}{J_{0(k)}}J_{1(k)}\sin(\omega_kt-\omega_pt)\cos(d(\omega_k))\sin(d(\omega_p))\Bigg], \tag{F.23}$$

$$|S_{IMout}|^2 = \sum_{k=1}^{N} \left[\frac{1}{2} B_k^2 \Phi^2 \cos(2\omega_k t) \right], \tag{F.24}$$

$$|S_{FMout}|^2 = \sum_{k=1}^{N} \left[-2A^2 \frac{\Phi^2}{J_{0(k)}^2} J_{1(k)}^2 cos(2\omega_k t) \right], \tag{F.25}$$

$$\begin{aligned}
&\Re(2A\Phi IP_{out}) = \\
&2A\Phi \sum_{k=1}^{N} \left[-C_k \Phi \cos(2\omega_k t)\cos(d(2\omega_k)) + 2A \frac{\Phi}{J_{0(k)}} J_{2(k)} \cos(2\omega_k t)\cos(d(2\omega_k)) \right] \\
&+2A\Phi \sum_{k=1}^{N} \sum_{\substack{p \\ p<k}}^{N} \left[-D_{kp}\Phi \cos(\omega_k t + \omega_p t)\cos(d(\omega_k + \omega_p)) \right] \\
&+2A\Phi \sum_{k=1}^{N} \sum_{\substack{p \\ p<k}}^{N} \left[-D_{kp}\Phi \cos(\omega_k t - \omega_p t)\cos(d(\omega_k - \omega_p)) \right] \\
&+2A\Phi \sum_{k=1}^{N} \sum_{\substack{p \\ p<k}}^{N} \left[2A \frac{\Phi}{J_{0(k)} J_{0(p)}} J_{1(k)} J_{1(p)} \cos(\omega_k t + \omega_p t)\cos(d(\omega_k + \omega_p)) \right] \\
&+2A\Phi \sum_{k=1}^{N} \sum_{\substack{p \\ p<k}}^{N} \left[-2A \frac{\Phi}{J_{0(k)} J_{0(p)}} J_{1(k)} J_{1(p)} \cos(\omega_k t - \omega_p t)\cos(d(\omega_k - \omega_p)) \right] \\
&+2A\Phi \sum_{k=1}^{N} \left[B_k \frac{\Phi}{J_{0(k)}} J_{1(k)} \sin(2\omega_k t)\sin(d(2\omega_k)) \right] \\
&+2A\Phi \sum_{k=1}^{N} \sum_{\substack{p \\ p<k}}^{N} \left[B_k \frac{\Phi}{J_{0(p)}} J_{1(p)} \sin(\omega_k t + \omega_p t)\sin(d(\omega_k + \omega_p)) \right. \\
&\qquad \left. - B_k \frac{\Phi}{J_{0(p)}} J_{1(p)} \sin(\omega_k t - \omega_p t)\sin(d(\omega_k - \omega_p)) \right] \\
&+2A\Phi \sum_{k=1}^{N} \sum_{\substack{p \\ p<k}}^{N} \left[B_p \frac{\Phi}{J_{0(k)}} J_{1(k)} \sin(\omega_k t + \omega_p t)\sin(d(\omega_k + \omega_p)) \right. \\
&\qquad \left. + B_p \frac{\Phi}{J_{0(k)}} J_{1(k)} \sin(\omega_k t - \omega_p t)\sin(d(\omega_k - \omega_p)) \right].
\end{aligned} \tag{F.26}$$

F.4 Aggregation of Terms

The detected terms can be aggregated according to frequency, sine or cosine and dispersion operator.

F.4.1 I_{Signal}

The signal term (ω_k) is taken from Eq. (F.16) and Eq. (F.17):

$$I_{Signal} = \sum_{k=1}^{N} \left[2AB_k\Phi^2 \cos(\omega_k t)\cos(d(\omega_k)) \right] + \sum_{k=1}^{N} \left[A^2\Phi^2 \frac{4J_{1(k)}}{J_{0(k)}} \sin(\omega_k t)\sin(d(\omega_k)) \right]. \tag{F.27}$$

F.4.2 $I_{SSII}[2\omega_k]$

SSII landing in $2\omega_k$ is taken from Eqs. (F.24), (F.25) and (F.26):

$$I_{SSII}[2\omega_k] = \sum_{k=1}^{N} \left[\Phi^2 \left(\left(-2AC_k + \frac{4A^2 J_{2(k)}}{J_{0(k)}} \right) \cos(d(2\omega_k)) + \frac{B_k^2}{2} - \frac{2A^2 J_{1(k)}^2}{J_{0(k)}^2} \right) \cos(2\omega_k t) \right] + \sum_{k=1}^{N} \left[A\Phi^2 \frac{2B_k J_{1(k)}}{J_{0(k)}} \sin(2\omega_k t)\sin(d(2\omega_k)) \right]. \tag{F.28}$$

F.4.3 $I_{SSII}[\omega_k+\omega_p]$

SSII landing in $\omega_k+\omega_p$ is taken from Eqs. (F.18), (F.19), (F.20), (F.21) and (F.26). The $\omega_k+\omega_p$ terms of Eqs. (F.18) and (F.19) differ only in the dispersion operators, these can be combined to become:

$$B_k B_p \Phi^2 \cos(\omega_k t + \omega_p t)\Big(\cos(d(\omega_k))\cos(d(\omega_p)) + \sin(d(\omega_k))\sin(d(\omega_p)) \Big), \tag{F.29}$$

noting that:

$$\cos(a)\cos(b) + \sin(a)\sin(b) = \cos(a-b), \tag{F.30}$$

leads to:

$$B_k B_p \Phi^2 \cos(\omega_k t + \omega_p t)\cos(d(\omega_k) - d(\omega_p)). \tag{F.31}$$

The same process can be applied to Eqs. (F.20) and (F.21) to obtain:

$$-4A^2\frac{\Phi^2}{J_{0(k)}J_{0(p)}}J_{1(k)}J_{1(p)}\cos(\omega_k t+\omega_p t)\cos(d(\omega_k)-d(\omega_p)). \tag{F.32}$$

A grouping of Eqs. (F.18), (F.19), (F.20), (F.21) and (F.26) with the simplifications of Eqs. (F.31) and (F.32) is performed:

$$\begin{aligned} I_{SSII}[\omega_k+\omega_p] = & \\ & \sum_{k=1}^{N}\sum_{\substack{p\\p<k}}^{N}\left[\Phi^2\left(B_kB_p-\frac{4A^2J_{1(k)}J_{1(p)}}{J_{0(k)}J_{0(p)}}\right)\cos(\omega_k t+\omega_p t)\cos(d(\omega_k)-d(\omega_p))\right] \\ & +\sum_{k=1}^{N}\sum_{\substack{p\\p<k}}^{N}\left[2A\Phi^2\left(-D_{kp}+\frac{2AJ_{1(k)}J_{1(p)}}{J_{0(k)}J_{0(p)}}\right)\cos(\omega_k t+\omega_p t)\cos(d(\omega_k+\omega_p))\right] \\ & +\sum_{k=1}^{N}\sum_{\substack{p\\p<k}}^{N}\left[2A\Phi^2\left(\frac{B_kJ_{1(p)}}{J_{0(p)}}+\frac{B_pJ_{1(k)}}{J_{0(k)}}\right)\sin(\omega_k t+\omega_p t)\sin(d(\omega_k+\omega_p))\right]. \end{aligned} \tag{F.33}$$

F.4.4 $I_{SSII}[\omega_k-\omega_p]$

SSII landing in $\omega_k-\omega_p$ is taken from Eqs. (F.18), (F.19), (F.20), (F.21), (F.22), (F.23) and (F.26). The $\omega_k-\omega_p$ terms of Eqs. (F.18) and (F.19) can be combined as in Eq. (F.31):

$$B_kB_p\Phi^2\cos(\omega_k t-\omega_p t)\cos(d(\omega_k)-d(\omega_p)), \tag{F.34}$$

the same is done for Eqs. (F.20) and (F.21):

$$4A^2\frac{\Phi^2}{J_{0(k)}J_{0(p)}}J_{1(k)}J_{1(p)}\cos(\omega_k t-\omega_p t)\cos(d(\omega_k)-d(\omega_p)). \tag{F.35}$$

The following simplification:

$$\sin(a)\cos(b)-\cos(a)\sin(b)=\sin(a-b), \tag{F.36}$$

is used in Eqs. (F.22) and (F.23) to become:

$$2A\Phi^2\left(\frac{B_kJ_{1(p)}}{J_{0(p)}}+\frac{B_pJ_{1(k)}}{J_{0(k)}}\right)\sin(\omega_k t-\omega_p t),\cos(d(\omega_k)-d(\omega_p)), \tag{F.37}$$

all equations are finally grouped:

$$
\begin{aligned}
I_{SSII}[\omega_k - \omega_p] = \\
&\sum_{k=1}^{N}\sum_{\substack{p\\p<k}}^{N}\left[\Phi^2\left(B_kB_p + \frac{4A^2J_{1(k)}J_{1(p)}}{J_{0(k)}J_{0(p)}}\right)\cos(\omega_k t - \omega_p t)\cos(d(\omega_k) - d(\omega_p))\right] \\
&+\sum_{k=1}^{N}\sum_{\substack{p\\p<k}}^{N}\left[2A\Phi^2\left(\frac{B_kJ_{1(p)}}{J_{0(p)}} + \frac{B_pJ_{1(k)}}{J_{0(k)}}\right)\sin(\omega_k t - \omega_p t)\sin(d(\omega_k) - d(\omega_p))\right] \\
&+\sum_{k=1}^{N}\sum_{\substack{p\\p<k}}^{N}\left[2A\Phi^2\left(-D_{kp} - \frac{2AJ_{1(k)}J_{1(p)}}{J_{0(k)}J_{0(p)}}\right)\cos(\omega_k t - \omega_p t)\cos(d(\omega_k - \omega_p))\right] \\
&+\sum_{k=1}^{N}\sum_{\substack{p\\p<k}}^{N}\left[2A\Phi^2\left(\frac{B_pJ_{1(k)}}{J_{0(k)}} - \frac{B_kJ_{1(p)}}{J_{0(p)}}\right)\sin(\omega_k t - \omega_p t)\sin(d(\omega_k - \omega_p))\right]. \quad \text{(F.38)}
\end{aligned}
$$

F.5 Formulation for a Single Subcarrier

The equations for signal and SSII are altered to represent the signal and SSII of/landing on subcarrier k. The signal is given by:

$$I_{k(Signal)} = A\Phi^2 2B_k\cos(\omega_k t)\cos(d(\omega_k)) + A^2\Phi^2\frac{4J_{1(k)}}{J_{0(k)}}\sin(\omega_k t)\sin(d(\omega_k)). \quad \text{(F.39)}$$

For noise landing in subcarrier k due to components of the type $2\omega_k$, the condition $k{>}1$ is imposed as SSII from an expression of the type $2\omega_k$ lands in ω_2 for $k{=}1$:

$$
\begin{aligned}
I_{k(SSII)}[2\omega_k] = \\
&\Phi^2\left(\left(-2AC_{k/2} + \frac{4A^2J_{2(k/2)}}{J_{0(k/2)}}\right)\cos(d(\omega_k)) + \frac{B_{k/2}^2}{2} - \frac{2A^2J_{1(k/2)}^2}{J_{0(k/2)}^2}\right)\cos(\omega_k t) \\
&+A\Phi^2\frac{2B_{k/2}J_{1(k/2)}}{J_{0(k/2)}}\sin(\omega_k t)\sin(d(\omega_k)), \quad \text{(F.40)}
\end{aligned}
$$

for noise landing in subcarrier k due to components of the type $\omega_k+\omega_p$, the sums of Eq. (F.33) are reduced and p is limited to the ceiling $\lceil k/2\rceil-1$:

$$
\begin{aligned}
&I_{k(SSII)}[\omega_k+\omega_p] = \\
&\quad\sum_{p=1}^{\lceil k/2\rceil-1}\left[\Phi^2\left(B_{(k-p)}B_p - \frac{4A^2J_{1(k-p)}J_{1(p)}}{J_{0(k-p)}J_{0(p)}}\right)\cos(\omega_k t)\cos(d(\omega_{(k-p)}) - d(\omega_p))\right] \\
&+\sum_{p=1}^{\lceil k/2\rceil-1}\left[2A\Phi^2\left(-D_{(k-p)p} + \frac{2AJ_{1(k-p)}J_{1(p)}}{J_{0(k-p)}J_{0(p)}}\right)\cos(\omega_k t)\cos(d(\omega_k))\right] \\
&+\sum_{p=1}^{\lceil k/2\rceil-1}\left[2A\Phi^2\left(\frac{B_{(k-p)}J_{1(p)}}{J_{0(p)}} + \frac{B_pJ_{1(k-p)}}{J_{0(k-p)}}\right)\sin(\omega_k t)\sin(d(\omega_k))\right],
\end{aligned}
\tag{F.41}
$$

for noise landing in subcarrier k due to components of the type $\omega_k-\omega_p$, the sums of Eq. (F.38) are reduced. The initial value for p is $k+1$:

$$
\begin{aligned}
&I_{k(SSII)}[\omega_k-\omega_p] = \\
&\quad\sum_{p=k+1}^{N}\left[\Phi^2\left(B_pB_{(p-k)} + \frac{4A^2J_{1(p)}J_{1(p-k)}}{J_{0(p)}J_{0(p-k)}}\right)\cos(\omega_k t)\cos(d(\omega_p) - d(\omega_{(p-k)}))\right] \\
&+\sum_{p=k+1}^{N}\left[2A\Phi^2\left(\frac{B_pJ_{1(p-k)}}{J_{0(p-k)}} + \frac{B_{(p-k)}J_{1(p)}}{J_{0(p)}}\right)\sin(\omega_k t)\sin(d(\omega_p) - d(\omega_{(p-k)}))\right] \\
&+\sum_{p=k+1}^{N}\left[2A\Phi^2\left(-D_{p(p-k)} - \frac{2AJ_{1(p)}J_{1(p-k)}}{J_{0(p)}J_{0(p-k)}}\right)\cos(\omega_k t)\cos(d(\omega_k))\right] \\
&+\sum_{p=k+1}^{N}\left[2A\Phi^2\left(\frac{B_{(p-k)}J_{1(p)}}{J_{0(p)}} - \frac{B_pJ_{1(p-k)}}{J_{0(p-k)}}\right)\sin(\omega_k t)\sin(d(\omega_k))\right].
\end{aligned}
\tag{F.42}
$$

Bibliography

[1] "Cisco Visual Networking Index: Global Mobile Data Traffic Forecast Update 2016–2021", Cisco, Tech. Rep., 2016.

[2] W. Shieh and I. Djordjevic, *OFDM for Optical Communications*. Academic Press, 2009, ISBN: 978-0-12-374879-9.

[3] "Broadband optical access systems based on Passive Optical Networks (PON)", *ITU-T Recommendation G.983.1*, 2005.

[4] "Gigabit-capable passive optical networks (GPON): General characteristics", *ITU-T Recommendation G.984.1*, 2008.

[5] "IEEE Standard for Information technology- Local and metropolitan area networks- Part 3: CSMA/CD Access Method and Physical Layer Specifications Amendment: Media Access Control Parameters, Physical Layers, and Management Parameters for Subscriber Access Networks", *IEEE Std 802.3ah-2004*, Sep. 2004.
DOI: 10.1109/IEEESTD.2004.94617.

[6] "IEEE Standard for Information technology- Local and metropolitan area networks- Specific requirements- Part 3: CSMA/CD Access Method and Physical Layer Specifications Amendment 1: Physical Layer Specifications and Management Parameters for 10 Gb/s Passive Optical Networks", *IEEE Std 802.3av-2009 (Amendment to IEEE Std 802.3-2008)*, Oct. 2009.
DOI: 10.1109/IEEESTD.2009.5294950.

[7] "Gigabit-capable Passive Optical Networks (GPON): Physical Media Dependent (PMD) layer specification", *ITU-T Recommendation G.984.2*, 2003.

[8] "10-Gigabit-capable passive optical networks (XG-PON): General requirements", *ITU-T Recommendation G.987.1*, 2016.

[9] "40-Gigabit-capable passive optical networks (NG-PON2): General requirements", *ITU-T Recommendation G.989.1*, 2013.

[10] G. P. Agrawal, *Fiber-Optic Communication Systems*, 3rd ed. New York: John Wiley & Sons, 2002, ISBN: 0471215716.

[11] "40-Gigabit-capable passive optical networks 2 (NG-PON2): Physical media dependent (PMD) layer specification", *ITU-T Recommendation G.989.2*, 2014.

[12] K. Petermann, *Laser Diode Modulation and Noise*. Dordrecht: Kluwer, 1991, ISBN: 9027726728.

[13] G. P. Agrawal and N. K. Dutta, *Semiconductor Lasers*, 2nd ed. Boston: Springer, 1993.
DOI: 10.1007/978-1-4613-0481-4.

[14] C.-C. Wei, "Small-signal analysis of OOFDM signal transmission with directly modulated laser and direct detection", *Optics Letters*, vol. 36, no. 2, p. 151, Jan. 2011.
DOI: 10.1364/OL.36.000151.

[15] N. S. André, H. Louchet, K. Habel and A. Richter, "Analytical Formulation for SNR Prediction in DMDD OFDM-Based Access Systems", *IEEE Photonics Technology Letters*, vol. 26, no. 12, pp. 1255–1258, Jun. 2014.
DOI: 10.1109/LPT.2014.2320825.

[16] N. S. André, K. Habel, H. Louchet and A. Richter, "Equalization techniques for high-speed OFDM-based access systems using direct modulation and direct detection", in *2013 15th International Conference on Transparent Optical Networks (ICTON)*, IEEE, Jun. 2013, pp. 1–6.
DOI: 10.1109/ICTON.2013.6602971.

[17] N. S. André, K. Habel, H. Louchet and A. Richter, "Adaptive nonlinear Volterra equalizer for mitigation of chirp-induced distortions in cost effective IMDD OFDM systems", *Optics Express*, vol. 21, no. 22, p. 26 527, Nov. 2013.
DOI: 10.1364/OE.21.026527.

[18] N. S. André, H. Louchet, K. Habel and A. Richter, "33% Capacity improvement of a direct-modulation direct-detection OFDM link using adaptive Volterra equalization", in *2014 The European Conference on Optical Communication*

(ECOC), IEEE, Sep. 2014, pp. 1–3.
DOI: 10.1109/ECOC.2014.6964078.

[19] "Akamai's state of the internet Q1 2017 report", Akamai, Tech. Rep., 2017.

[20] T. van der Vorst, R. Brennenraedts, D. van Kerkhof and R. Bekkers, "Fast Forward - How the speed of the internet will develop between now and 2020", Technische Universiteit Eindhoven, Dialogic, Utrecht, Tech. Rep., 2014.

[21] *FTTH Council - Definition of Terms*, Feb. 2015.

[22] I. P. Kaminow and T. Li, Eds., *Optical Fiber Telecommunications IV-B: Systems and Impairments*. San Diego: Academic Press, 2002, ISBN: 0123951739.

[23] C. Lee, W. V. Sorin and B. Y. Kim, "Fiber to the Home Using a PON Infrastructure", *Journal of Lightwave Technology*, vol. 24, no. 12, pp. 4568–4583, Dec. 2006.
DOI: 10.1109/JLT.2006.885779.

[24] B. Y. Yoon, B. K. Kim, D. Lee, M. Hajduczenia and M. S. Lee, "Availability of 10G Transmitters, Receivers and Amplifiers", in *IEEE P802.3av 10GEPON Task Force Plenary Meeting*, Dallas, TX, 2006.

[25] S. Pato, P. Monteiro and H. Silva, "Performance evaluation of the physical layer for 10 Gbit/s ethernet passive optical networks", in *Proceedings of the 1st international conference on Access networks - AcessNets '06*, New York, New York, USA: ACM Press, 2006.
DOI: 10.1145/1189355.1189369.

[26] E. Vanin, "Performance evaluation of intensity modulated optical OFDM system with digital baseband distortion", *Optics Express*, vol. 19, no. 5, p. 4280, Feb. 2011.
DOI: 10.1364/OE.19.004280.

[27] A. Shahpari, R. M. Ferreira, R. S. Luis, Z. Vujicic, F. P. Guiomar, J. D. Reis and A. L. Teixeira, "Coherent Access: A Review", *Journal of Lightwave Technology*, vol. 35, no. 4, pp. 1050–1058, Feb. 2017.
DOI: 10.1109/JLT.2016.2623793.

[28] J. L. Wei, K. Grobe, C. Sanchez, E. Giacoumidis and H. Griesser, "Comparison of cost- and energy-efficient signal modulations for next generation passive optical networks", *Optics Express*, vol. 23, no. 22, p. 28 271, Nov. 2015.
DOI: 10.1364/OE.23.028271.

[29] A. Lender, "The duobinary technique for high-speed data transmission", *Transactions of the American Institute of Electrical Engineers, Part I: Communication and Electronics*, vol. 82, no. 2, pp. 214–218, May 1963.
DOI: 10.1109/TCE.1963.6373379.

[30] K. Yonenaga and S. Kuwano, "Dispersion-tolerant optical transmission system using duobinary transmitter and binary receiver", *Journal of Lightwave Technology*, vol. 15, no. 8, pp. 1530–1537, 1997.
DOI: 10.1109/50.618386.

[31] A. Abbasi, C. Spatharakis, G. Kanakis, N. M. André, H. Louchet, A. Katumba, J. Verbist, X. Yin, J. Bauwelinck, H. Avramopoulos, G. Roelkens and G. Morthier, "PAM-4 and Duobinary Direct Modulation of a Hybrid InP/SOI DFB Laser for 40 Gb/s Transmission over 2 km Single Mode Fiber", in *Optical Fiber Communication Conference*, OSA, 2016, p. M2C.6.
DOI: 10.1364/OFC.2016.M2C.6.

[32] G.-H. Im and J. Werner, "Bandwidth-efficient digital transmission up to 155 Mb/s over unshielded twisted pair wiring", in *Proceedings of ICC '93 - IEEE International Conference on Communications*, vol. 3, IEEE, 1993, pp. 1797–1803.
DOI: 10.1109/ICC.1993.397590.

[33] N. Cvijetic, "OFDM for Next-Generation Optical Access Networks", *Journal of Lightwave Technology*, vol. 30, no. 4, pp. 384–398, Feb. 2012.
DOI: 10.1109/JLT.2011.2166375.

[34] M. Bellanger, *FBMC physical layer : a primer*, 2010.

[35] R. W. Chang, "Synthesis of Band-Limited Orthogonal Signals for Multichannel Data Transmission", *Bell System Technical Journal*, vol. 45, no. 10, pp. 1775–1796, Dec. 1966.
DOI: 10.1002/j.1538-7305.1966.tb02435.x.

[36] S. Weinstein, "The history of orthogonal frequency-division multiplexing [History of Communications]", *IEEE Communications Magazine*, vol. 47, no. 11, pp. 26–35, Nov. 2009.
DOI: 10.1109/MCOM.2009.5307460.

[37] "IEEE Standard for Information technology–Telecommunications and information exchange between systems Local and metropolitan area networks–Specific requirements Part 11: Wireless LAN Medium Access Control (MAC) and Physical Layer (PHY) Specifications", *IEEE Std 802.11-2012 (Revision of IEEE Std 802.11-2007)*, Mar. 2012.
DOI: 10.1109/IEEESTD.2012.6178212.

[38] "IEEE Standard for Local and metropolitan area networks Air Interface for Fixed and Mobile Broadband Wireless Access Systems", *IEEE Std 802.16e-2005*, Feb. 2005.

[39] "Long Term Evolution of the 3GPP radio technology", 3GPP, Tech. Rep., 2006.

[40] "Radio Broadcasting Systems Digital Audio Broadcasting (DAB) to mobile, portable and fixed receivers", *ETSI Std EN 300 401*, 2006.

[41] "Digital Video Broadcasting (DVB) Framing structure, channel coding and modulation for digital terrestrial television", *ETSI Std EN 300 744*, 2009.

[42] ETSI, "Digital Video Broadcasting (DVB) System Specifications for Satellite services to Handheld devices (SH) below 3 GHz", *ETSI Std TS 102 585*, 2009.

[43] "Asymmetric digital subscriber line (ADSL) transceivers", *ITU-T Recommendation G.992.1*, 1999.

[44] "Digital Video Broadcasting (DVB) Frame structure channel coding and modulation for a second generation digital transmission system for cable systems (DVB-C2)", *ETSI Std EN 302 769*, 2012.

[45] "Unified high-speed wireline-based home networking transceivers – System architecture and physical layer specification", *ITU-T Recommendation G.9960*, 2015.

[46] "Narrowband orthogonal frequency division multiplexing power line communication transceivers for G3-PLC networks", *ITU-T Recommendation G.9903*, 2014.

[47] Qi Pan and R. Green, "Bit-error-rate performance of lightwave hybrid AM/OFDM systems with comparison with AM/QAM systems in the presence of clipping impulse noise", *IEEE Photonics Technology Letters*, vol. 8, no. 2, pp. 278–280, Feb. 1996.
DOI: 10.1109/68.484266.

[48] A. Lowery, Liang Du and J. Armstrong, "Orthogonal Frequency Division Multiplexing for Adaptive Dispersion Compensation in Long Haul WDM Systems", in *2006 Optical Fiber Communication Conference and the National Fiber Optic Engineers Conference*, IEEE, 2006, pp. 1–3.
DOI: 10.1109/OFC.2006.216072.

[49] I. B. Djordjevic and B. Vasic, "Orthogonal frequency division multiplexing for high-speed optical transmission", *Optics Express*, vol. 14, no. 9, p. 3767, 2006.
DOI: 10.1364/OE.14.003767.

[50] W. Shieh and C. Athaudage, "Coherent optical orthogonal frequency division multiplexing", *Electronics Letters*, vol. 42, no. 10, p. 587, 2006.
DOI: 10.1049/el:20060561.

[51] Dayou Qian, Junqiang Hu, Jianjun Yu, P. Ji, Lei Xu, Ting Wang, M. Cvijetic and T. Kusano, "Experimental demonstration of a novel OFDM-a based 10 Gb/s PON architecture", in *33rd European Conference and Exhibition on Optical Communication - ECOC 2007*, vol. 2007, IEE, 2007, pp. 541–541.
DOI: 10.1049/ic:20070200.

[52] G. Smith, D. Novak and Z. Ahmed, "Overcoming chromatic-dispersion effects in fiber-wireless systems incorporating external modulators", *IEEE Transactions on Microwave Theory and Techniques*, vol. 45, no. 8, pp. 1410–1415, 1997.
DOI: 10.1109/22.618444.

[53] W. Shieh, X. Yi and Y. Tang, "Transmission experiment of multi-gigabit coherent optical OFDM systems over 1000 km SSMF fibre", *Electronics Letters*, vol. 43, no. 3, p. 183, 2007.
DOI: 10.1049/el:20073496.

[54] S. L. Jansen, I. Morita, N. Takeda and H. Tanaka, "20-Gb/s OFDM Transmission over 4,160-km SSMF Enabled by RF-Pilot Tone Phase Noise Compensation", in *Optical Fiber Communication Conference and Exposition and The*

National Fiber Optic Engineers Conference, Optical Society of America, 2007, PDP15.

[55] D. F. Hewitt, "Orthogonal Frequency Division Multiplexing using Baseband Optical Single Sideband for Simpler Adaptive Dispersion Compensation", in *OFC/NFOEC 2007 - 2007 Conference on Optical Fiber Communication and the National Fiber Optic Engineers Conference*, IEEE, Mar. 2007, pp. 1–3. DOI: 10.1109/OFC.2007.4348553.

[56] W.-R. Peng, X. Wu, V. R. Arbab, B. Shamee, L. C. Christen, J.-Y. Yang, K.-M. Feng, A. E. Willner and S. Chi, "Experimental Demonstration of a Coherently Modulated and Directly Detected Optical OFDM System Using an RF-Tone Insertion", in *OFC/NFOEC 2008 - 2008 Conference on Optical Fiber Communication/National Fiber Optic Engineers Conference*, IEEE, Feb. 2008, pp. 1–3.
DOI: 10.1109/OFC.2008.4528410.

[57] W.-R. Peng, X. Wu, V. R. Arbab, B. Shamee, J.-Y. Yang, L. C. Christen, K.-M. Feng, A. E. Willner and S. Chi, "Experimental Demonstration of 340 km SSMF Transmission Using a Virtual Single Sideband OFDM Signal that Employs Carrier Suppressed and Iterative Detection Techniques", in *OFC/NFOEC 2008 - 2008 Conference on Optical Fiber Communication/National Fiber Optic Engineers Conference*, IEEE, Feb. 2008, pp. 1–3.
DOI: 10.1109/OFC.2008.4528409.

[58] M. Schuster, S. Randel, C. A. Bunge, S. C. J. Lee, F. Breyer, B. Spinnler and K. Petermann, "Spectrally Efficient Compatible Single-Sideband Modulation for OFDM Transmission With Direct Detection", *IEEE Photonics Technology Letters*, vol. 20, no. 9, pp. 670–672, May 2008.
DOI: 10.1109/LPT.2008.918911.

[59] J. Tang and K. Shore, "30-gb/s signal transmission over 40-km directly modulated DFB-laser-based single-mode-fiber links without optical amplification and dispersion compensation", *Journal of Lightwave Technology*, vol. 24, no. 6, pp. 2318–2327, Jun. 2006.
DOI: 10.1109/JLT.2006.874557.

[60] K. Petermann, "FM–AM noise conversion in dispersive single-mode fibre transmission lines", *Electronics Letters*, vol. 26, no. 25, p. 2097, 1990.
DOI: 10.1049/el:19901350.

[61] S. Weinstein and P. Ebert, "Data Transmission by Frequency-Division Multiplexing Using the Discrete Fourier Transform", *IEEE Transactions on Communication Technology*, vol. 19, no. 5, pp. 628–634, Oct. 1971.
DOI: 10.1109/TCOM.1971.1090705.

[62] C. R. Berger, Y. Benlachtar, R. I. Killey and P. A. Milder, "Theoretical and experimental evaluation of clipping and quantization noise for optical OFDM", *Optics Express*, vol. 19, no. 18, p. 17 713, Aug. 2011.
DOI: 10.1364/OE.19.017713.

[63] A. Razmtouz, K. Habel, C. Kottke, C. Ruprecht and W. Rosenkranz, "Initial ranging scheme based on interpolated Zadoff-Chu sequences for OFDMA-PON", *Optics Express*, vol. 22, no. 3, p. 3669, Feb. 2014.
DOI: 10.1364/OE.22.003669.

[64] T. Weiss, J. Hillenbrand, A. Krohn and F. Jondral, "Mutual interference in OFDM-based spectrum pooling systems", in *2004 IEEE 59th Vehicular Technology Conference. VTC 2004-Spring (IEEE Cat. No.04CH37514)*, vol. 4, IEEE, 2004, pp. 1873–1877.
DOI: 10.1109/VETECS.2004.1390598.

[65] C. Muschallik, "Improving an OFDM reception using an adaptive Nyquist windowing", *IEEE Transactions on Consumer Electronics*, vol. 42, no. 3, pp. 259–269, 1996.
DOI: 10.1109/30.536046.

[66] Society of Cable Telecommunication Engineers, "Radio Frequency over Glass Fiber-to-the-Home Specification", *ANSI/SCTE 174*, 2010.

[67] D. R. Sánchez Montero and C. Vázquez García, "Multimode Graded-Index Optical Fibers for Next-Generation Broadband Access", in *Current Developments in Optical Fiber Technology*, InTech, Jun. 2013.
DOI: 10.5772/54245.

[68] T. Irujo, *OM4 - The Next Generation of Multimode Fiber (White Paper)*, 2011.

[69] "40G Extended Reach with Corning Cable Systems OM3/OM4 Connectivity with the Avago 40G QSFP+ eSR4 Transceiver (White Paper)", Corning, Tech. Rep., 2013.

[70] E. Ip, P. Ji, E. Mateo, Y.-K. Huang, L. Xu, D. Qian, N. Bai and T. Wang, "100G and Beyond Transmission Technologies for Evolving Optical Networks and Relevant Physical-Layer Issues", *Proceedings of the IEEE*, vol. 100, no. 5, pp. 1065–1078, May 2012.
DOI: 10.1109/JPROC.2012.2183329.

[71] S. O. Arik, J. M. Kahn and K.-P. Ho, "MIMO Signal Processing for Mode-Division Multiplexing: An overview of channel models and signal processing architectures", *IEEE Signal Processing Magazine*, vol. 31, no. 2, pp. 25–34, Mar. 2014.
DOI: 10.1109/MSP.2013.2290804.

[72] E. Peral and A. Yariv, "Large-signal theory of the effect of dispersive propagation on the intensity modulation response of semiconductor lasers", *Journal of Lightwave Technology*, vol. 18, no. 1, pp. 84–89, Jan. 2000.
DOI: 10.1109/50.818911.

[73] J. Wang and K. Petermann, "Small signal analysis for dispersive optical fiber communication systems", *Journal of Lightwave Technology*, vol. 10, no. 1, pp. 96–100, 1992.
DOI: 10.1109/50.108743.

[74] G. P. Agrawal, *Applications of Nonlinear Fiber Optics*, Second Edition. Burlington: Academic Press, 2008.
DOI: 10.1016/B978-0-12-374302-2.X5001-3.

[75] G. P. Agrawal, *Nonlinear Fiber Optics*, Fourth Edition, G. P. Agrawal, Ed., ser. Optics and Photonics. San Diego: Academic Press, 2006.
DOI: 10.1016/B978-0-12-369516-1.X5000-6.

[76] N. S. André, H. Louchet, V. Filsinger, E. Hansen and A. Richter, "OFDM and PAM comparison using a high baudrate low resolution IM/DD interface for 400G Ethernet access", *Optics Express*, vol. 24, no. 11, p. 11 926, May 2016.
DOI: 10.1364/OE.24.011926.

[77] G. Smith, D. Novak and Z. Ahmed, "Novel technique for generation of optical SSB with carrier using a single MZM to overcome fiber chromatic dispersion", in *International Topical Meeting on Microwave Photonics. MWP '96 Technical Digest. Satellite Workshop (Cat. No.96TH8153)*, IEEE, pp. 5–8.
DOI: 10.1109/MWP.1996.660352.

[78] M. Schuster, B. Spinnler, C. Bunge and K. Petermann, "Spectrally efficient OFDM-transmission with compatible single-sideband modulation for direct detection", in *33rd European Conference and Exhibition on Optical Communication - ECOC 2007*, vol. 2007, IEE, 2007, P075–P075.
DOI: 10.1049/ic:20070465.

[79] M. Abramowitz and I. A. Stegun, *Handbook of Mathematical Functions With Formulas, Graphs and Mathematical Tables*, 10th ed. Washington, DC: National Bureau of Standards, 1972.

[80] G. Meslener, "Chromatic dispersion induced distortion of modulated monochromatic light employing direct detection", *IEEE Journal of Quantum Electronics*, vol. 20, no. 10, pp. 1208–1216, Oct. 1984.
DOI: 10.1109/JQE.1984.1072286.

[81] C. Sánchez, B. Ortega, J. L. Wei, J. Tang and J. Capmany, "Analytical formulation of directly modulated OOFDM signals transmitted over an IM/DD dispersive link", *Optics Express*, vol. 21, no. 6, p. 7651, Mar. 2013.
DOI: 10.1364/OE.21.007651.

[82] A. J. Lowery, "Improving Sensitivity and Spectral Efficiency in Direct-Detection Optical OFDM Systems", in *OFC/NFOEC 2008 - 2008 Conference on Optical Fiber Communication/National Fiber Optic Engineers Conference*, IEEE, Feb. 2008, pp. 1–3.
DOI: 10.1109/OFC.2008.4528367.

[83] H. Mahmoud and H. Arslan, "Error vector magnitude to SNR conversion for nondata-aided receivers", *IEEE Transactions on Wireless Communications*, vol. 8, no. 5, pp. 2694–2704, May 2009.
DOI: 10.1109/TWC.2009.080862.

[84] W. Yan, B. Liu, L. Li, Z. Tao, T. Takahara and J. C. Rasmussen, "Nonlinear Distortion and DSP-based Compensation in Metro and Access Networks using

Discrete Multi-tone", in *European Conference and Exhibition on Optical Communication*, Washington, D.C.: OSA, 2012, Mo.1.B.2.
DOI: 10.1364/ECEOC.2012.Mo.1.B.2.

[85] B. Krongold, K. Ramchandran and D. Jones, "Computationally efficient optimal power allocation algorithm for multicarrier communication systems", in *ICC '98. 1998 IEEE International Conference on Communications. Conference Record. Affiliated with SUPERCOMM'98 (Cat. No.98CH36220)*, vol. 2, IEEE, 1998, pp. 1018–1022.
DOI: 10.1109/ICC.1998.685166.

[86] J. Campello, "Optimal discrete bit loading for multicarrier modulation systems", in *Proceedings. 1998 IEEE International Symposium on Information Theory (Cat. No.98CH36252)*, IEEE, 1998, p. 193.
DOI: 10.1109/ISIT.1998.708791.

[87] C. Xia and W. Rosenkranz, "Nonlinear Electrical Equalization for Different Modulation Formats With Optical Filtering", *Journal of Lightwave Technology*, vol. 25, no. 4, pp. 996–1001, Apr. 2007.
DOI: 10.1109/JLT.2007.891174.

[88] P. Chow, J. Cioffi and J. Bingham, "A practical discrete multitone transceiver loading algorithm for data transmission over spectrally shaped channels", *IEEE Transactions on Communications*, vol. 43, no. 2/3/4, pp. 773–775, Feb. 1995.
DOI: 10.1109/26.380108.

[89] R. Fischer and J. Huber, "A new loading algorithm for discrete multitone transmission", in *Proceedings of GLOBECOM'96. 1996 IEEE Global Telecommunications Conference*, vol. 1, IEEE, 1996, pp. 724–728.
DOI: 10.1109/GLOCOM.1996.594456.

[90] D. Hsu, C.-C. Wei, H.-Y. Chen, C.-Y. Song, I.-C. Lu and J. Chen, "74.4% SSII Cancellation in an EAM-based OFDM-IMDD Transmission System", in *Optical Fiber Communication Conference/National Fiber Optic Engineers Conference 2013*, Washington, D.C.: OSA, 2013, OM2C.7.
DOI: 10.1364/OFC.2013.OM2C.7.

[91] W. Yan, T. Tanaka, B. Liu, M. Nishihara, L. Li, T. Takahara, Z. Tao, J. C. Rasmussen and T. Drenski, "100 Gb/s Optical IM-DD Transmission with 10G-Class Devices Enabled by 65 GSamples/s CMOS DAC Core", in *Optical*

Fiber Communication Conference/National Fiber Optic Engineers Conference 2013, Washington, D.C.: OSA, 2013, OM3H.1.
DOI: 10.1364/OFC.2013.OM3H.1.

[92] R. P. Stanley, *Enumerative Combinatorics, Volume I*. Cambridge University Press, 2011, ISBN: 9781107602625.

[93] C. Belfiore and J. Park, "Decision feedback equalization", *Proceedings of the IEEE*, vol. 67, no. 8, pp. 1143–1156, 1979.
DOI: 10.1109/PROC.1979.11409.

[94] V. Madisetti, R. Dorf and I. Young, *The Digital Signal Processing Handbook*, 2nd ed., V. Madisetti, Ed. Boca Raton: CRC Press, 2010.

[95] J. L. Wei, C. Sánchez, R. P. Giddings, E. Hugues-Salas and J. M. Tang, "Significant improvements in optical power budgets of real-time optical OFDM PON systems", *Optics Express*, vol. 18, no. 20, p. 20 732, Sep. 2010.
DOI: 10.1364/OE.18.020732.

Publications as First Author

N. S. André, H. Louchet, V. Filsinger, E. Hansen and A. Richter, "OFDM and PAM comparison using a high baudrate low resolution IM/DD interface for 400G Ethernet access", *Optics Express*, vol. 24, no. 11, p. 11 926, May 2016.
DOI: 10.1364/OE.24.011926.

N. M. André, H. Louchet, V. Filsinger, E. Hansen and A. Richter, "Experimental 32Gbaud OFDM transmission using a 3-bit DAC", in *Asia Communications and Photonics Conference 2015*, OSA, 2015, ASu1E.1.
DOI: 10.1364/ACPC.2015.ASu1E.1.

N. S. André, H. Louchet, K. Habel and A. Richter, "33% Capacity improvement of a direct-modulation direct-detection OFDM link using adaptive Volterra equalization", in *2014 The European Conference on Optical Communication (ECOC)*, IEEE, Sep. 2014, pp. 1–3.
DOI: 10.1109/ECOC.2014.6964078.

N. S. André, H. Louchet, K. Habel and A. Richter, "Analytical Formulation for SNR Prediction in DMDD OFDM-Based Access Systems", *IEEE Photonics Technology Letters*, vol. 26, no. 12, pp. 1255–1258, Jun. 2014.
DOI: 10.1109/LPT.2014.2320825.

N. S. André, K. Habel, H. Louchet and A. Richter, "Adaptive nonlinear Volterra equalizer for mitigation of chirp-induced distortions in cost effective IMDD OFDM systems", *Optics Express*, vol. 21, no. 22, p. 26 527, Nov. 2013.
DOI: 10.1364/OE.21.026527.

N. S. André, K. Habel, H. Louchet and A. Richter, "Equalization techniques for high-speed OFDM-based access systems using direct modulation and direct detection", in *2013 15th International Conference on Transparent Optical*

Networks (ICTON), IEEE, Jun. 2013, pp. 1–6.
DOI: 10.1109/ICTON.2013.6602971.

Publications as Co-Author

A. Rahim, A. Abbasi, M. Shahin, N. S. André, A. Richter, J. Van Kerrebrouck, K. Van Gasse, A. Katumba, B. Moeneclaey, X. Yin, G. Morthier, R. Baets and G. Roelkens, "50 Gb/s DMT and 120 Mb/s LTE signal transmission over 5 km of optical fiber using a silicon photonics transceiver", in *Advanced Photonics 2018 (BGPP, IPR, NP, NOMA, Sensors, Networks, SPPCom, SOF)*, OSA, 2018, IW1B.4.
DOI: 10.1364/IPRSN.2018.IW1B.4.

A. Rahim, A. Abbasi, N. S. André, A. Katumba, H. Louchet, K. Van Gasse, R. Baets, G. Morthier and G. Roelkens, "69 Gb/s DMT direct modulation of a Heterogeneously Integrated InP-on-Si DFB Laser", in *Optical Fiber Communication Conference*, OSA, 2017, Th1B.5.
DOI: 10.1364/OFC.2017.Th1B.5.

A. Abbasi, C. Spatharakis, G. Kanakis, N. S. André, H. Louchet, A. Katumba, J. Verbist, H. Avramopoulos, P. Bienstman, X. Yin, J. Bauwelinck, G. Roelkens and G. Morthier, "High Speed Direct Modulation of a Heterogeneously Integrated InP/SOI DFB Laser", *Journal of Lightwave Technology*, vol. 34, no. 8, pp. 1683–1687, Apr. 2016.
DOI: 10.1109/JLT.2015.2510868.

A. Abbasi, C. Spatharakis, G. Kanakis, N. S. André, H. Louchet, A. Katumba, J. Verbist, X. Yin, J. Bauwelinck, H. Avramopoulos, G. Roelkens and G. Morthier, "PAM-4 and Duobinary Direct Modulation of a Hybrid InP/SOI DFB Laser for 40 Gb/s Transmission over 2 km Single Mode Fiber", in *Optical Fiber Communication Conference*, OSA, 2016, p. M2C.6.
DOI: 10.1364/OFC.2016.M2C.6.